Burst Pressure Prediction of Cord-Rubber Composite Pressure Vessels

Using Global-Local Nonlinear Finite Element Analysis

MSc. Thesis

Ahaan Bhosale

Delft University of Technology

TU Delft

TANIQ

This page was intentionally left blank.

Burst Pressure Prediction of Cord-Rubber Composite Pressure Vessels

Using Global-Local Nonlinear Finite Element Analysis

by

Ahaan Bhosale

to obtain the degree of Master of Science

at the Delft University of Technology,

to be defended publicly on Friday, December 16, 2022 at 2:00 PM.

Student number:	5268605	
Project duration:	March 1, 2022 – December 16, 2022	
Thesis committee:	Prof. dr. ir. R. Benedictus,	TU Delft, Chair
	Dr. B. Chen,	TU Delft
	Dr. ir. JMJF. van Campen,	TU Delft
	Ir. R. Barendse,	Taniq BV

This thesis is confidential and cannot be made public until December 16, 2024.

TU Delft

TANIQ

This page was intentionally left blank.

Foreword

"No man needs sympathy because he has to work, because he has a burden to carry. Far and away the best prize that life offers is the chance to work hard at work worth doing."

Theodore Roosevelt

This thesis is written to obtain my Master's degree in Aerospace Engineering with a specialization in aerospace structures at Delft University of Technology, Netherlands.

My journey at TU Delft has been an unusual and intriguing one. Since I arrived right in the heat of the Covid-19 pandemic in the fall of 2020, living and studying away from home for the first time was not the only new challenge I had to face. I often wondered whether my decision to travel at such a time was justified, given I had very minimal time to spend on campus, and that all the lectures that I ever attended here were conducted online. However, as time progressed, I realised that my education here was of far more than just attending a few classes in a physical space. During my time here, I have experienced freedom, undertaken greater responsibilities, learnt the value of friendship, interacted with some incredible minds, and also understood the need to be more empathetic towards the issues that we all face. And for these experiences, I am eternally grateful.

I believe my thesis has been an embodiment of all the lessons I have learnt here. Coursing through the journey, I have felt confusion, elation, frustration, relief, tiredness, excitement, and a lot more. And I do believe all the negative feelings were equally as important as the positive ones as they pushed me to work harder and to make progress. Of course, none of this progress would have been possible without the support of a LOT of people, each of whose presence has made a uniquely invaluable contribution to the project.

I would first like to thank Soren and Coen from Taniq for entrusting me with this project - first as an intern, and then as a thesis student. For any graduate student, I think the most important aspect is feeling as if the work they do is valued, and I have always felt this at Taniq. A big thank you also to the whole team at Taniq for being extremely helpful (and patient with the mess I sometimes left behind). Specifically, thank you Rob for being an excellent supervisor, and my first point of contact for the smallest of questions. Also a big thank you to Fred, Rutger and Damiaan for helping me tremendously with the experimental setup and the parts that needed to be purchased. I think you reduced several weeks from the time I would have otherwise taken to graduate. Finally, thank you to Carlo Socci, who supervised the starting few months of this project from Taniq's side.

The academic guidance from my supervisors at TU Delft was of course one of the main reasons I have been able to reach the stage to write this report, and for that, I most certainly must thank Prof. Boyang Chen and Prof. Julien van Campen. After having completed the non-linear modelling course taught by Prof. Chen at TU Delft, I was certain that he would be the ideal person to guide this project - with its heavy dose of state-of-the-art FEA techniques and its large nonlinearities. At the same time, despite not having been taught by Prof. van Campen, just a brief literature survey confirmed that with anything filament wound, Prof. van Campen would be the best source of guidance. I am extremely grateful that I got the opportunity to work with both of them, and would certainly love to work with them again, should opportunities arise to further this work.

Living away from home hasn't been as challenging as I thought it would, thanks to my mini-family here in Delft. Thank you to Radha and Sankalp for always being my top 2 dialled numbers here in Delft (and probably also in Mumbai). I think the two of you have contributed to this thesis in ways more

than I can express here. I would also like to thank Camill, Jonas, Marco, and Akshay for all the input you provided during the project.

Finally, and probably the most strongly, I would like to thank my parents for giving me the opportunity to pursue this course, and also for supporting me emotionally and financially throughout my two years here in the Netherlands. It is a bit redundant to say, but this would definitely not have been possible without you.

Ahaan Bhosale
Delft, December 2022

Abstract

This project aims at developing a model to predict the damage initiation and propagation in a cylindrical filament-wound cord-rubber structure under internal pressurization using non-linear FEA, and is conducted in cooperation with TANIQ BV, Netherlands. Cord-reinforced rubber composites are used in several safety-critical industries such as oil and gas and civil plumbing. Despite their widespread use, limited research is available that focuses on the single-cycle damage phenomenon that may occur in events such as over-pressurization.

The aim of this project is to close this knowledge gap by developing a theory that accounts for the key damage modes present in CRC structures. This involves experimental studies for material characterization and identification of relevant damage modes, the creation of a novel fibre overlap model that accurately replicates the meso-level filament-wound structure, and translation of the experimentally verified damage modes into functional damage initiation and propagation laws using a global-local FEA model. Verification of the created damage model is done experimentally on samples manufactured and tested at TANIQ, with differences between model predictions and experimental burst pressures being $\approx 6.5\%$. This is a marked improvement over Taniq's current FEA model, which overpredicts the solution by $\approx 27\%$.

The successful implementation of this model would help industries like TANIQ build efficient, strong, and lightweight rubber composite parts for various industries, thus adapting aerospace design principles to the development of more commonplace apparatus.

This page was intentionally left blank.

Contents

This page was intentionally left blank.

Nomenclature

Abbreviations

CRC	Cord-rubber composite
FEA	Finite element analysis (structural)
PA	Polyamide
RFL	Resorcinol Formaldehyde Latex
RUC	Repeating unit cell
RVE	Representative volume element
SCL	Slow cyclic loading

Symbols

α	Winding Angle wrt. longitudinal axis
α_g	Neutral winding angle
λ_i	Principle stretch in the i$^{\text{th}}$ direction
$\mathbb{R}$	Real coordinate space
σ	Cauchy Stress
$\mathbf{b}$	Left Cauchy-Green stretch tensor
$\mathbf{C}$	Right Cauchy-Green stretch tensor
$\mathbf{E}$	Green-Lagrange strain tensor
$\mathbf{F}$	Deformation gradient
$\mathbf{K}$	Tangent stiffness matrix
$\mathbf{S}$	2$^{\text{nd}}$ Piola-Kirchhoff stress
$\mathcal{B}_0$	Body in reference frame
$\mathcal{B}_t$	Body in current frame at time t
ϕ	Dwell angle
Ψ	Helmholtz potential (strain energy density functional)
τ	Kirchhoff stress
ξ	Deformation
$I_i(M)$	i$^{\text{th}}$ invariant of the arbitrary tensor M
$\overline{\mathbf{M}}$	Isochoric (volume preserving) portion of arbitrary tensor M
G	Fracture toughness

J	Jacobian (volume ratio)
p	Filament winding parameter
S_{ij}	i,jth term of compliance matrix
t	Traction

1

Introduction

1.1. Context and Motivation

Cord-rubber composites (CRCs) are an interesting branch of composites that use highly tough and flexible rubber elastomers as the matrix material while using stiff twisted cord constructions as strengthening additives. Usually, these structures are used under internal pressurisation such that the rubber with its low modulus and high failure strain provides flexibility and acts as a leak-proof barrier, while the high-modulus reinforcing cords provide the needed load-carrying capacity. These properties allow these composites to be used in some of the most demanding applications, where large deformations should be sustained without product failure.

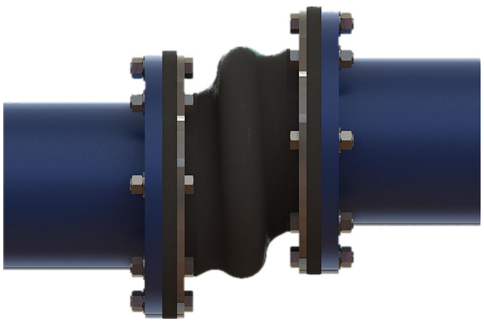

(a) Expansion joint

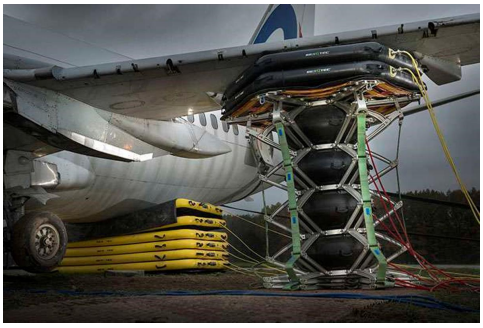

(b) Lift bag

(c) Floating dredging hose

(d) Pipe-plug

Figure 1.1: Various CRC products in use

One of the most prominent industries where cord-rubber composites are used is the tyre industry, where a steel grid reinforcement forms the structural backbone of the tyre for the various on and off-road loads.

CRC dredging hoses are also commonly used in the mining and construction industries, where they are tasked with the conveyance of silt/gravel and other abrasive slurries. The civil pipeline and oil and gas industries make extensive use of expansion joints to allow a flexible coupling between adjacent fluid transmission lines, while even safety-critical industries such as search and rescue companies use CRC products such as lift-bags to efficiently displace heavy loads.

This thesis project is conducted in cooperation with Taniq B.V, a dutch company specialising in producing such rubber composite products via their proprietary design software and robotic production solutions. Despite the varied form factors and applications of the products, all Taniq's products share a common manufacturing method base in the form of tape/filament winding. Additionally, most products are also loaded via internal pressurisation. Due to these commonalities, it is theorised that most of these CRC products will have common geometrical features, material tendencies, and damage modes that lead to eventual product failure. This research aims to identify these parameters using a representative CRC cylindrical close-ended pressure vessel, and then create an FEA model to predict its single-cycle burst pressure.

Single-cycle burst is a critical safety and performance-related parameter of highly pressurised CRC components such as pipe-plugs, lift-bags and conformable pressure vessels. The latter also has massive potential in powering the sustainable automobiles and aircraft of tomorrow. It has been found that the response of these rubber composites is highly dependent on the fibre placement and fibre stiffness [1] Despite this, most publications focus extensively on fatigue, hysteresis, and the viscoelastic nature of rubber to define CRC damage, which may not be relevant for single cycle burst. Thus, the aim of this project is to close this research gap and investigate a suitable damage model for the single-cycle burst of CRCs.

1.2. Research Questions

Based on the objectives of this project, the primary research question for this project may be defined as:

Primary Research Question

How can a non-linear finite element model be created to capture the relevant failure modes in a close-ended cylindrical cord-rubber composite structure and predict its single cycle burst pressure under a quasi-statically varying internal pressure to a degree acceptable to enable engineering decision-making?

Careful unpacking of this research question allows for the definition of several research sub-questions. To start with, emphasis has been placed on capturing the *relevant* damage modes. This leads to the question:

1. Which damage modes in a cylindrical filament wound CRC structure are relevant to drive its eventual burst under internal pressurisation?

    (a) How can the relevant damage modes that drive product failure be identified using literature, numerical models, or physical experiments?
    (b) How can the results of these singular (numerical) experiments be translated to the CRC structural scale to arrive at meaningful conclusions about the relevant damage modes?
    (c) What specimen design should be chosen such that it is representative of typical failure modes in most CRC products?

With the decision to model the structure using a nonlinear FEA model comes the need to define the exact modelling methodology. This helps formulate the next set of research sub-questions:

2. Which FEA modelling methodology should be utilized to capture the identified damage modes in the most efficient manner?

   (a) Which modelling scale allows accurate representation of the pre-identified damage modes?
   (b) Which damage laws are appropriate to model failure in each failure mode?
   (c) How can relevant material and structural data be obtained to capture the pre-damage and damage response of the CRC specimen?

Finally, the solution must be computationally efficient and must deliver a solution that is able to *enable engineering decision-making*. This means that the proposed solution must compare well to experimental data whilst also being quick enough to deliver results during the product design phase. This defines the final set of research questions:

3. How can experimental burst tests be conducted to validate the FEA model while allowing maximum data to be collected per experiment?

   (a) Which measurements taken during the burst test would help to validate the created FEA model?
   (b) How can a test setup be designed to allow the logging of these measurements continuously in real time during each burst test?

1.3. Report Layout

The report begins with a concise overview of literature for modelling methods for cord-rubber composite structures in chapter 2, along with a section on automated CRC product design and production at Taniq. This is followed by a description of fibre patterns created via filament winding in chapter 3, along with the description of a simplified fiber overlap model created to model the undulating fiber geometry for this project. Chapter 4 details the methodology followed to create the FEA model, whilst chapter 5 defines the material models for the same. The FEA model itself is described in chapter 6, the results of which are described and used for parametric studies in chapter 7. Finally, the various experimental campaigns to calibrate the material models and conduct the burst tests are highlighted in chapter 8.

This page was intentionally left blank.

2

Cord-Rubber Composites : A Literature Review

This chapter aims to acquaint readers with the analysis methods, production processes, and behavioural characteristics of cord-rubber composites. The main focus lies in presenting the work done in literature to model both the pre-damage and damage response of cord-rubber composites. The content presented here is an abridged version of the literature review report written by the author of this study. Interested readers may refer to [2] for a complete overview. Additionally, snippets of relevant literature are provided throughout the report when certain concepts are introduced to aid smoother flow and better readability.

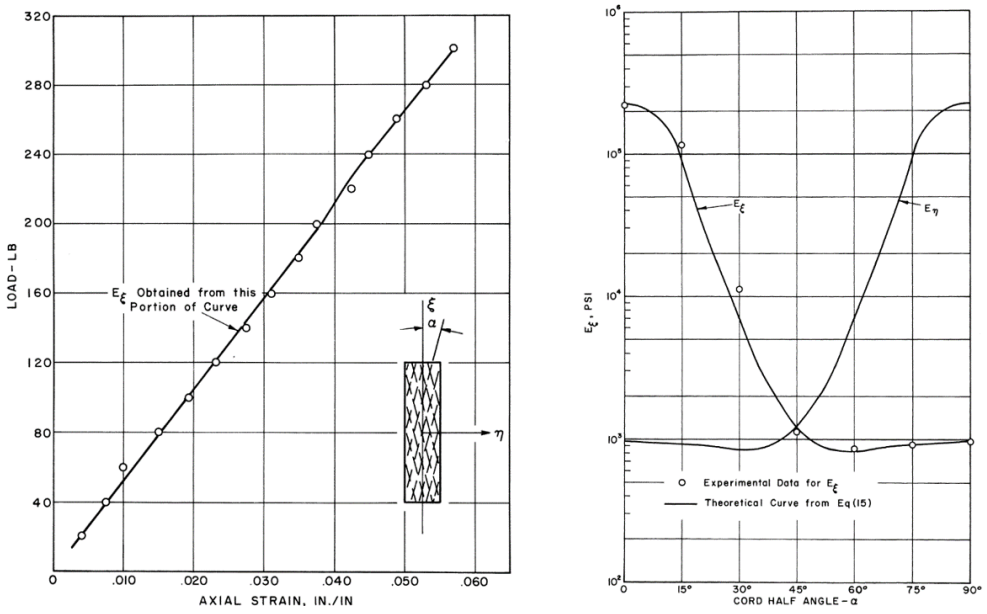

(a) Small strain region chosen for tensile modulus estimation

(b) Tensile modulus prediction for various cord angles

Figure 2.1: Small strain CRC moduli prediction using Clarke's theory [3]

2.1. Legacy CRC Modelling Techniques

In the context of this chapter, 'legacy' modelling techniques refer to those analyses which are highly simplified and offer quick solutions to the pre-damage response of CRC structures with minimal com-

putational cost. Often, linearised methods are used here that are direct adaptations of conventional lamination theory for polymer composites [4].

One such early attempt to linearise the response of rectangular CRC specimens was by Clark in 1960 [3]. He analytically solved for the elastic moduli in a laminated cord-rubber sheet based on the principles of linearly-elastic orthotropic materials, and thereby was able to predict its stress state. For arbitrary cord angles, Clark defined 14 elastic constants that were to be used in groups depending on the loading applied to the composite. For load cases in which all the fibres were either in tension or compression, a statically determinate set of solutions was obtained, which yielded the elastic constants as well as inter-laminar shear stresses. On the other hand, for a combination of tensile and compressive forces among the cords, a statically indeterminate set was formed, for which only approximate solutions were possible. Despite showing a decent correlation with experimental data, this set of predictions was valid only for extremely small strains in the linear limit as shown in figure 2.1a.

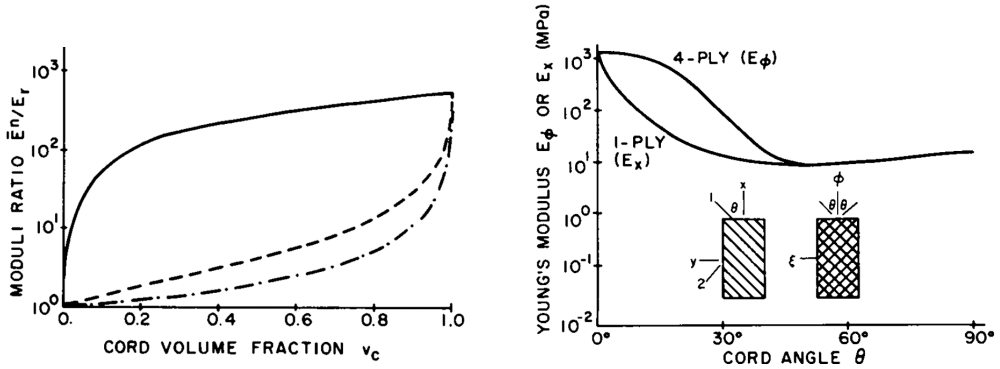

(a) Variation of elastic modulus with cord volume fraction

(b) Variation of elastic modulus with cord bias angle

Figure 2.2: Parametric studies by Walter based on rectangular CRC specimen [1]

Following a similar methodology, Walter [1] published an extensive study to predict the stress state in cord-rubber composites for tyre applications. For single-ply CRC systems with a single cord bias direction, he attempted to build a system of engineering constants based on classical lamination theory and the rule of mixtures. For multi-ply systems, netting analysis was attempted to predict tyre performance, on the basis of which several parametric studies (figure 2.2) were conducted to compare the effects of factors such as cord volume fraction and cord bias angle on the elastic properties of the composite.

Ford et. al [6] expanded the multi-ply analysis by Walter to focus on the inter-ply shear strains. They hypothesised that the shear-coupling response in two-ply ($\pm\alpha^\circ$) CRC laminate has a significant influence on the specimen stiffness. Here, the in-plane liner compliance matrix coupling term 'S16' was used to predict the interlaminar shear stresses in a two-ply CRC laminate. Using the developed analytical model, it was predicted that the shear-coupling for a single ply would be maximum at ($\alpha \approx 20^\circ$), and would reverse directions at ($\alpha \approx 66^\circ$) - see figure 2.3. Additionally, it was shown that for a two-ply composite, maximum shear strains lie at the free ends, and drop off rapidly towards the centre of the specimen - see figure 2.4. This highlights an important damage initiation mechanism for CRC composites with open ends but is not as critical in axisymmetric products.

Rule of mixtures type homogenisation approaches also were fairly common to describe CRC behaviour using moduli. Akasaka and Hirano [7] published a list of equations that can be used to formulate the ply properties if the individual cord and rubber moduli and the fibre fraction are known. Few publications have also quoted the equations by Halpin and Tsai [8] developed for conventional composites to the same effect. Similar analyses have also been carried out specifically for tyre constructions by Gough [9], and Patel et. Al.[10].

Even though these methods were reasonably successful in predicting the small strain behaviour of CRCs using linearised moduli, the actual behaviour of these materials is far from linear. Cord twist, material non-linearity and finite displacements, all lead to deviations from linear elastic behaviour, and thus

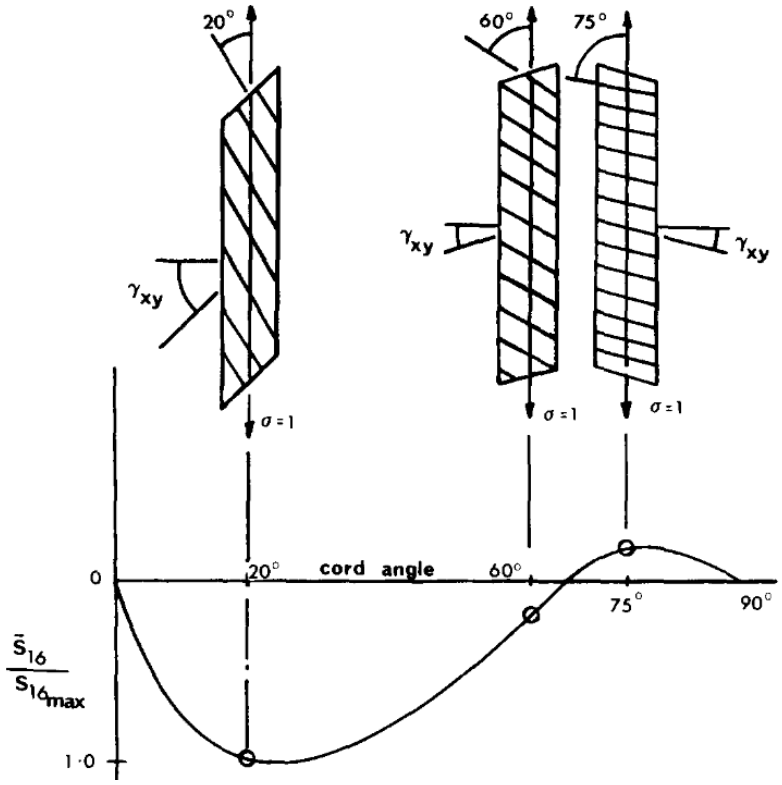

Figure 2.3: Variation in the analytical prediction of shear-coupling compliance with cord angle [5]

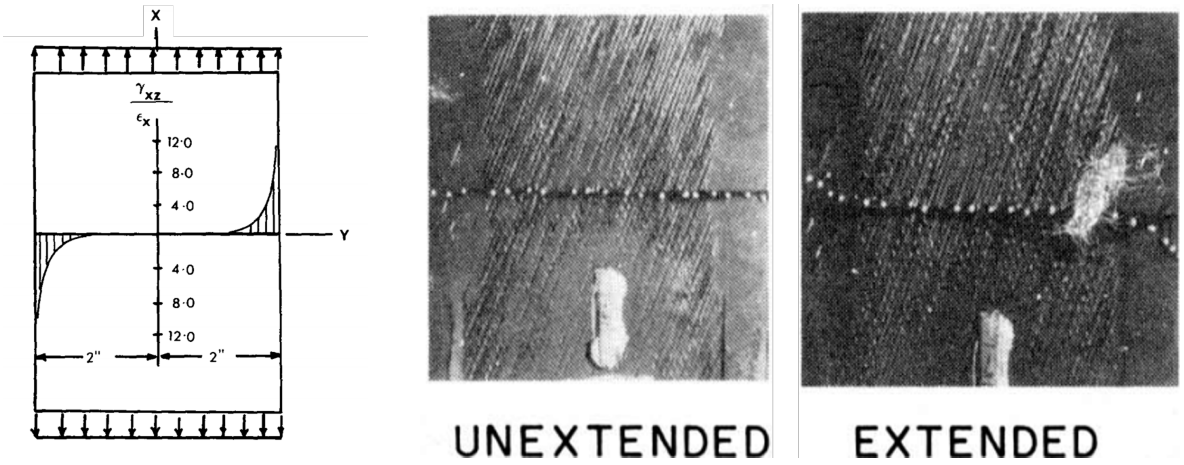

(a) Analytical shear strain prediction

(b) Pin test to show shear strain distribution

Figure 2.4: Theoretical and experimental shear strain distribution along a 2 ply CRC laminate [6]

more accurate modelling techniques are needed. This is the subject of discussion in the next section.

2.2. Hyperelastic Materials

2.2.1. Basics of Nonlinear Solid Mechanics

The foundations of non-linear solid mechanics are based on the separation of the reference (often the same as undeformed) configuration of a body $\mathcal{B}_0 \subset \mathbb{R}^3$ at time $t = 0$ and the current state of the body

$\mathcal{B}_t \subset \mathbb{R}^3$ at a time t. The deformation $x = \chi(X, t)$ may then be described as a map between the reference and the current configurations of the body. Since this definition is parameterised by coordinates in the reference configuration, it is known as the Lagrangian formulation.

The deformation gradient $\mathbf{F}$ may then be described as a useful measure of deformation as in equation (2.1). Here, $\nabla\mathbf{u}(\mathbf{X})$ is the displacement gradient. The determinant of $\mathbf{F}$ is known as the Jacobian J and signifies the volume ratio between the deformed and reference states.

$$\mathbf{F} = \frac{\partial \chi(\mathbf{X}, t)}{\partial \mathbf{X}} = \mathbf{I} + \nabla\mathbf{u}(\mathbf{X}) \tag{2.1}$$

$$J = \det \mathbf{F} > 0 \tag{2.2}$$

The polar decomposition of the deformation gradient helps to define a useful measure of strain in $\mathcal{B}_0$ known as the right Cauchy-Green stretch tensor given by $\mathbf{C} = \mathbf{F}^{\mathbf{T}}\mathbf{F}$. A similar left Cauchy-Green tensor may be defined in $\mathcal{B}_t$ as $\mathbf{b} = \mathbf{F}\mathbf{F}^{\mathbf{T}}$. Then, to fulfil the condition of having zero strain in the undeformed configuration, the Green-Lagrange strain tensor may be defined as:

$$\mathbf{E} = \frac{1}{2}(\mathbf{C} - \mathbf{I}) \tag{2.3}$$

The most fundamental measure of stress can be derived from Cauchy's theorem and is known as the Cauchy stress tensor σ. This is a measure of the true stress in the current configuration and relies on an infinitesimal force vector df on an infinitesimal area dA.

$$\mathbf{t} \equiv \frac{\mathrm{df}}{\mathrm{dA}} = \boldsymbol{\sigma} \cdot \mathbf{n} \tag{2.4}$$

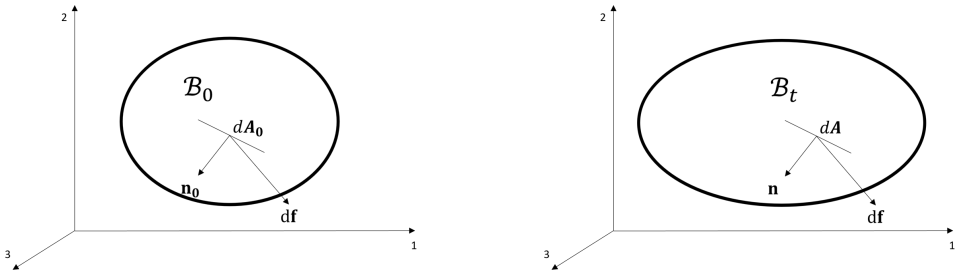

(a) 1st PK Stress **(b)** Cauchy Stress

Figure 2.5: Stress measures [11]

A similar measure of stress may be defined in $\mathcal{B}_0$ using the same infinitesimal force df over the undeformed initial area element dA_0. This is known as the 1st Piola-Kirchhoff stress tensor $\mathbf{P}$, and is representative of the engineering stress.

$$\tilde{\mathbf{t}} \equiv \frac{\mathrm{d}\mathbf{f}}{\mathrm{d}A_0} = \mathbf{P} \cdot \mathbf{n_0} \tag{2.5}$$

The relation between $\mathrm{d}A_0$ and $\mathrm{d}A$ is provided by the Nanson's formula as:

$$\mathbf{n}\mathrm{d}A = J(\mathbf{F})\mathbf{F}^{-\mathrm{T}}\mathbf{n}_0 \, \mathrm{d}A_0 \tag{2.6}$$

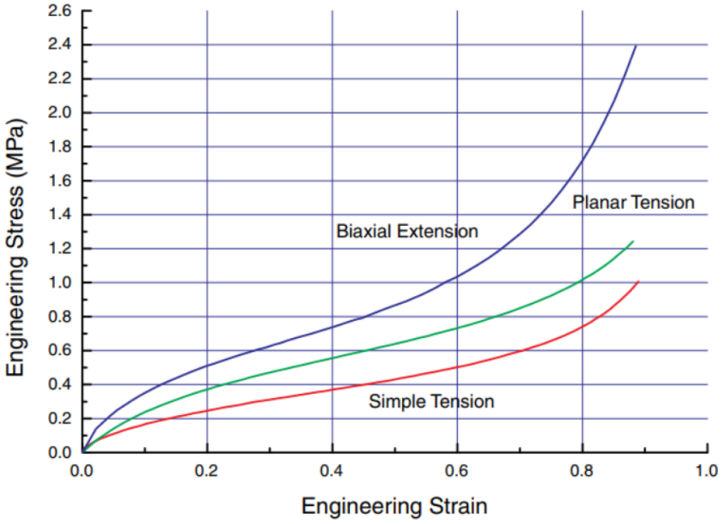

Figure 2.6: Typical rubber stress-strain response for monotonic loading in 3 deformation modes [12]

Finally, to complete the description of stress in $\mathcal{B}_0$, the 2$^{\text{nd}}$ Piola-Kirchhoff stress tensor $\mathbf{S}$ is defined that uses a 'pull-back' of the force from the current configuration to the reference configuration via the deformation gradient.

$$\tilde{\tilde{\mathbf{t}}} = \frac{\mathbf{F}^{-1}\,\mathrm{d}\mathbf{f}}{\mathrm{dA}} = \mathbf{S}\cdot\mathbf{N} \tag{2.7}$$

2.2.2. Hyperelastic Materials

Hyperelastic materials are most commonly used to define the stress-strain response of rubber-like materials or any highly deformable solid material - see figure 2.6. For such materials, the work done is independent of its loading path [13], [14]. These materials provide a convenient description for highly non-linear materials at finite strains by describing the material behaviour via the Helmholtz energy potential (Ψ) which is defined per unit volume. A phenomenological approach is commonly utilized where experimental data is used to define expressions for the Helmholtz potential - often as a function of the deformation gradient ($\mathbf{F}$). Since various measures of stretch and strain such as $\mathbf{C}$ and $\mathbf{E}$ are also functions of the deformation gradient, the potential may also be expressed in terms of them as shown in equation (2.8). Here, the liberty is taken to express different potentials using the same letter Ψ with the understanding that they should be read along with their arguments.

$$\Psi = \Psi(\mathbf{F}) = \Psi(\mathbf{C}) = \Psi(\mathbf{E}) \tag{2.8}$$

Being a thermodynamic potential, the stress measures may be obtained by differentiating the Helmholtz free energy with respect to the conjugate strain measure. Therefore,

$$\mathbf{S} = \frac{\partial\Psi(\mathbf{E})}{\partial\mathbf{E}} = 2\frac{\partial\Psi(\mathbf{C})}{\partial\mathbf{C}} \tag{2.9}$$

Other stress measures may then be arrived at using standard transformations using the Jacobian ($\mathbf{J}$). These are not discussed further, but an interested reader may refer to the discussion in [2].

For this project, the rubber will be considered as an isotropic continuum. If a material is deemed isotropic, then by the representation theorem of invariants [15] its Helmholtz potential may be expressed in terms of its principle invariants.

$$\Psi = \Psi[I_1(\mathbf{C}), I_2(\mathbf{C}), I_3(\mathbf{C})] \tag{2.10}$$

Where:

$$I_1(\mathbf{C}) = \mathrm{tr}\,\mathbf{C} = \lambda_1^2 + \lambda_2^2 + \lambda_3^2 \tag{2.11}$$

$$I_2(\mathbf{C}) = \frac{1}{2}\left[(\mathrm{tr}\mathbf{C})^2 - \mathrm{tr}\left(\mathbf{C}^2\right)\right] = \mathrm{tr}\,\mathbf{C}^{-1}\ \det\ \mathbf{C} = \lambda_1^2\lambda_2^2 + \lambda_1^2\lambda_3^2 + \lambda_2^2\lambda_3^2 \tag{2.12}$$

$$I_3(\mathbf{C}) = \det\mathbf{C} = J^2 = \lambda_1^2\lambda_2^2\lambda_3^2 \tag{2.13}$$

From equations (2.11) to (2.13), it is apparent that the invariants can be expressed in terms of the principle stretches λ_i. Hence, the strain energy potential itself can also be expressed in terms of λ_i. In these cases, the stresses can be calculated via the chain rule applied on equation (2.9).

2.3. Rubber Material Models

Over the years, several researchers have used the above constitutive hyperelastic theory to define physically motivated or phenomenological expressions for the Helmholtz potential in terms of the Cauchy stretch tensor ($\mathbf{C}/\mathbf{b}$), its principle invariants (I_i) or the principle stretches (λ_i). Some of these expressions for isotropic rubber are presented in this section.

2.3.1. Neo-Hookean Model

One of the simplest and oldest phenomenological expressions for isotropic rubber is the Neo-Hookean model [16] given by equation (2.14). Here, μ_{10} is the initial shear modulus. Being a single-term model, it is unable to capture the upturn in the stress-strain data and is thus best used for small strains.

$$\Psi = \frac{\mu_{10}}{2}(\bar{I}_1 - 3) \tag{2.14}$$

2.3.2. Mooney-Rivlin Model

An improvement over the Neo-Hookean model is the two-term phenomenological Mooney-Rivlin model [17] given by equation (2.15). Due to the additional term, it is able to capture the behaviour up to moderate strains, but it still misses the upturn in the hyperelastic response.

$$\Psi = C_{10}\left(\bar{I}_1 - 3\right) + C_{01}\left(\bar{I}_2 - 3\right) \tag{2.15}$$

2.3.3. Ogden Model

In order to better capture the entire response in the applied strain domain, Ogden [18] created a phenomenological model given by equation (2.16) in terms of the principle stretches. Here, $\mu = \sum_{p=1}^{N} \mu_p\alpha_p$ is the shear modulus and α_p is a set of dimensionless constants.

$$\Psi = \sum_{p=1}^{N} \frac{\mu_p}{\alpha_p}\left(\lambda_1^{\alpha_p} + \lambda_2^{\alpha_p} + \lambda_3^{\alpha_p} - 3\right) \tag{2.16}$$

The Ogden strain energy potential forms a very general description of hyperelasticity from which other functionals may be derived. For example, the Mooney-Rivlin model may be derived with $N = 2$, $\alpha_1 = 2$ and $\alpha_2 = -2$. Similarly, the Neo-Hookean model may be derived using $N = 1$ and $\alpha_1 = 2$.

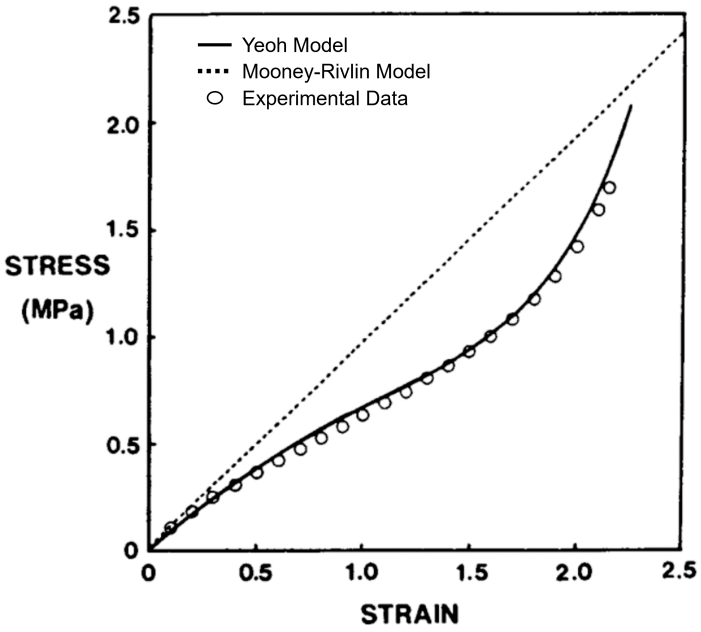

Figure 2.7: Comparision of the shear response of the Mooney-Rivlin and Yeoh model against experimental data for filled rubbers [19]

2.3.4. Yeoh Model

Most natural rubbers used in engineering applications have reinforcing fillers such as carbon black that form physical and chemical bonds with the polymer chains [16]. Physical observations showed that the shear moduli for such filled rubbers is highly non-linear with deformation. If the Mooney-Rivlin model is considered, then the shear modulus may be specified as shown in equation (2.17). This is clearly linear with a constant slope.

$$\mu = 2\left(\frac{\partial \Psi}{\partial I_1} + \frac{\partial \Psi}{\partial I_2}\right) = 2\left(\mu_1 + \mu_2\right) > 0 \tag{2.17}$$

To counter this issue, Yeoh [19] created a phenomenological model for carbon-black filled elastomers with the needed shear-stiffening response in the large strain domain - see figure 2.7. The model was based on data for filled rubbers by Kawabata [20], which suggested that $\partial\Psi/\partial I_2$ should be set to zero. Thus, a three-term Helmholtz potential was proposed as shown in equation (2.18), where I_2 does not appear.

$$\Psi = c_1\left(I_1 - 3\right) + c_2\left(I_1 - 3\right)^2 + c_3\left(I_1 - 3\right)^3 \tag{2.18}$$

2.3.5. Arruda-Boyce 8 Chain Model

To round off the discussion in this section, a non-phenomenological model is presented. The Arruda-Boyce 8 chain model [21] is a statistical model in which the calibration parameters are physically motivated by the chain orientations during the deformation of a 3D elastomeric unit cell. The first three terms of the Helmholtz potential are presented in equation (2.19), where μ denotes the shear modulus, and n denotes the number of segments in a chain.

$$\Psi = \mu\left[\frac{1}{2}\left(I_1 - 3\right) + \frac{1}{20n}\left(I_1^2 - 9\right) + \frac{11}{1050n^2}\left(I_1^3 - 27\right) + \ldots\right] \tag{2.19}$$

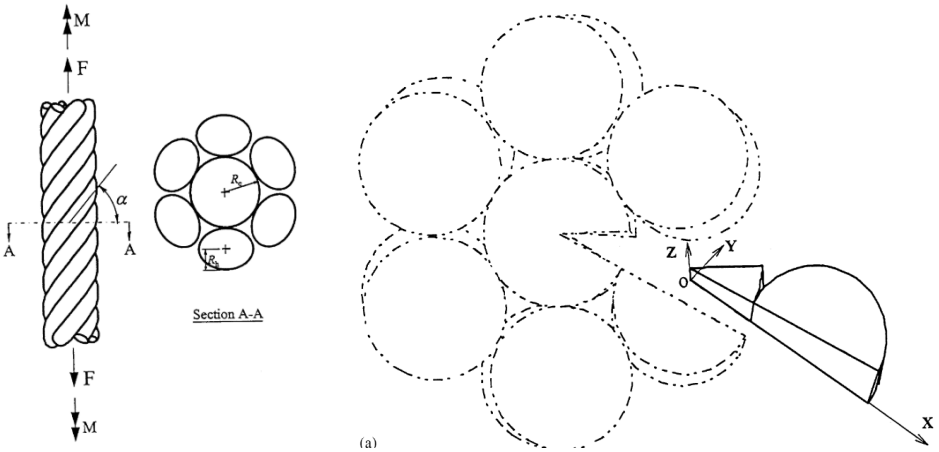

(a) 7-strand wire rope **(b)** Reduced cross section considered due to symmetry

Figure 2.8: Reduced section and mesh considered for the twisted cord [27]

2.3.6. Newer Models

Newer models have since been formulated that either account for more phenomena such as hysteresis, or are able to capture deformation more accurately using limited constitutive parameters. Külcü [22] recently published a model using a combination of exponential and polynomial functions (see equation (2.20)) which is able to use just two constants to capture various deformation modes up to the large strain domain. A good match is seen with experimental data for uniaxial and equi-biaxial tension, and pure shear.

$$\Psi = \mu \left[f\left(I_1, \alpha\right) + f\left(I_2, -\frac{\alpha}{16}\right) + \ln\left(\frac{1}{\alpha} f\left(I_1, 1\right) + 1\right)\right] \tag{2.20}$$

Where

$$f(x, y) = \frac{\alpha}{y}\left[e^{y[x-3]} - 1\right] \tag{2.21}$$

More advanced models such as the MORPH rubber model [23]–[25] are able to capture effects such as Mullin's effect [26], hysteresis and permanent set. This is done using a phenomenological additive decomposition of the Kirchhoff stress tensor into the 'limiting stress' component which represents the basic Neo-Hookean like stress state and an 'additional stress' component which characterises the hysteresis. In all, 8 material constants are required to calibrate this model via a combination of cyclic and static experiments. Since cyclic loading is not a focus of this project, such models are not considered further.

2.4. Fibre Models

The reinforcement of most CRC consists of twisted cords, which have two levels of twist - twisted filaments that make up a single yarn and then twisted yarns that make a cord. This forms a complex 3D structure whose behaviour needs to be understood to capture important coupling effects and also points of stress concentration for damage.

Despite the presence of several analytical models that treat twisted cords as ideally helical structures [28], [29], the true non-linearity in the mechanical response can most efficiently be predicted using an FEA model. Jiang et. al. [27] created an FEA model to study the performance of a twisted steel chord with an untwisted central core while accounting for plastic yielding and frictional slip. Boundary conditions based on the helical symmetry of the cord were used to define a reduced model that is $\frac{1}{12}^{\text{th}}$

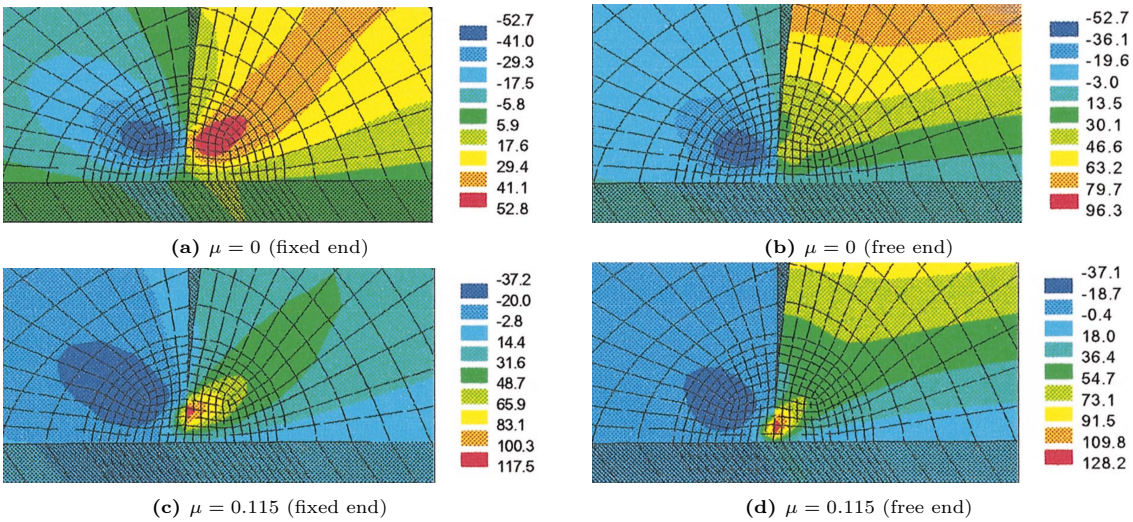

(a) $\mu = 0$ (fixed end)

(b) $\mu = 0$ (free end)

(c) $\mu = 0.115$ (fixed end)

(d) $\mu = 0.115$ (free end)

Figure 2.10: Effect of friction coefficient (μ) on the shear stress in a twisted cord for fixed and free-end loading [27]

of the circumference and only a single element thick (see figure 2.8).

Plastic yielding of the fibres was accounted for using a von-Mises yield criteria and a bilinear hardening law. Contact formulation is used with Coulomb friction sliding to model the effects of inter-fibre friction on the rope mechanical response. Excellent results are seen when compared with experimental data. All the relevant non-linearities were captured (see figure 2.9). One of the key observations during the axial loading simulation was that there is an increasing contact pressure between neighbouring fibre bundles within a single cord with increasing load. This leads to localised yielding at the points of contact ($R = R_c$) with the points of maximum stress lying around this localised yield zone (see figure 2.9).

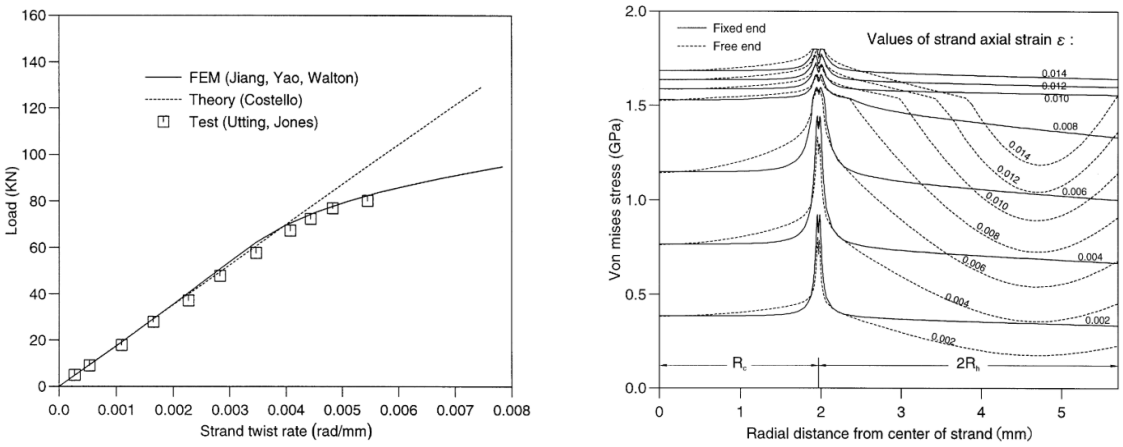

(a) Comparison of twisted cord model with experimental data

(b) Mises stresses along radius of cord under uniaxial tensile loading

Figure 2.9: Twisted cord analysis results by Jiang [27]

The effect of various friction coefficients is also studied - see figure 2.10. There is a significant increase in localised shear stress when friction between yarns is considered vs the case when friction is ignored. These effects are highly localised and play almost no role in the global load-displacement behaviour. However, they may be relevant for characterising failure.

An alternative route to modelling twisted cords is to homogenise the material response. Li et. al. [30] created a phenomenological hyperelastic model that captures the behaviour of coated and twisted nylon-66 cords under monotonic and cyclic loading. The strain energy potential is expressed as an infinite

power series, with a higher number of terms yielding better accuracy (see equation (5.2)). Experimental tests (see figure 5.4) provided an insight into the typical elastomer-like hyperelastic response of the fibre. This is elaborated on in more detail in section 5.2 due to its relevance in defining a material model for the fibre.

In Li's study, it was noticed that the yield strain of the twisted cord structure was $\approx 60\%$ higher than that of a single filament. Thus, the effects of the twist on the structural properties of the cord need further explanation. Recently, Teng et. al [31] carried out an experimental, numerical and analytical investigation of yarn twist on the tensile loading properties of twisted fibre yarns. Three samples with differing degrees of twist were analysed using the analytical and numerical models. Excellent agreement was observed with experimental data (see figure 2.12).

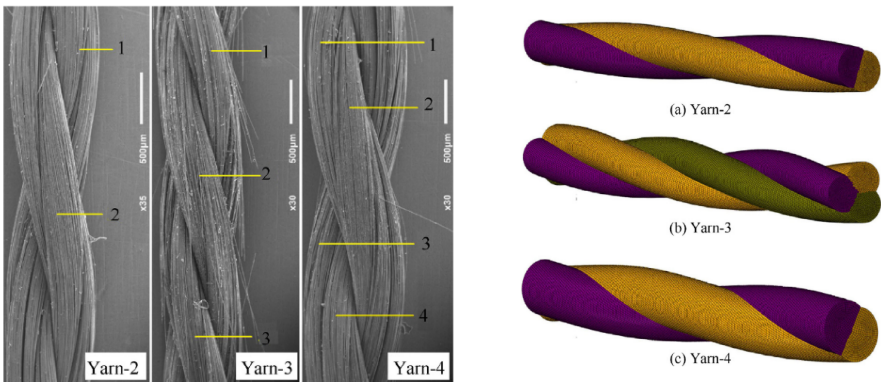

(a) SEM images of cords under consideration **(b)** FEA models

Figure 2.11: Twisted cords considered for study by Teng [31]

It is noticed that there is a marginal decrease in stiffness with an increasing twist in the cord, but rapidly increasing tensile strength. This is because twisting increases the compaction and frictional interaction between the yarns and thus improves the uniformity of the bundle. This also reduces the dispersion of the tensile strength within the cord due to manufacturing and other defects. Another key difference between figure 2.12 and the response obtained by Li et. al (figure 5.4 in section 5.2) is that the cord considered by Teng et. al. is uncoated while the one considered by Li et. al. is coated with an elastomeric layer. This is reflected in the response of the fibre, where the curve in figure 5.4 shows a region of non-linearity while the data in figure 2.12 is almost linear. This highlights the possibility that the cord coating is the source of nonlinearity in the response.

It is also postulated that inter-yarn friction plays a major role in higher tensile strength. The friction creates even load sharing within the fibre bundle and reduces the sensitivity of the yarn to defects. Localisation due to single filament failure is also limited as neighbouring filaments can carry load via frictional shear transfer. This effect lasts as long as the fibre remains loaded. However, on unloading, subsequent cycles undergo reducing ultimate strengths. Thus, friction is also relevant for fatigue analyses.

2.5. CRC Models

With an overview of the state of the art in cord and rubber modelling, the current advances in CRC modelling can be explored. Despite the dearth of literature on this topic, available literature may be broadly classified into continuum models and explicit models. In continuum models, the cord-fibre structure is treated as a single homogenous material, while in explicit models, efforts have been made to individually capture the behaviour of each material into the model. Both of these techniques will be briefly discussed in this section.

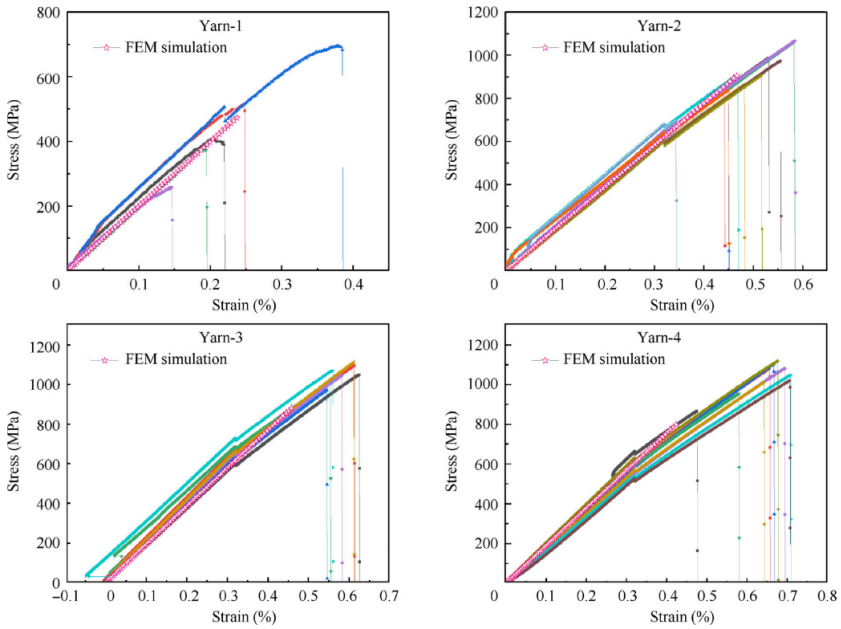

Figure 2.12: Uniaxial stress-strain response for twisted cords [31]

2.5.1. Continuum Models

CRCs are created using a base rubber matrix and embedded directional fibre strengthening. If treated as a continuum, this means that the resulting material is strongly anisotropic due to the bias of the fibres along with the large stiffness difference between the cord and the rubber. Thus, homogenised methods of CRC modelling aim at fitting phenomenological expressions to Spencer's constitutive theory [32] for anisotropic solid continua.

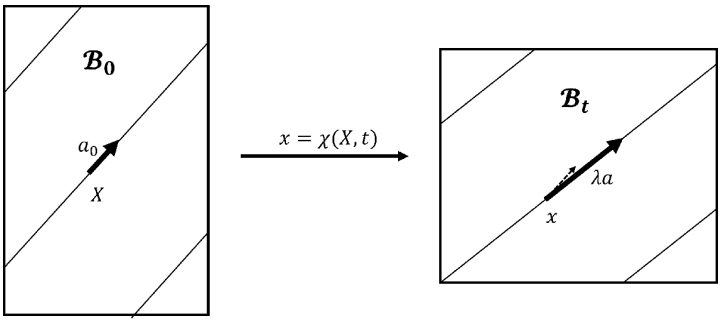

Figure 2.13: Body with single direction reinforcement in initial and current configurations

Spencer's model may be understood using figure 2.13. Here, a_0 is the unit direction vector of the reinforcement in $\mathcal{B}_0$ while a is the unit direction vector of the same fibre in $\mathcal{B}_t$. Then, the stretch may be expressed as:

$$\lambda \mathbf{a}(\mathbf{x}, t) = \mathbf{F}(\mathbf{X}, t)\mathbf{a_0}(\mathbf{X}) \tag{2.22}$$

Then, since a is a unit vector, the square of stretch may be expressed as:

$$\lambda^2 = \mathbf{a}_0 \cdot \mathbf{F}^{\mathrm{T}}\mathbf{F}\mathbf{a}_0 = \mathbf{a}_0 \cdot \mathbf{C}\mathbf{a}_0 \tag{2.23}$$

Thus, the fibre stretch depends on the fibre orientation in the reference configuration and the stretch measure. These should be incorporated explicitly in the strain energy potential. Since the directionality

along a fibre - down to up or up to down should not affect the potential, an even function of a_0 is chosen. Then, the potential may be represented as:

$$\Psi = \Psi(\mathbf{C}, \mathbf{a_0} \otimes \mathbf{a_0}) \tag{2.24}$$

In terms of invariants, according to [33], apart from equations (2.11) to (2.13), two additional invariants need to be defined to complete the integrity basis of $\mathbf{C}$ and $\mathbf{a_0} \otimes \mathbf{a_0}$.

$$I_4(\mathbf{C}, \mathbf{a}_0) = \mathbf{a}_0 \cdot \mathbf{C}\mathbf{a}_0 = \lambda^2, \quad I_5(\mathbf{C}, \mathbf{a}_0) = \mathbf{a}_0 \cdot \mathbf{C}^2\mathbf{a}_0 \tag{2.25}$$

Using the above formulation, the Helmholtz potential may be represented phenomenologically as a sum of isotropic and anisotropic parts.

$$\Psi(\mathbf{C}, \mathbf{a_0} \otimes \mathbf{a_0}) = \underbrace{\Psi(\mathbf{C})}_{\Psi_{iso}} + \underbrace{\Psi(\mathbf{a_0} \otimes \mathbf{a_0})}_{\Psi_{aniso}} \tag{2.26}$$

A similar approach may be used to define multiple families of fibres in a hyperelastic matrix using their own set of direction vectors. For instance, for two fiber families a_0 and b_0, the strain energy potential can be represented as:

$$\Psi = \Psi(\mathbf{C}, \mathbf{a_0} \otimes \mathbf{a_0}, \mathbf{b_0} \otimes \mathbf{b_0}) \tag{2.27}$$

A total of nine invariants will now be present. Apart from the original set of invariants equations (2.11) to (2.13) , an additional two pseudo-invariant sets will be defined similar to equation (2.25) for $\mathbf{b_0} \otimes \mathbf{b_0}$ and C. Finally, two invariants given by equation (2.28) will be defined to account for the coupling between the two families of fibres.

$$I_8(\mathbf{C}, \mathbf{a}_0, \mathbf{b}_0) = (\mathbf{a}_0 \cdot \mathbf{b}_0)\, \mathbf{a}_0 \cdot \mathbf{C}\mathbf{b}_0, \quad I_9(\mathbf{a}_0, \mathbf{b}_0) = (\mathbf{a}_0 \cdot \mathbf{b}_0)^2 \tag{2.28}$$

A well-studied application of this method lies in the medical sciences, where various biologically-reinforced tissues are modelled as anisotropic hyperelastic solids. Holzapfel et. al [34] created an anisotropic hyperelastic model for the human artery (see figure 2.14), where the anatomy is modelled as a thick-walled double-layered cylinder with the fibres arranged in helical patterns. This is especially interesting considering the CRC specimen studied for this project also has a similar filament wound constriction.

Similar to equation (2.26), there is an additive split of the isochoric Helmholtz potential into the isotropic and anisotropic parts as shown in equation (2.29).

$$\bar{\Psi}\left(\overline{\mathbf{C}}, \mathbf{a}, \mathbf{b}\right) = \bar{\Psi}_{\text{iso}}\left(\overline{\mathbf{C}}\right) + \bar{\Psi}_{\text{aniso}}\left(\overline{\mathbf{C}}, \mathbf{a}, \mathbf{b}\right) \tag{2.29}$$

For modelling the matrix, the classical Neo-Hookean model was chosen (see equation (2.14)). while equation (2.30) was chosen for the anisotropic component (fibres). It must be noted that ideally, all the invariants $\overline{I_2} - \overline{I_9}$ should be present in the formulation. However, this creates a large number of material constants which are difficult to calibrate. The two invariants $\overline{I_4}$ and $\overline{I_6}$ capture the stretches in the fibre principal direction and hence were deemed sufficient for this application.

$$\bar{\Psi}_{\text{aniso}}\left(\bar{I}_4, \bar{I}_6\right) = \frac{k_1}{2k_2} \sum_{i=4.6} \left\{ \exp\left[k_2 \left(\bar{I}_i - 1\right)^2\right] - 1 \right\} \tag{2.30}$$

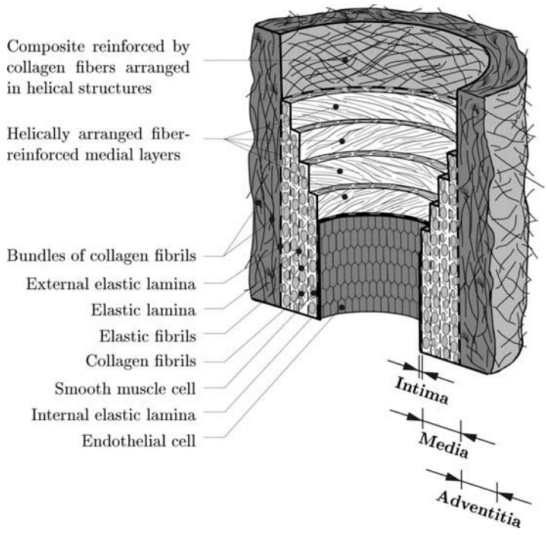

Figure 2.14: Human artery with various biologically stiffened layers [34]

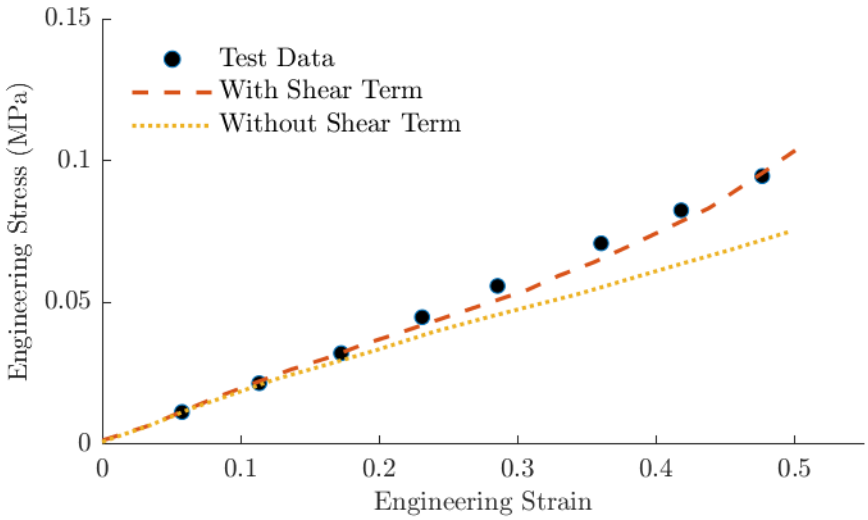

Figure 2.15: Effect of shear interaction term on the deformation of the human annulus fibrosus[37]

Similar models for biological tissues that either extend or modify this described model are presented by Nguyen et. al [35] for tubular organs, and by Zhalmuratova et al. [36] for human and porcupine aorta.

An interesting addition to the above model was made by Peng et. al. [37], [38] by adding an additional shear interaction term to the strain energy potential. This allows the contribution of the fibre-matrix shear energy to be added explicitly to the functional, which leads to a strain energy density functional of the form:

$$\Psi(I_1, I_4) = \underbrace{C_{10}\left(\bar{I}_1 - 3\right) + \frac{1}{D_1}(J-1)^2}_{\Psi_{rub}} + \underbrace{C_2\left(I_4 - 1\right)^2 + C_3\left(I_4 - 1\right)^2}_{\Psi_{fib}} + \underbrace{f\left(I_4\right)\chi^2}_{\Psi_{shear}} \tag{2.31}$$

The advantages of introducing the shear term in the Helmholtz potential are seen in figure 2.15. Here, experimental data is compared against the model with and without the shear term. Both axial and transverse deformations show better matches with the shear term included. It is also postulated by Peng that the fibre rotation angles are better described, but a comparison is made with a solitary

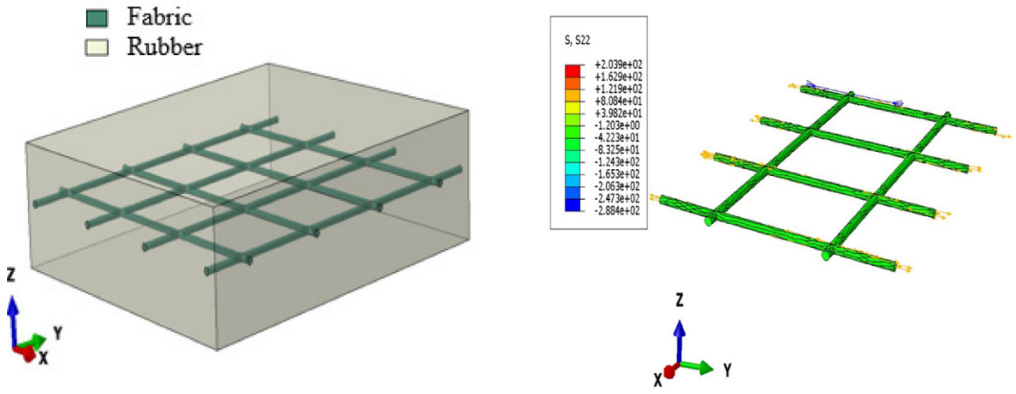

(a) 3D micromechanical RVE **(b)** Stress vector at fiber-rubber interface

Figure 2.16: Micromechanical FEA RVE analysis of fabric rubber composite

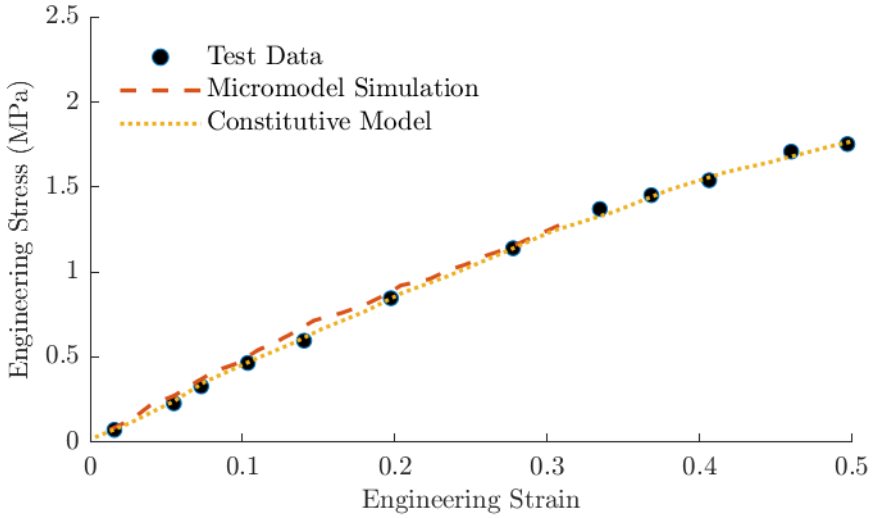

Figure 2.17: Comparison with uniaxial tension results from the micromechanical analysis and the constitutive model by Yang [41]

experimental data point which is not conclusive. Nonetheless, in the scope of this project, such an isolated shear term may be useful to degrade the interface stiffness independently for implementing an interface failure model.

The concept of introducing a shear energy term for the strain energy potential has found application in a number of structures. Aboshio et. al [39] used a decomposition similar to equation (2.31) to arrive at a constitutive formulation for a woven fabric reinforcement in a rubber matrix. One worthwhile addition made in this model was the explicit addition of the fibre volume fraction to the functional description. Xu et. al. [40] further expanded this approach to evaluate the mechanical behaviour of non-orthogonal fabric rubber seals using a 6-variable model.

Yang et. al. [41] used this method to study the behaviour of fabric-reinforced rubber composites. Here, the method of decomposing the strain energy potential into three parts was validated using a 3D micromechanical model (figure 2.16). The results from the RVE model were compared with the constitutive model and a good match was seen (figure 2.17). It was noticed that difference in stiffness between the cord and the rubber causes large shear stresses at the interface. This loads the adhesive bond between the same and may lead to failure once the strength of the adhesive is exceeded. This aspect relating to damage will be explored more in section 5.3.

2.5.2. Explicit Models

Explicit models of CRC analysis are those in which the cords and the rubber constituents are modelled independently and are clearly differentiated in the FEA model. This may be beneficial in terms of modelling damage as the response of each constituent can be studied independently without altering the response of the other constituents. This is not possible when the properties are smeared in a homogenised model.

Donner et. al. [42], [43] created a homogenised material model for multifilament twisted yarns that accounts for inter-filament frictional sliding. This was based on the hypothesis that a bundle of parallel filaments can transmit shear load amongst themselves until their limit of static friction, after which they flow freely and do not transmit load (see figure 2.18).

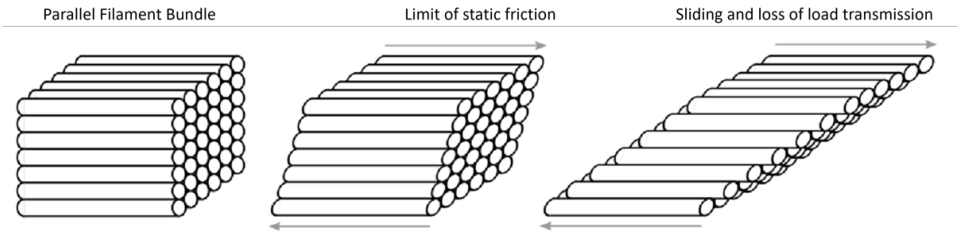

Figure 2.18: Filament bundle frictional sliding [44]

If it is assumed that the filaments in a bundle always stay in contact and transmit stresses only via shear, then it is possible to define a 'friction relevant' stress tensor that preserves only the components which are relevant to frictional force transmission. Filament orientation information is provided to this tensor via tangent vector a at every point along each filament in the bundle (see figure 2.19). The definition of a may also be a design parameter that can define the twist of the yarn.

$$\tau_{\mathbf{eff}} = \tau \cdot \cdot \left(\mathbb{J} - \mathbf{A} \otimes \mathbf{A} - \frac{1}{2}(\mathbf{I} - \mathbf{A}) \otimes (\mathbf{I} - \mathbf{A}) \right) \tag{2.32}$$

Where $\mathbb{J}$ is the 4^{th} order isotropic tensor and $\mathbf{A}$ is the structural tensor defining the filament orientation given by $\mathbf{A} = \mathbf{a} \otimes \mathbf{a}$. Using this definition of stress, the deformation was then solved for using conventional plasticity theory by defining a yield criteria based on the friction coefficient required to initiate slipping, and a corresponding associated flow rule.

This fibre material model was then used to model CRC structures using a unit cell approach. Because the fibre twist was already taken into account in the material model, the fibre may be represented in the unit cell model by just applying the developed material model at the appropriate material point without modelling the fibre as separate geometry. This implementation is seen in figure 2.20.

Further work was done on this model by Weiser et. al [25] to include plastic yielding (apart from

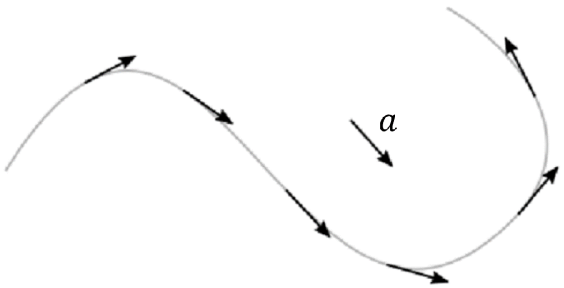

Figure 2.19: Tangent vector a at each filament point [44]

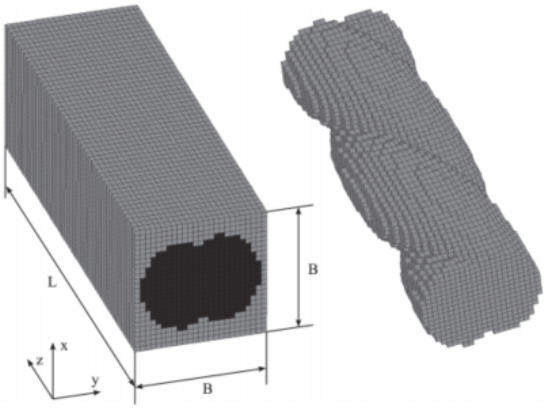

Figure 2.20: CRC unit cell mesh in which twisted fibre geometry is created by assigning material data to discrete material points [45]

frictional sliding) as an additional dissipative mechanism, and by Donner et. al. [45], [46] to model the behaviour of hybrid cords - whose interior construction consists of two or more different materials. Despite the model being impressive in its ability to simplify the representation of twisted cords in a manner that allows FEA implementation, its main drawback is that it relies on data for individual filaments and fibre bundles to be constructed, which is not always easy to obtain.

Moving up one scale, explicit cord-rubber modelling may also be attempted by modelling the cords by truss [47], [48] or rebar elements [49]–[53] embedded in a solid rubber matrix. Here, twisted cords are often treated as isotropic or anisotropic continua, and thus do not need individual filament properties. For the truss method, the cord geometry and placement can be captured very accurately depending on the element mesh size. Rebar elements on the other hand model the reinforcement as a smeared surface layer with effective properties of the entire reinforcement. This topic is discussed in more detail in chapter 6 while building the FEA model for this project. As a synopsis, Oman et. al. [54] recently did a comparative study where a full 3D micromechanical FEA solution was compared against solutions obtained using the truss and rebar approach. They concluded that rebar and truss embedding methods can capture the region of maximum stress, but highly under-predict the magnitude of the stress. This under-prediction can be because of the following reasons:

1. Embedding 1D truss elements or 2D rebar surface elements in the rubber does not account for the volume of the fibres present in the rubber. Thus, depending on the density of fibres present in the rubber, the fibre volume fraction may be grossly under-predicted due to this effect.
2. Studies [55]–[59] have shown that for twisted cords, as the cross-section gets larger, transverse shear stresses become a significant contributor to fibre failure, especially for off-axis loads. As truss and rebar elements cannot capture (out of plane) shear stresses, they are likely to over-predict its strength.
3. Any overlaps or separations in the fibre pattern are ignored when it is modelled either using trusses or rebar. Here, the entire fibre geometry is modelled in a planar manner.

Thus, via this study, it is concluded that to model damage and failure in CRCs, detailed models that capture the undulating geometry and correct cord-volume fractions are essential for capturing its complex stress states.

2.6. Automated Design and Manufacturing at TANIQ

The CRC products used for this project are developed using TANIQ's in-house suite of automated filament wound composite design and production software. The workflow for the complete production

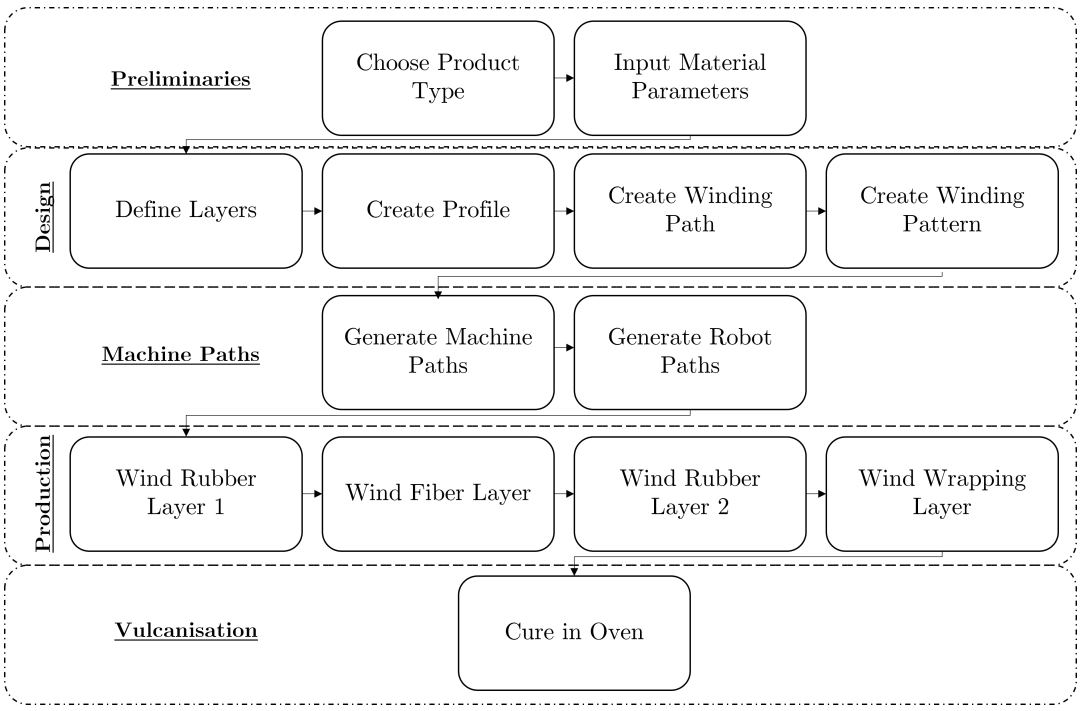

Figure 2.21: Production workflow for CRC products at TANIQ

can be seen in figure 2.21. This workflow can be broadly split into two categories - product design on the TaniqWind platform, and production using the Scorpo-Virgo robotic system.

2.6.1. Product Design using TaniqWind

Profile Generation

Figure 2.22: Layer profile generation

The product design begins with the definition of the desired profile for each winding layer - see figure 2.22. As seen in figure 2.21, for the CRC product chosen, there are two rubber layers and one fibre layer. Thus, three profiles need to be generated, each being offset from the previous layer by the layer thickness. These layer thicknesses can be estimated from the rubber tape dimensions and the production stretch. These parameters are often calculated automatically by the software after accurate material data is fed in.

Path Generation

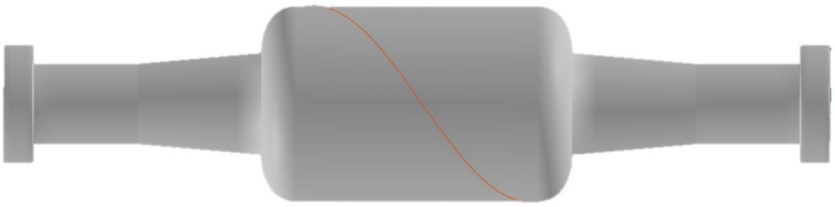

Figure 2.23: Helical path generation

Once a profile for a layer is created, a winding path needs to be created - see figure 2.23. This winding path is a single trajectory between the two extremes of the profile that follows predefined angles over the cylindrical portion over the profile. Paths may be either helical or circumferential. In case a helical path is self-stable and requires no friction to be held in place, it is known as a geodesic. All other paths, including all portions of a geodesic path that traverse over the polar openings, need adequate friction between the layer and the substrate below it to maintain the defined angles.

Winding Pattern Generation

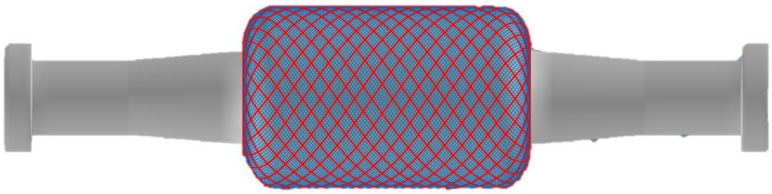

(a) Winding pattern for fiber

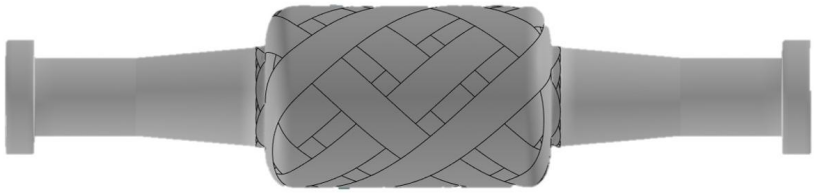

(b) Winding pattern for rubber

Figure 2.24: Helical pattern generation

A winding pattern is created by repeating a single path a fixed number of times to and fro along the circumference of the profile. An important design variable while designing the winding pattern is the dwell, which is the angle subtended by the circular circumferential path travelled by the fibre at the polar opening before turning around and continuing its journey towards the opposite end. Too high a dwell creates an excessive buildup of fibres near the ends of the specimen, which may lead to incomplete penetration by the rubber and subsequent formation of dry spots. On the other hand, having sufficient dwell is necessary to hold the metal flanges (see figure 6.6) in place during pressurisation. A more detailed discussion of fibre patterns is presented in chapter 3.

Generation of Machine Paths

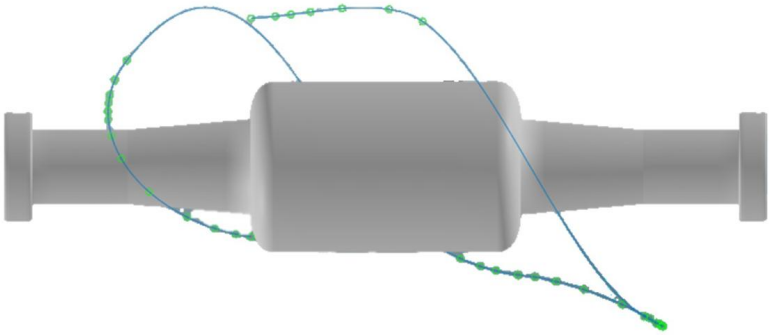

Figure 2.25: Automatic machine path generation by TaniqWind

With the generation of the patterns for all layers, the design of the product is complete. The software then uses the defined parameters to generate appropriate machine paths for all the axis of the robot and the tool head. This entire process is automated with minimal need for user input.

2.6.2. Automated Production using the Scorpo Virgo System

With the design phase complete, the robot program generated by the software is loaded onto the Scorpo Virgo filament winding robot, which is equipped with an ABB six-axis industrial robotic arm - see figure 2.26. The system also contains automatic fibre tensioners, along with the ability to switch between rubber, fibre and wrapping tools automatically. To begin production, the mandrel is cleaned, lubricated with release agent, and placed firmly in the chucks of the external axis. Then, the fibre, rubber and wrapping layers are applied.

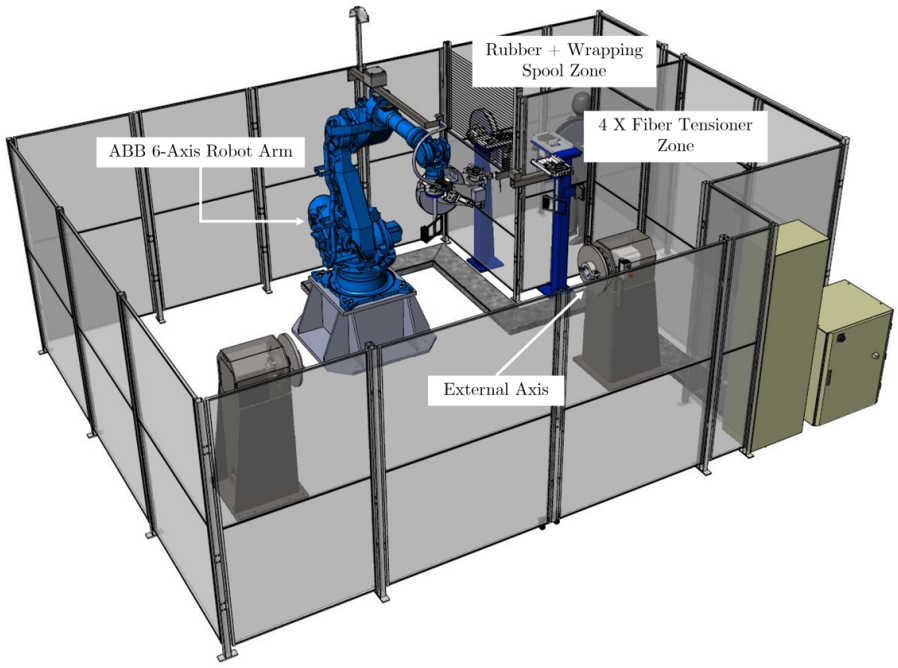

Figure 2.26: Taniq Scorpo Virgo robotic system

Rubber Layer Winding

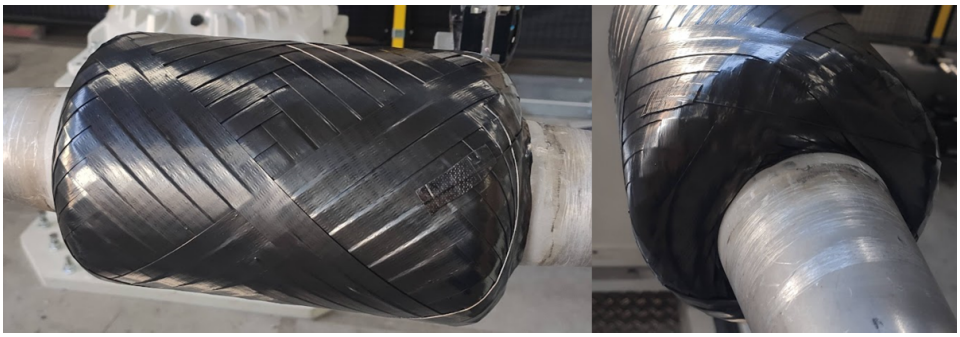

Figure 2.27: Rubber winding layer

There are two rubber layers in the current product design - one on either side of the fibre layer. To obtain an even rubber layer with the desired coverage, care must be taken to ensure that the fibre width fed to the software matches that of the rubber on the production spool. Additionally, the position of the mandrel should be correctly centred on the external axis, with the offset correctly matching that in the software. Failing to do so could lead to biased winding, in which one polar opening has excessive rubber, while the other suffers insufficient coverage.

Fiber Layer Winding

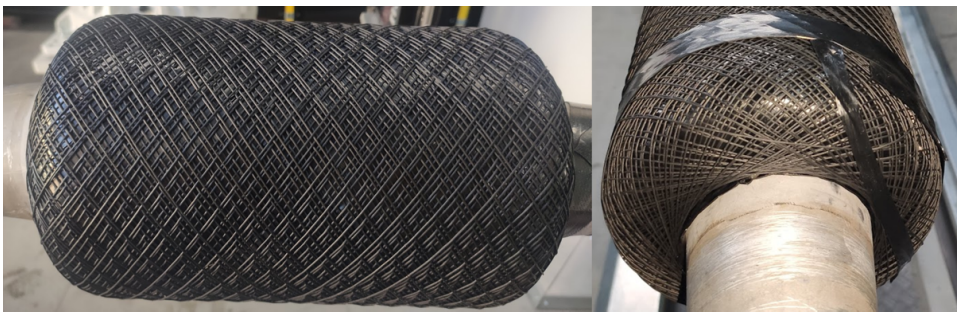

Figure 2.28: Fiber winding layer

The fibre layer is wound using fiber spools mounted on one of four automatic fibre tensioners (figure 2.29) in the robot cell. The main job of the tensioners is to maintain constant tension in the fibres during the winding process irrespective of the position of the robot head. This tension can be varied by the user. Once again, care must be taken to ensure that the position of the mandrel with respect to its entered position in the software is in agreement. Additionally, the slippage of fibres, especially at the polar domes should be monitored. If excessive slip occurs, it indicates that the friction coefficient is not sufficient to sustain the current winding angle, and hence a new winding path must be designed.

Wrapping Layer Winding

Finally, after the winding of the fibre layer and two rubber layers, a nylon wrapping tape under high tension is wound around the specimen. The aim of the wrapping tape is to apply consistent pressure over the sample to aid compaction during the vulcanisation process and to facilitate the flow of rubber into the fibre gaps. The winding tension must be carefully modulated to ensure that there is enough compaction pressure to aid curing, but not high enough to squeeze the rubber out through the product ends (see figure 4.5).

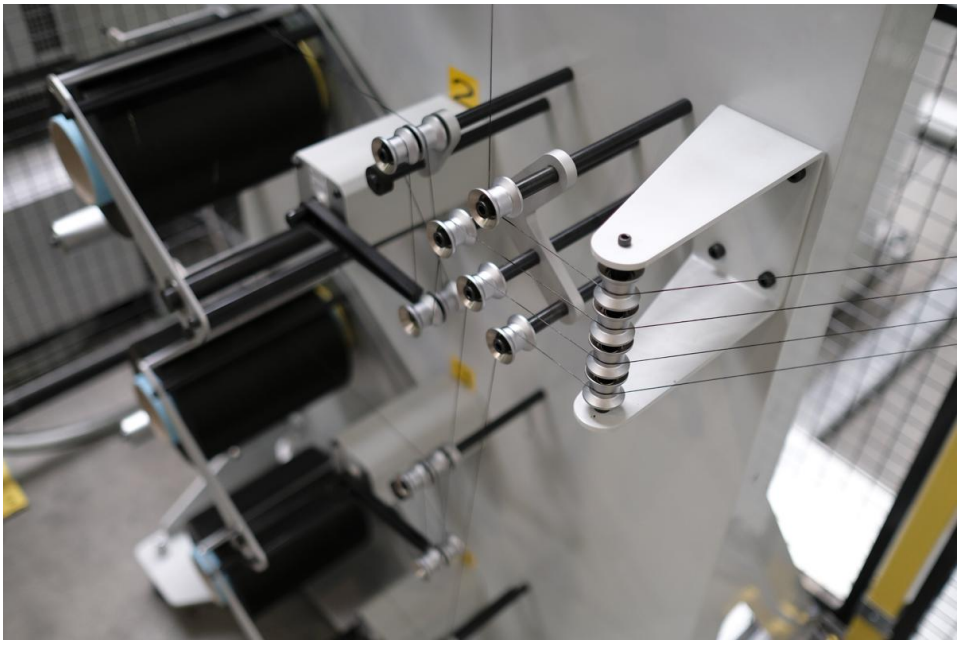

Figure 2.29: Fiber tensioners in the Virgo robot cell

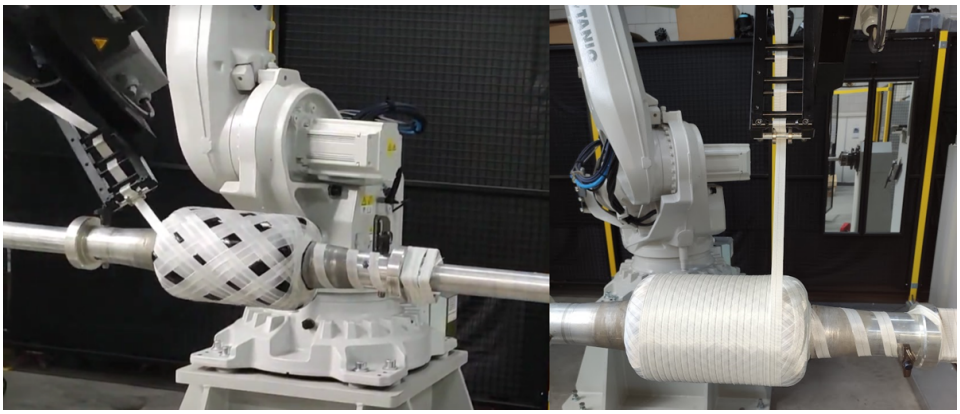

Figure 2.30: Winding of nylon wrapping layer

2.7. Conclusion

In this chapter, a brief overview was given regarding the current state of the art in CRC product modelling and manufacturing. To motivate modelling the non-linearities in CRC structures, first, a short summary was given of 'legacy' attempts to linearise cord-rubber behaviour. Following this, hyperelasticity was introduced as a convenient constitutive framework to describe CRC non-linearities through the material model, and common phenomenological and physically-motivated hyperelastic rubber models were presented with their drawbacks. Finally, homogenised and explicit methods of modelling CRCs were introduced via the presentation of relevant literature. It was concluded that homogenised models do a good job of phenomenologically representing the pre-damage response of CRCs. However, they fail to capture local events which may be key to predicting the onset of damage. Here, explicit CRC models do a better job, where, depending on the scale considered, various damage phenomena can be described by the model.

Being a project primarily focused towards predicting the burst pressures of CRCs produced by Taniq's Scorpo Robotics system, it was considered appropriate to include a concise overview of the design and manufacturing technology developed as a part of this production package. Here, the design workflow to be used on the product development software - TaniqWind is detailed, following which steps taken

to produce the rubber, fibre and wrapping layers via the robotic arm are described.

3

Overlap Geometry Modelling

Modelling of filament wound patterns presents a unique set of challenges which are otherwise not present in a conventional composite layup. This chapter focuses on the intricacies of developing representative geometry to describe filament wound structures, and also motivates the need to model the overlap pattern that results from this manufacturing process.

3.1. Brief Introduction to Filament Winding Patterns

This section will focus on the winding pattern created by winding the fibres in a helical pattern. Although a detailed discussion of the generation of winding patterns and its mathematics is beyond the scope of this project, an elementary qualitative discussion of the same proves useful to better understand the fibre geometry used in this study. As previously explained, the pattern created by the rubber is not focused upon as the pattern itself is lost when the rubber exceeds its glass transition temperature during the vulcanisation process.

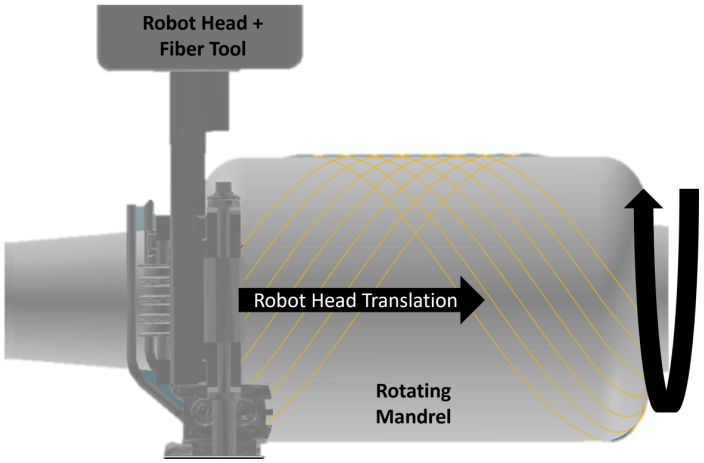

Figure 3.1: Mandrel rotation and robot head translation produce the required (fibre) winding angle

At its core, the fibre pattern is constructed using a continuous fibre yarn that is wrapped along an axisymmetric mandrel in a to-and-fro motion along the axis. The mandrel rotates about its own independent axis, and the relative difference in rotational and linear velocity of the mandrel and the robot head respectively allows for a precise definition of the path winding angle - see figure 3.1.

Once a fibre path is generated as detailed in section 2.6, it is repeated along the mandrel's equatorial

circumference to form a winding pattern that covers the mandrel surface by a predetermined coverage. This pattern may be described by two integral constants - p and q, a decimal value - ϕ, and a boolean s that specifies whether the pattern is leading or lagging. This concept can be further illustrated if we look at a circumferential cross-section along the mandrel's axis. Then, the equatorial diameter may be divided into n equidistant points as shown in figure 3.2. Here, $p = 5$ characterises the number of partitions the circumference is divided into while $q = 2$ specifies that the following path is laid by stepping over 2 partitions each time. This is evident by the partition numbering in figure 3.2. The distinction between leading and lagging patterns is made only when laying the $(p+1)^{th}$ loop, wherein a leading pattern (figure 3.2a) begins to the right of the first points when the layup is clockwise, while a lagging pattern (figure 3.2b) begins to the left. The dwell (ϕ), which is the angular rotation of the fibre along the circumference of the polar opening of the mandrel, is zero in this reference image.

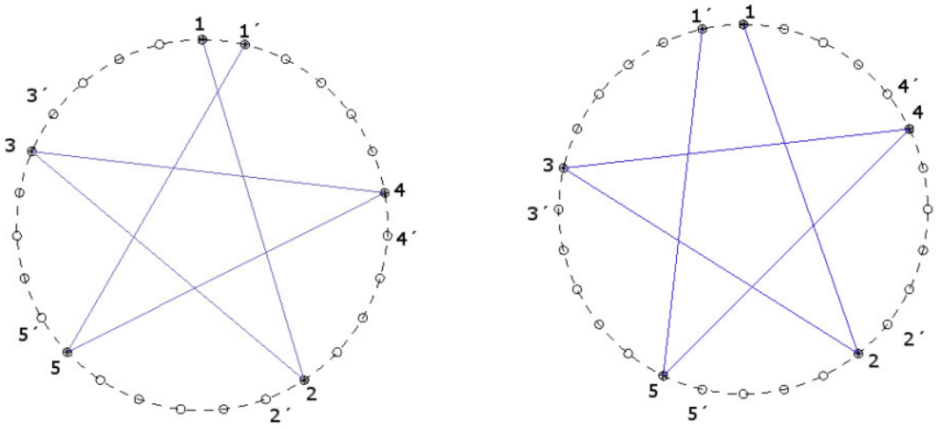

(a) Leading 5/2 pattern **(b)** Lagging 5/2 pattern

Figure 3.2: Variation of the 5/2 winding pattern with $n = 28$ equatorial points [60]

On the cylindrical surface of the mandrel, the formed pattern then consists of a repeating set of rhombi of varying sizes. The fundamental unit consists of the rhombi whose perimeter is made of the first p loops (red lines in figure 3.3), which are then filled internally by the subsequent p loops (blue lines in figure 3.3).

3.2. Effect of fiber overlap patterns

Barring the first half p loop, all subsequent fibres are laid such that they intersect previously laid fibres at least once. The resulting geometry is a complex undulation - and is a function of the helical winding angles, the fibre-to-fibre friction coefficient, the mandrel geometry, the fibre winding tension, etc. An exaggerated example of the same is shown in figure 3.4, where the build-up occurring in one rhombus (defined at the borders by the white lines) is tracked as it grows. It is noticed here that the complex interactions of each fibre with its neighbours cause fibre bending, shifting and radial thickness buildup. Such designs with excessive fibre buildup are to be avoided as they may result in considerable deviation from intended patterns due to lower friction coefficients between fibres, smaller contact patches and the fact that the robot program is not correcting its winding path for the radial thickness buildup.

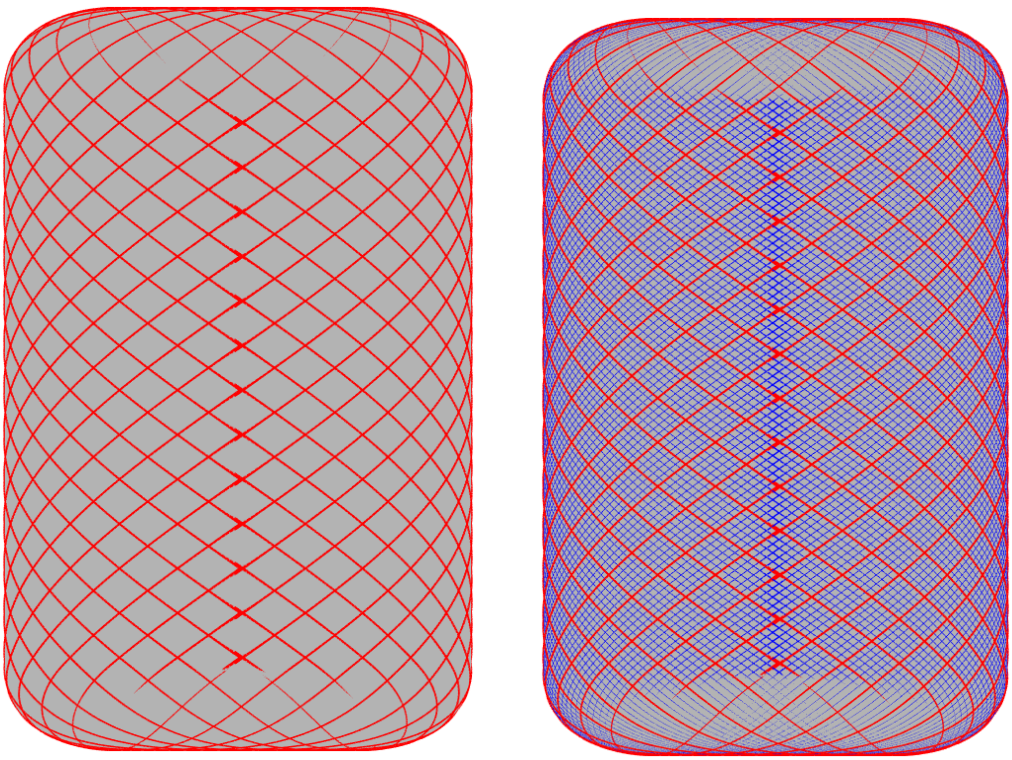

(a) Pattern after first p loops **(b)** Full winding pattern

Figure 3.3: 23/22 Lead Winding Pattern

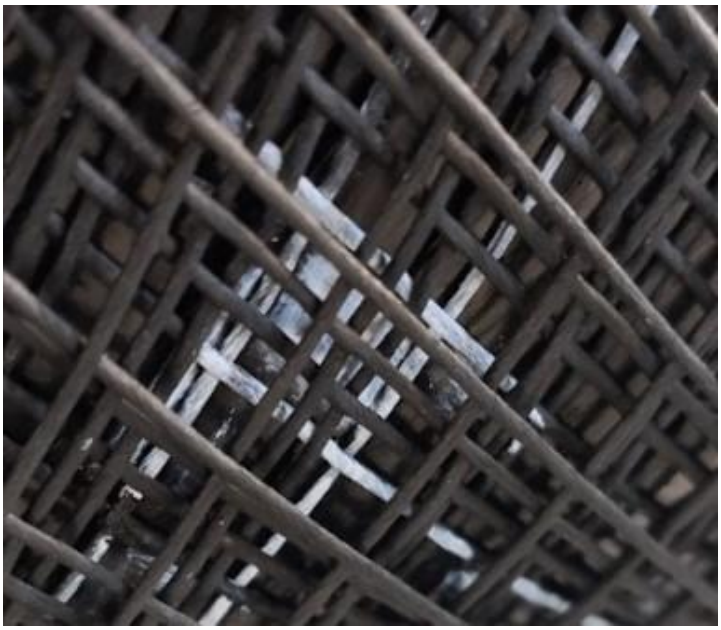

Figure 3.4: Fiber build-up during fibre winding. The white markers define the boundaries of a rhombus formed by the first p loops

Much of the literature available regarding the effects of these undulations is present for tape-laid polymer composite materials. Nonetheless, the similarity in the manufacturing process warrants careful attention to these results. These undulations are often considered by studies [61], [62] as a special kind of defect which influences the structure's load path by changing the fibre's orientation. Rousseau et. al. [63]

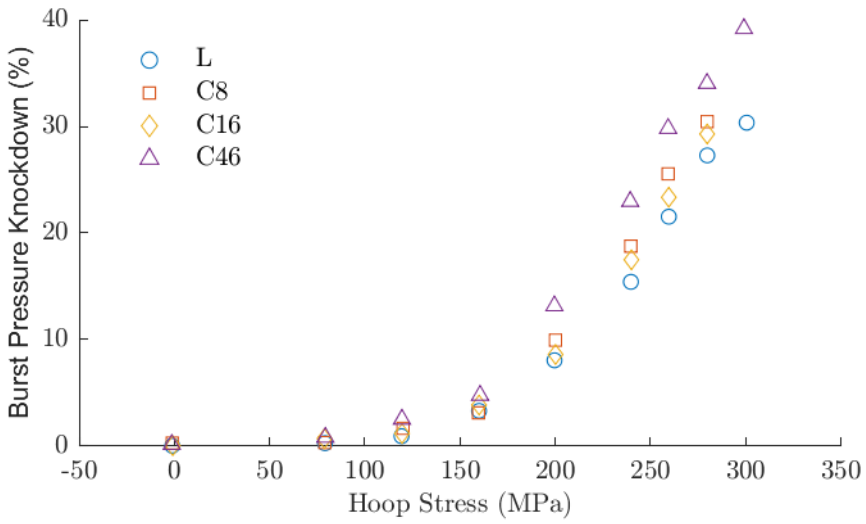

Figure 3.5: Variation of damage with increasing fiber undulation for close-ended pressure vessels [63]

studied these effects of undulations experimentally for close-ended pressure vessels by comparing the damage levels in three samples C_i of varying levels of undulation i=8, 16, 46% with a control flat specimen L. Here, the damage was represented by a scalar parameter representing a loss in axial stiffness while the levels of undulations were characterised by the ratio of the undulated area in a periodic rhombus to the area enclosed by the rhombus.

As seen in figure 3.5, the difference in damage between the undulated specimens and the flat control increases rapidly at higher pressures, with greater damage observed for a higher degree of undulation. This forms a strong argument to explore the effects of fibre undulation for this project. This argument will further be strengthened in chapter 7, where the developed model with undulations is compared to the model without considering overlap.

3.3. Modelling fiber overlap patterns

Developing an exact solution for fibre undulation is a complex task that needs to take into account several variables and phenomena which were discussed earlier. Such a level of accuracy would demand a study of its own and is outside the scope of this project. Despite this, it is still necessary to develop the overlap geometry in a way that captures its main essence without extensive experimental campaigns.

It is once again possible to turn to tape-laid polymer composite pressure vessels for inspiration. Several studies [62], [64]–[66] employ simple trigonometric or linear functions to describe the undulation geometry as seen in figure 3.6. However, on comparing these simplified descriptions to the geometry seen in figure 3.4, a considerable deviation is seen in the fibre placement. These can be attributed to the following reasons:

- CFRP tapes are inherently wider than the diameter of the cords in question and thus do not interact as closely as single fibres to their surrounding neighbours.
- Pre-preg CFRP tapes, as used in these studies, tend to be 'tackier' compared to the cords used in this project. This means that under the influence of compacting pressure, they are better able to adhere to the layers under them, thus forming undulations with tighter radii (similar to figure 3.6b).
- The studies using CFRP tapes have a much higher coverage ($\approx$ 200%) compared to the fibre coverage used in this project($\approx$ 50%). This means that the rhomboidal regions can be considered sufficiently small to ignore the mandrel curvature in CFRP structures but not in CRC structures

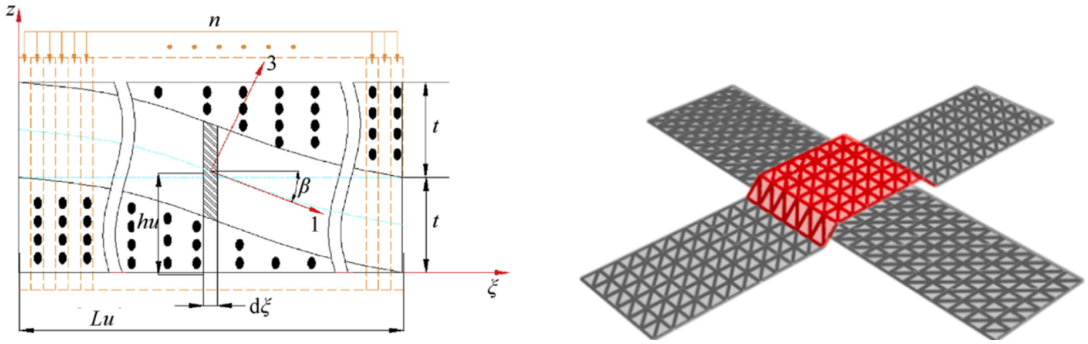

(a) Sinusoidal overlap model [64]

(b) Linear overlap model [66]

Figure 3.6: Simplified overlap models

(see figure 3.7).

Even if separate mathematical descriptions were to be made specifically for filament wound structures, they would need extensive experimental calibrations (or assumptions) that would differ from design to design. A more robust solution is desired that accounts for the mandrel curvature, and is automatable using data only from the filament winding geometry and production parameters. This can be achieved via a detailed simulation of the winding process using non-linear FEA, or by the means of a (semi) analytical approach. The latter has the following benefits over the FEA approach:

- The fibre pattern seen in figure 3.4 represents the final rhomboidal geometry achieved after fibre stretching and compaction during the winding process. Any FEA solution aiming to predict this geometry would need an initial geometry that is strain-free and would have to reach this final stage via careful application of loads and boundary conditions. This could very easily balloon into a detailed manufacturing simulation, which is not the goal of this project.
- A lot of data during the winding process is not easy to capture. This includes the varying fibre tension throughout the winding process, the friction coefficients between the fibre-fibre and fibre-rubber interfaces, and the fibre expansion and relaxation during rubber vulcanisation. This implies that any developed FEA model would have to be based on assumptions which may not necessarily yield accurate geometry.

As an alternative to a full production simulation, a simple geometrical solution can be obtained based on convex hull algorithms. This is the point of discussion in the following section.

3.4. Convex hull model for fiber overlap

A novel model for fibre overlap may be devised based on the observation that a fibre under pure tension will traverse the shortest path between any two points on which its ends lie. This same concept may be extended to the case of fibre overlaps by making the following assumptions:

- The fibres are in a state of pure tension always.
- The fibres are infinitely rigid against cross-sectional deformation. In other words, the cross-section remains constant irrespective of the applied load.
- There is no fibre slippage. Frictional forces are adequate to maintain the required helical winding angles.
- There is no effect of neighbouring fibres on the fibre placement within a single domain. This domain can be as large as possible to increase accuracy within the domain and to account for as many boundary effects as possible. For this study, a domain is defined as any rhombus bounded by first p fibres (see figure 3.3).

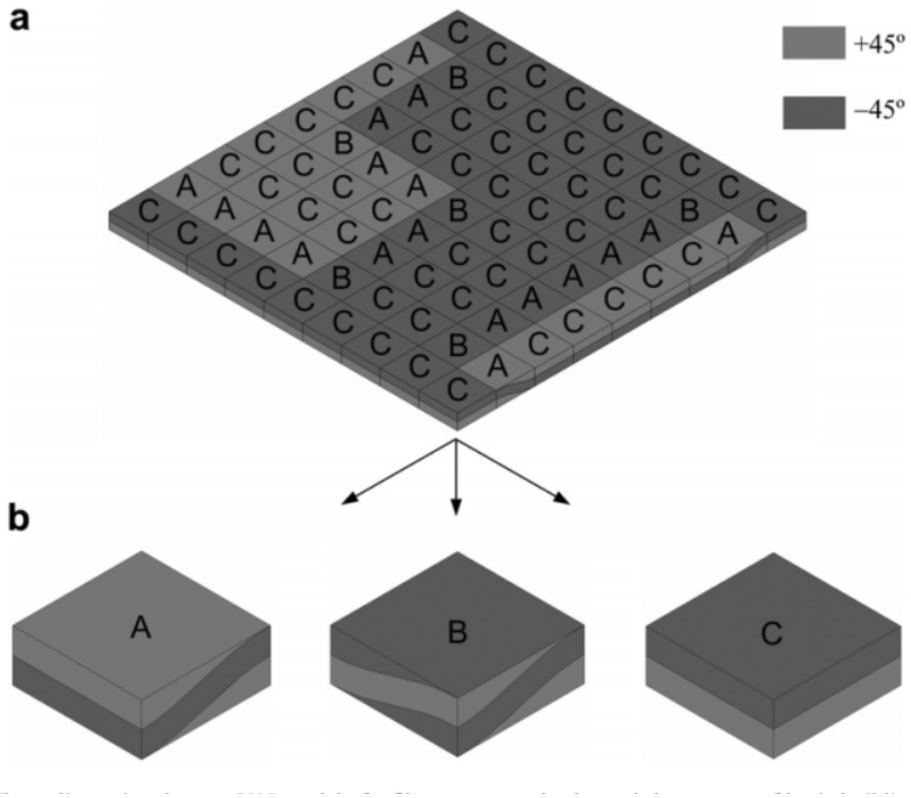

Figure 3.7: Flattened RVE model for undulating structures [67]

Then, it can be theorized that when a fibre is laid on top of pre-existing fibres, the newly laid fibre will follow the shortest constrained path between the fibres at the domain boundary that does not intersect either the mandrel or any previously laid fibres. The constraint here refers to the ideal helical winding path that the overlapping fibre would have followed if there was no overlap. This concept is illustrated in 2D in figure 3.8a. Here, the shortest path for a crossover fibre between fibres F1 and F2 would be one which partially bridges and then partially follows the profile of the mandrel. The reference straight line path, which is the mathematically shortest path, may not be used as it intersects the mandrel. However, the same fibre is then able to follow the shortest straight line path between fibres F2 and F3 as that path does not intersect the mandrel.

An elegant approach to automate the generation of crossover paths is the use of the convex hull algorithm. The convex hull $CH(Q)$ of a set of 2D planar points Q is defined as the convex polygon of the shortest perimeter which either contains or encloses all the points in Q [68]. Then, the set Q can be defined such that it contains a discretised set of all possible points the fibre can take. This includes circumferential points on both the mandrel and any other fibres previously laid down. $CH(Q)$ thus represents the shortest perimeter path the overlapping fibre takes over the mandrel and all previously laid fibres. All the points in $CH(Q)$ are then connected via straight lines to form the overlapping fibre paths. This implementation can be seen in 2D in figure 3.8b. Due to the relative efficiency of the method, a large number of points can be included in Q to avoid significant discretisation errors.

The discussion until now was focused on understanding the fibre overlap geometry in 2D. In 3D, fibres do not traverse axial and hoop paths as shown in figure 3.8 but complex undulating helical paths. Despite this, it is possible to collapse the problem into two dimensions by noting that fibres traversing a helical path on a cylinder will follow a circumferential path along the cross-section when projected on the $r - \theta$ cross-sectional plane - similar to figure 3.8. In this cross-sectional plane, the convex hull algorithm can be employed, and the resulting geometry can be pushed back into 3D space by adding the z-dimensions. This process is highlighted in figure 3.9 as a flowchart. The same process was then scripted within a MATLAB® script for further use.

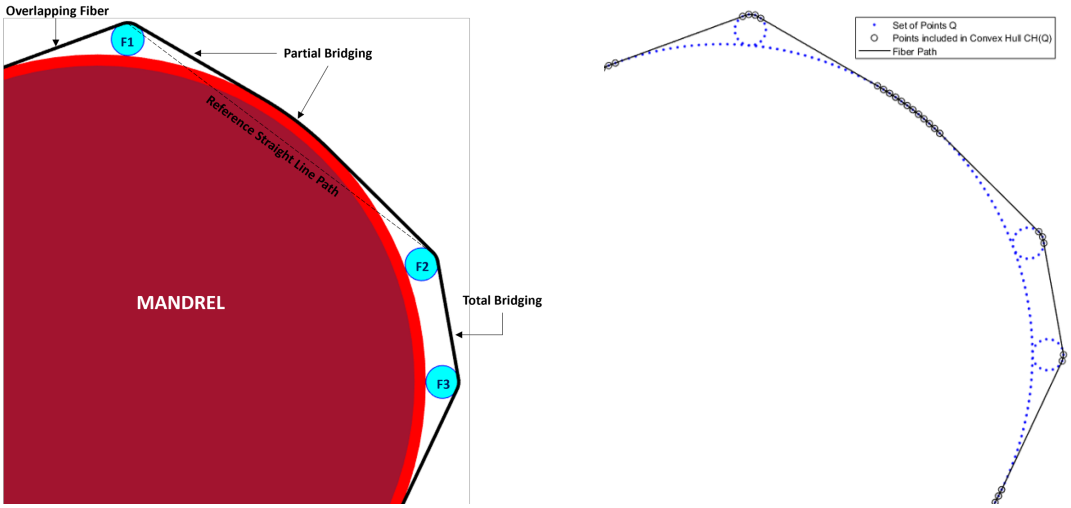

(a) 2D illustration of bridging behaviour **(b)** Convex hull algorithm for fiber overlap

Figure 3.8: Proposed fibre overlap model in 2D (only for explanation, not drawn to scale)

3.5. Limitations of Model

Building a simplified geometrical overlap model will always entail limitations and losses of accuracy. These limitations are the subject of discussion in the current section.

3.5.1. Compaction Forces

The most significant omission in the current convex hull implementation is the downward compaction force due to fibre tension. As seen in figure 3.10, any fibre laid over pre-existing fibres over a curved mandrel will exert a downward compaction force due to its winding tension. This means that fibre F2 in inset L2, figure 3.9 will not be as shown, but will instead be bent toward the mandrel due to the compacting force from fibre F3. This downward compaction would depend on the winding tension, the flexural modulus of the fibre, and the unique boundary conditions present at each the ends of each fibre bridge. These boundary conditions further depend on the frictional conditions present at each contact region. An approach to overcome this issue, although not implemented in this project, is presented in section 9.2.

As a natural extension to the above point, not modelling the compaction forces means that the developed geometry will have a higher radial thickness buildup compared to the actual product. Additionally, not including the tension in the model also ignores the state of pre-stress in the model and thus may contribute to the non-conservativeness in the burst pressure prediction. The same can be said about the stress concentrations induced due to the fibre bending, which may again add a degree of non-conservativeness.

3.5.2. Universal applicability

The developed model is also not universally applicable to all CRC designs. The projection of the 3D geometry onto a cross-sectional plane as shown in figure 3.8 to allow the computation of a 2D convex hull is only possible if the product geometry is cylindrical in the domain of interest. Any other shape would not allow projection onto this plane via simple removal of the z coordinate. However, this is not a hindrance in the current project due to the chosen shape of the pressure vessel. Additionally, it is assumed the fibres within one domain, do not interact with fibres outside its domain. In this context, it means that the fibres within one rhombus do not affect the overlapping placement of fibres in another rhombus. This effect can be considered relatively small compared to the other effects presented, as the

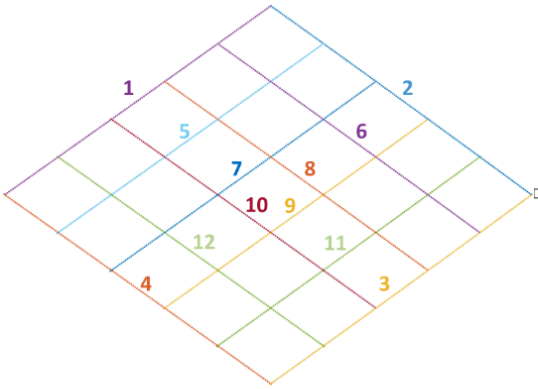

Inset L1: Set of discrete points for each fiber

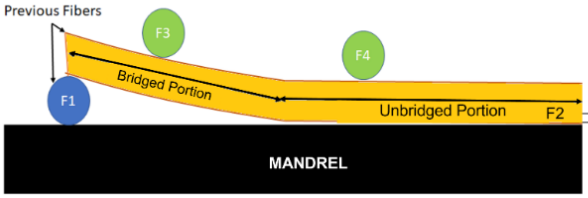

Inset L2: Algorithm for placing overlapped fibers

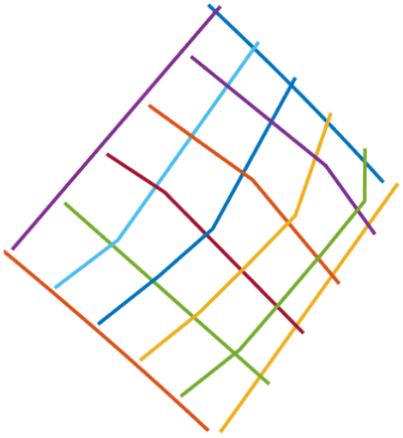

Inset L3: Fiber Paths generated by Overlap Code

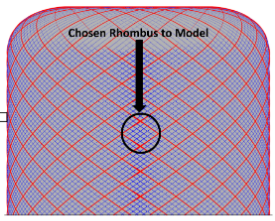

Inset R1: Choice of Rhombus

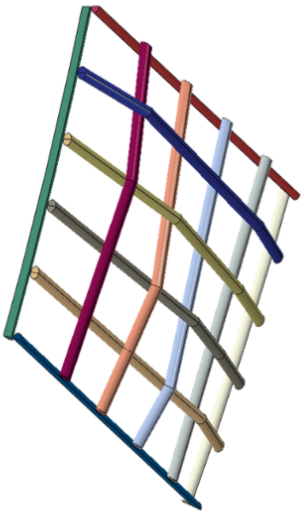

Inset R2: Swept 3d Fiber Paths

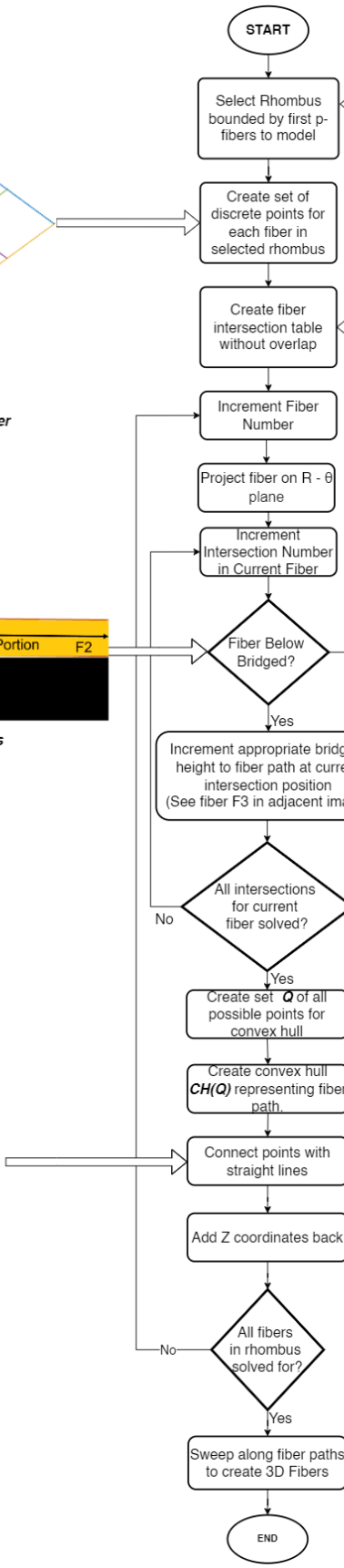

Current Fiber	Intersects With
1	-
2	1
3	2
4	1,3
5	2,4
6	1,3,5
7	2,4,6
8	1,3,5,7
9	2,4,6,8
10	1,3,5,7,9
11	2,4,6,8,10
12	1,3,5,7,9,11

Figure 3.9: 3D Convex Hull Algorithm

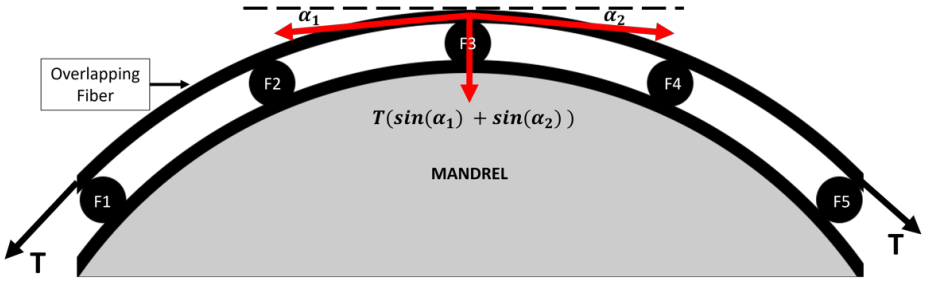

Figure 3.10: Fiber compaction due to winding tension (only for explanation, not drawn to scale)

choice of domain, which is defined as a rhombus enclosed by first p fibres, allows for a representatively large number of fibres within a single domain.

3.5.3. Behavioural Simplifications

Fibres in the proposed model are assumed to be perfectly rigid against transverse deformation. However, as seen in figure 3.11, fibres do tend to undergo (considerable) flattening when crossing over another fibre. Additionally, the model assumes perfect 'stick' conditions between fibres at all times and ignores any effects that induce fibre slippage due to insufficient friction.

Figure 3.11: Fiber bending and cross sectional deformation during winding

3.6. Conclusion

The aim of the current method was to generate a simple yet representative overlap geometry model for cylindrical filament wound CRC structures for further use in FEA models. The need for modelling overlap patterns explicitly instead of relying on empirical mathematical simplifications was highlighted in section 3.2 and section 3.3. Then, through the use of the 2D convex hull algorithm as described in section 3.4, a geometric solution was arrived at for the overlap pattern specifically for fibres laid on a cylindrical mandrel within a user-defined rhomboidal domain. Finally, the limitations of the current model were acknowledged in section 3.5, where the main drawback was identified as the omission of the downward compaction force due to winding tension.

This page was intentionally left blank.

4

Analysis Methodology

Once the overlap geometry has been generated based on the method detailed in chapter 3, the FEA model can be developed. This chapter elaborates on the submodelling approach used for this project and the development of the global and local models used thereof.

4.1. Global - local analysis

The inclusion of fibre overlap in the model warrants the creation of separate rubber and fibre geometry that is later assembled in the FEA model. However, modelling each overlap for each fibre over the entire product domain is a highly computationally expensive effort - one that may not be beneficial in the design stages of the product, where rapid analysis is required to try several prospective options. An elegant approach to overcome this setback is the usage of a global-local model. In such an approach, the global structure is studied using a low-fidelity model, with only the critical regions of interest being modelled with a high-fidelity local model [69]. There is usually at least a one-way transfer of data from the global to the local model, but high-accuracy analyses also attempt to include a feedback loop to correct the global model behaviour based on the local model response

Using such a bifurcated global-local approach is a common method to analyse damage mechanisms in CFRP composite structures. This allows relevant meso and micro-scale effects to be captured by the simulation without modelling the entire domain with the fidelity of the finest detail. The conventional approach to this is to first study the high-fidelity model of the desired scale under suitable boundary conditions, and then to homogenise the structural behaviour at this length scale into a material model and apply it homogeneously at the macro length scale. Visrolia and Meo [70] studied the failure behaviour of 3D weave composites using a micro-scale RUC model. The model behaviour was then homogenised using asymptotic homogenisation, following which a continuum damage model was employed at the macro scale. Similar approaches were used by Pulangan et. al [71] to study the damage behaviour in GFRP panels, by Zhou et. al. [72] to study damage behaviour in CFRP woven composites, and most interestingly by Zhang et. al. [67] and Yin et. al. [64] for studying damage in undulating filament wound composite structures.

4.2. Periodicity and RVEs

In most of the studies quoted above, the terms ‘RVE’ and ‘RUC’ are used interchangeably. For the context of this research, a distinction should be made between a repeating unit cell (RUC) and a representative volume element (RVE). A repeating unit cell is defined as the smallest structural unit that can be repeated along all axes to form the complete geometry. Analysis of RUCs is usually done with

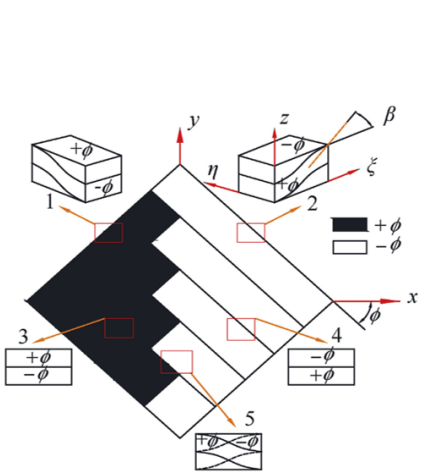

(a) RUC for filament wound structures

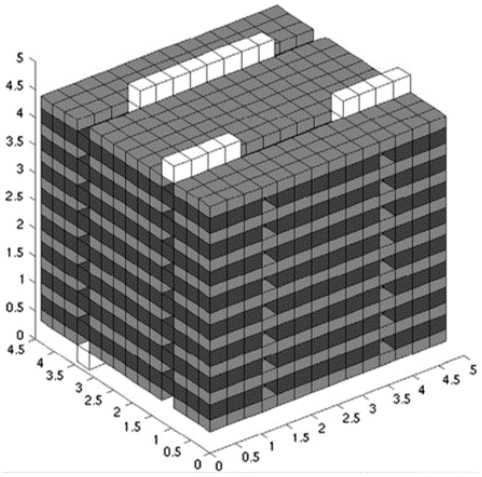

(b) RUC for 3D weave structures

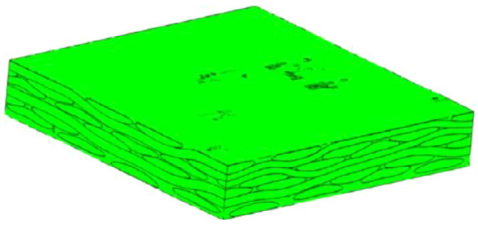

(c) RUC for woven structures

Figure 4.1: Unit cell local models for various applications [70]–[72]

the help of periodic boundary conditions, which stipulate that corresponding nodes on opposite faces of an element should deform identically under an applied load [73] - see figure 4.2. These allow repeating unit cells (RUCs) to be studied independently while allowing the constraint of material continuity to be applied via relevant displacement boundary conditions. On the other hand, a representative volume element is the smallest volume in a structure with several constituent materials that can be considered to be statistically homogeneous such that the RVE response is characterised by the average response of all the constituents. In this manner, the RVE is considered representative of the entire structure. To be representative, it should be small enough such that the variation of the macroscopic fields it represents are sufficiently small, but yet should be large enough to be considered statistically homogeneous [74].

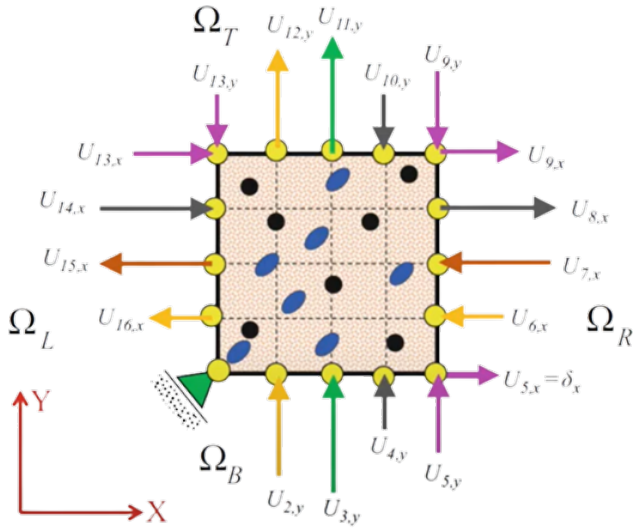

Figure 4.2: Application of periodic boundary conditions to an RUC [73]

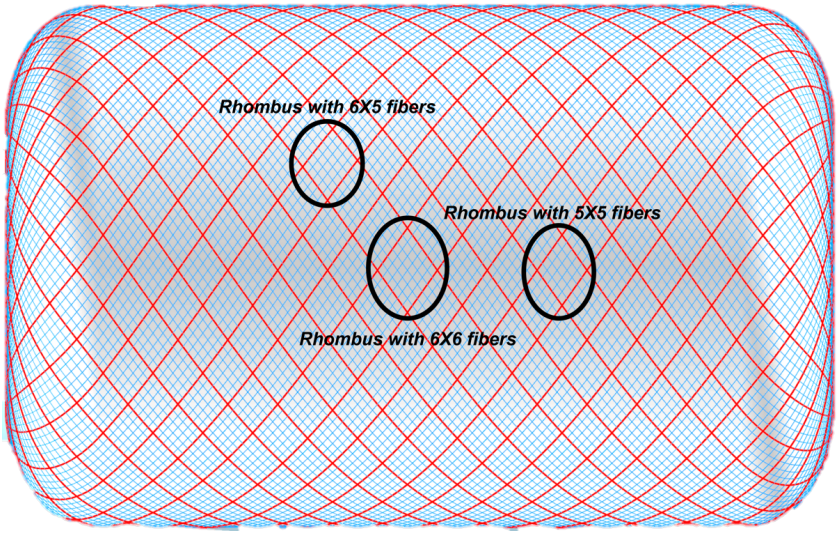

Figure 4.3: Three distinct rhombi developed during fibre winding

A rhomboidal unit cell as a result of the filament winding process can never be considered a pure RUC for the following reasons:

- Any filament winding pattern produced by TANIQ's winding platform will always have three distinct rhombus shapes. This can be seen by returning to the discussion on the parameters p and q for describing the winding pattern. In figure 3.2, it can be seen that successive partitions of the equatorial plane may not have the same subtended angle. This leads to the variation in rhombi sizes as is seen in figure 4.3. Any attempt to find a truly repeating unit by combining several rhombi would either not be possible, or would lead to an RUC that is too big to benefit from the efficiency gains of the global-local approach.
- The overlap pattern itself does not follow a periodic pattern as neighbouring rhombi can have completely different overlap patterns to a given rhombus. This means that no single 3D rhombus can be repeated along the axes to tile the mandrel surface while maintaining fibre continuity.

Instead, each rhombus can be considered as an RVE - with the assumption that each RVE contains features that represent the heterogeneity in the entire product domain. Following this line of thought, the logical pick amongst the three available rhombi to model as the RVE would be the one that is present most frequently in the pattern. Finding out the most common rhombus can be achieved via a simple arithmetic procedure:

- Divide the number of fiber loops n by the p number. The value m then represents the average number of fibres along one side of the rhombus.
- The remainder can be used as an indicator of the distribution of the 3 rhombi. The closer the remainder is to 1, the larger the number of $(m+1) \times (m+1)$ rhombi there will be. Similarly, the closer the remainder is to 0, the larger the number of $(m) \times (m)$ rhombi there will be.

For the chosen geometry (explained in section 4.4) , $p = 23$ and $n = 116$. It must be noted that only half of each boundary fibre (red fibres in figure 4.3) contributes to the fibre count in a given rhombus as the other half is considered a part of the neighbouring rhombus. Then, $m = 5\frac{1}{23}$. Thus, this shows that a very small portion of the rhombi will be larger than 5×5, and hence the 5×5 rhombus would be a reasonable choice for the RVE.

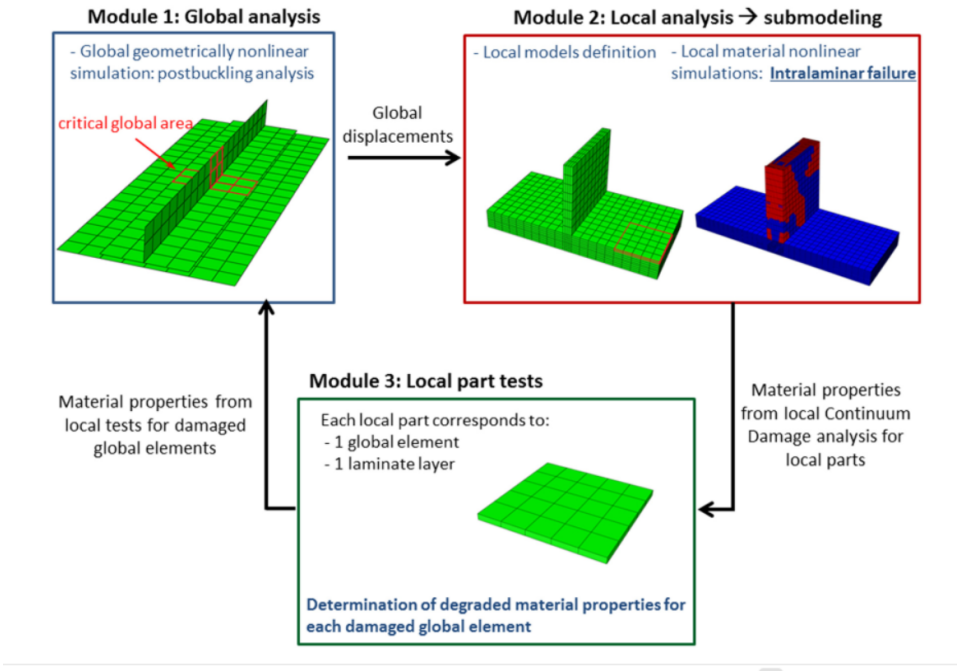

Figure 4.4: Damage analysis of a stiffened composite panel using a two-way submodelling approach [75]

4.3. The submodelling approach

With the adoption of an RVE instead of an RUC, it is no longer possible to use a global-local approach with homogenisation as used by the studies cited in section 4.1. However, a different style of global-local modelling - *submodelling* can be used for the analysis of the CRC structure. In such a study, a course global model is run first to obtain a displacement solution for the entire geometry. These displacements are then applied as boundary conditions on a detailed local 'submodel' in which all relevant effects for the study are modelled to a higher fidelity. In such a modelling procedure, it is sufficient to achieve convergence of only the displacement field (as opposed to the full stress field) in the global model as the displacements are the only relevant quantities transferred to the local model. This reduces the computational complexity of the model several-fold due to the relatively few elements needed to obtain an acceptable solution from the global model.

Although not extremely common, submodelling has been used in literature to analyse composite structural failure. Bogdanovich and Kizhakkethara [76] used the method as early as 1998 to analyse the stresses in a double-lap composite adhesively-bonded joint. Hühne et. al [75] used a two-way shell-to-solid submodelling approach (see figure 4.4) to study buckling and delamination in stiffened composite panels. The same study was extended by Akterskaia et. al. [77]–[79] to include effects of progressive skin-stiffener debonding behaviour using cohesive damage. The positive nature of their results suggests that using a global-local submodelling approach is a promising method to analyse the burst pressure of the CRC pressure vessel - with the local model compromising of single rhomboidal RVE and the global model consisting of the entire product geometry. Details regarding this procedure are further shared in chapter 6.

4.4. Prototype Design

With the methodology for the analysis decided, a relevant design can be created which will be analysed. This includes the choice of the mandrel, the filament winding parameters, and the rubber layer thicknesses. To be consistent with the design method, the main requirement is that the mandrel should have a relatively large cylindrical region such that the performance of the cylindrical region can be assumed

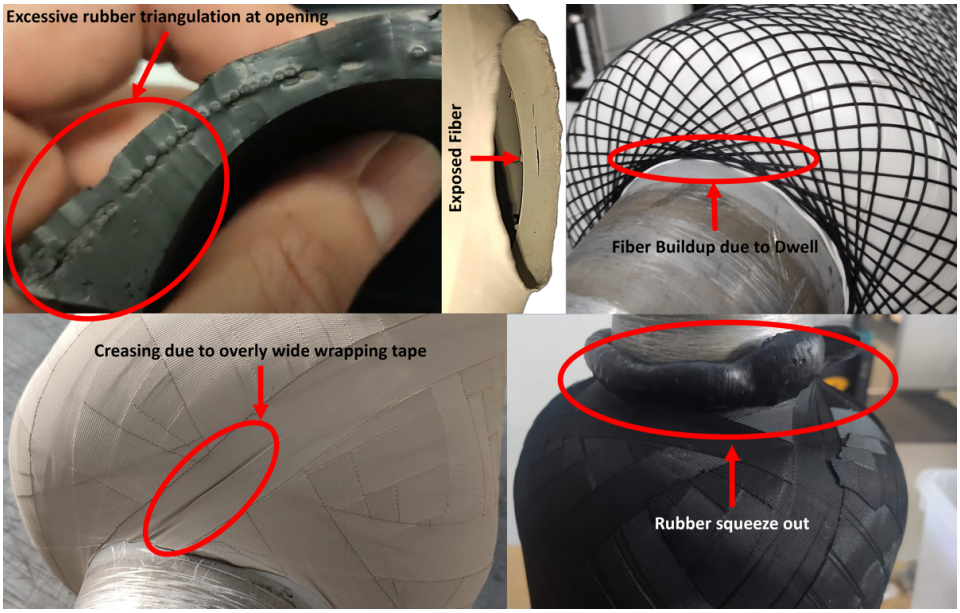

Figure 4.5: Common production defects

to not be affected by the dome ends. This is because the rhomboidal RVE considered for the local submodel only represents the cylindrical face of the pressure vessel and thus is not a representative volume for other regions. Other requirements to avoid common production defects (see: figure 4.5) include:

- Rubber thickness should be sufficient to not allow fibres to be exposed on the external surfaces.
- Rubber triangulation at the polar openings should be minimised. This allows for better flange seating.
- The dwell at the polar openings should be minimised as far as possible. This is because excessive dwell can cause large fibre buildup at the polar opening, causing poor rubber penetration and possible matrix-free regions. At the same time, there should be sufficient dwell to allow enough fibres at the polar opening to hold the flanges in place under pressure loads.
- Wrapping tape width should be low enough to follow the contours of the product without leaving fold and crease marks.
- Wrapping tension should be adjusted to allow efficient rubber vulcanisation without causing the rubber to squeeze out from the polar openings.
- The fibre pattern should not have excessive fibre radial buildup as seen in figure 3.4. The reasons for this have already been elaborated on in section 3.2.
- Fiber coverage should be sufficient to allow for predictable burst performance without burst pressures being excessively high, which may compromise safety.

Taniq had available two possible mandrels that could be used for the project - see figure 4.6. Despite the longer mandrel suiting the analysis method better due to its larger cylindrical section, it was not feasible for use as it needed a bigger oven to vulcanise the product, which was not readily available. As a compromise, the smaller mandrel was used with a geodesic winding angle, which aligns fibres over the cylindrical section along the 'optimal' winding angle as per netting analysis [80]. Here, for an initial estimate, it is assumed that the product is geometrically linear and that the fibres carry all the load only in their axial direction. Then, the balance of forces for a single fibre with winding angle α can be written as:

$$\sigma_{11} t \begin{bmatrix} \cos^2\alpha & \sin^2\alpha & \cos\alpha\sin\alpha \end{bmatrix}^{\mathrm{T}} = \begin{bmatrix} N_{11} & N_{22} & N_{12} \end{bmatrix}^{\mathrm{T}} \tag{4.1}$$

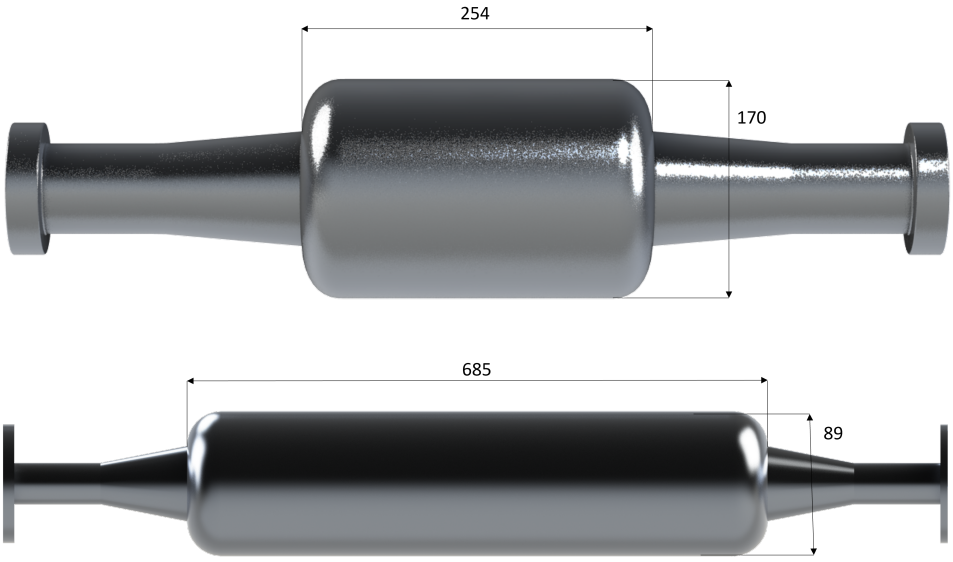

Figure 4.6: Mandrel choices

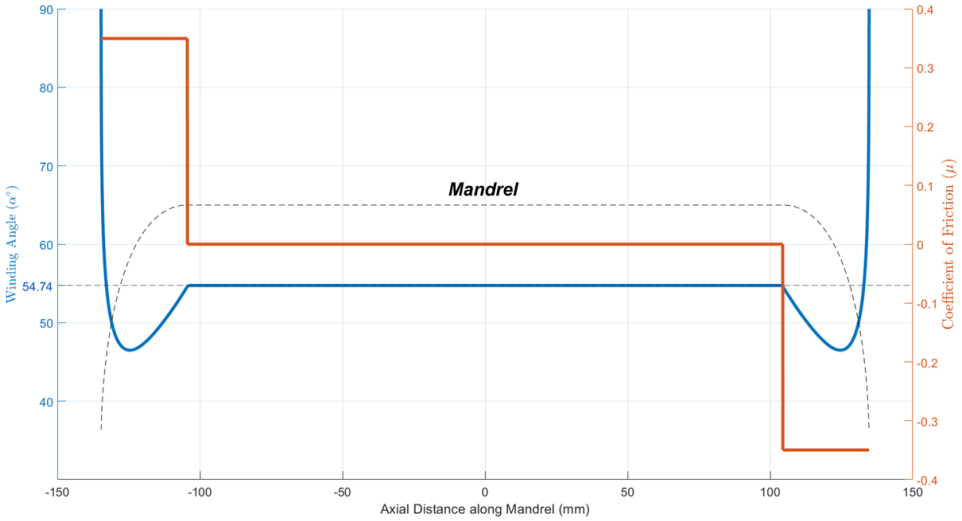

Figure 4.7: Fiber winding pattern friction coefficient distribution and winding angles

where t is the cylinder thickness and N_{ij} are the external loads. Then, by assuming the product as a classical thin-walled pressure vessel, the load vector may be represented for a given pressure p and cylinder radius R as:

$$\begin{bmatrix} N_{11} & N_{22} & N_{12} \end{bmatrix}^{\mathrm{T}} = \frac{pR}{2} \begin{bmatrix} 1 & 2 & 0 \end{bmatrix}^{\mathrm{T}} \tag{4.2}$$

Solving the above system of equations yields a singular solution for α as $\alpha \approx 54.74$. This angle is considered as a first estimate solution for the optimal winding angle and thus ensures that the cylindrical region undergoes minimal fibre rotation on loading. This allows for the region of interest on the smaller mandrel to be considered a uniformly loaded region despite its short length. A winding path with this angle is known as a geodesic path, which is the shortest path between two points on the mandrel surface. This characteristic also means that the path is usually stable and non-slip [81].

The created fibre winding pattern is the same as shown in figure 4.3. For the pattern, the winding angles and required friction coefficients are seen in figure 4.7. The fact that no friction is needed to

wind the fibre over the cylindrical section is a feature of the geodesic winding angle $\alpha = 54.74$. On the dome section, the required friction increases steeply, reaching its maximum at the polar opening, where the inclination of the mandrel profile approaches 90.

4.5. Conclusion

The current chapter focuses on motivating the choice of global-local submodelling as the methodology for the FEA analysis of the CRC pressure vessel. Global-local analysis was first introduced as a viable option considering the computational cost of modelling the entire domain in high fidelity. The distinction between repeating unit cells and representative volume elements was then elaborated on, following which it was concluded that the overlapping fibre rhombus can be treated as an RVE and not as an RUC due to its lack of periodicity. This also meant that the submodelling approach was then chosen as the best option for pursuing a global-local analysis without periodicity constraints and homogenisation. Finally, to suit the requirements for the submodelling method, a winding design and mandrel were selected that allowed for the creation of optimally sized rhomboidal RVEs for this project.

This page was intentionally left blank.

5

Material Models

5.1. Rubber Material Model

With the introduction of various hyperelastic models for rubber in chapter 2, the task now is to choose a suitable Helmholtz potential form that fits the test data for the natural rubber used for this project. As discussed in section 2.3, several researchers have proposed physically motivated and phenomenological models similar in form to equation (2.8) to describe the behaviour of rubbers. This study will concentrate specifically on the phenomenological models due to the minimal experimental parameters needed to calibrate them, and their widespread use in literature. Additionally, only incompressible hyperelastic models will be dealt with considering the fact that natural rubber has negligible compressibility [16], and that the characterisation of its compressibility is highly dependent on the test setup. This will be discussed further in chapter 8.

An extremely popular description for the rubber hyperelastic response is via the use of Ogden- type models [18], which describes the Helmholtz potential in terms of the principle stretches - see equation (5.1). Here, μ_p and α_p are a set of dimensionless constants which can be fitted to the material data in multiple modes of deformation using a least squares algorithm. This model type was chosen for this project as it has a proven track record for modelling rubbers accurately [14], [16], benefits from data from multiple loading modes, and is able to capture all the non-linearities in the rubber response, including the 'upturn' in the stress-strain behaviour (see figure 5.1).

$$\Psi = \sum_{p=1}^{N} \frac{2\mu_p}{\alpha_p^2} \left(\lambda_1^{\alpha_p} + \lambda_2^{\alpha_p} + \lambda_3^{\alpha_p} - 3\right) \tag{5.1}$$

Rubbers have differing stress-strain responses for different loading modes as seen in figure 2.6. For calibration of any hyperelastic material model, it is imperative to include test data from as many deformation modes as possible in the strain interval of interest to ensure an accurate model fit. Failure to do so may result in loss of uniqueness of the material parameters [84], implying that although material characterisation using only a single mode of deformation is theoretically possible, it is possible to find a wide range of possible material parameters for a given set of experimental data. The effect of this non-uniqueness on the material description is not negligible.

For this study, rubber samples each were studied in three modes - uniaxial tension, biaxial tension and planar tension in the following strain ranges:

- Simple Tension: 0 % to 250%

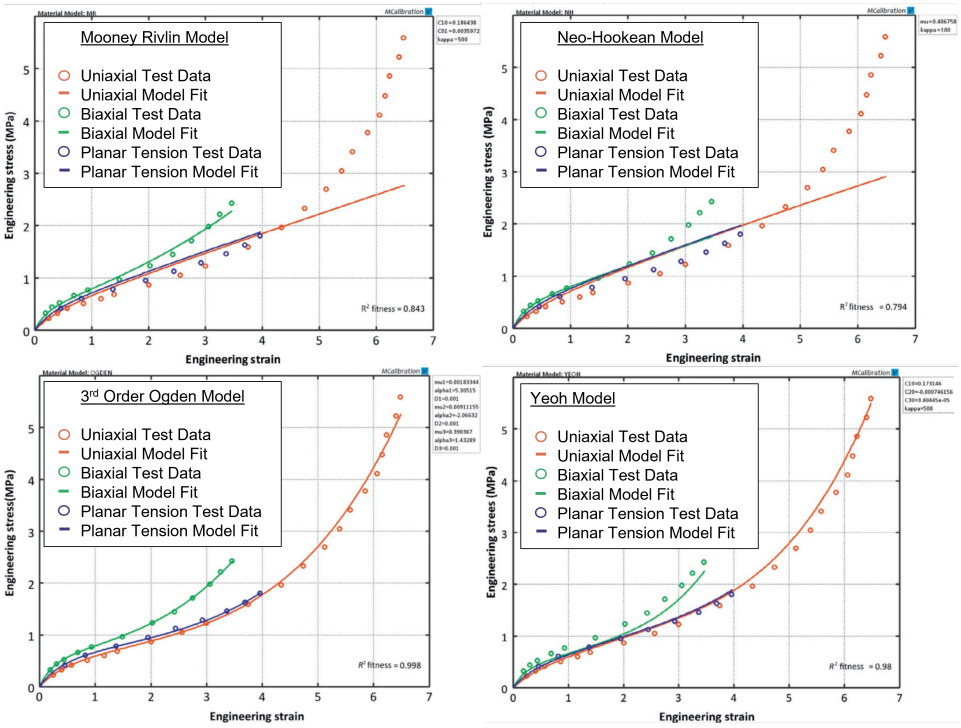

Figure 5.1: Fit comparisons between several phenomenological hyperelastic models and experimental data from Treloar [82], [83]

- Biaxial Tension: 0 % to 100%
- Planar Tension: 0 % to 60%

Fitting data to hyperelastic models from multiple repetitions of the same test is not as straightforward as fitting data to linear elastic models. Here, key parameters such as the linear elastic moduli and Poisson ratios cannot be averaged from several data sets. Instead, the entire data set is required. The data cloud from the physical tests was fit to a 6^{th} order Ogden hyperelastic model as shown in figure 5.2 using a non-linear least-squares technique by Twizell and Ogden [85]. The calibrated list of constants may be found in table 5.1. The theory behind this fitting procedure may be found in appendix C.

$\boldsymbol{\alpha}_1$	$\boldsymbol{\alpha}_2$	$\boldsymbol{\alpha}_3$	$\boldsymbol{\alpha}_4$	$\boldsymbol{\alpha}_5$	$\boldsymbol{\alpha}_6$
-0.131	0.503	4.828	-0.412	-1.471	-2.129
$\boldsymbol{\mu}_1$	$\boldsymbol{\mu}_2$	$\boldsymbol{\mu}_3$	$\boldsymbol{\mu}_4$	$\boldsymbol{\mu}_5$	$\boldsymbol{\mu}_6$
1.284	-7.760	0.103	16.172	-13.448	4.631

Table 5.1: Calibrated constants for the 6^{th} order Ogden model as shown in equation (5.1)

From figure 5.2, an acceptable fit is seen for all modes barring planar tension. Even here, the fit is acceptable until a stretch ratio of $\lambda \approx 1.3$. Beyond this, the upturn in the data is not captured. This may be partly due to the limitations of the model itself, and partly due to the approximations made for the planar tension test. This is elaborated further in section 8.1.3.

5.2. Fibre Material Model

The PET cords used for this project have a complex double twisted structure - see figure 5.3. First, several twisted filaments make a single yarn, and then multiple yarns are twisted together in a direction opposite to that of the filament twist to create a single cord. Modelling each cord as a structure, either analytically [28], [29] or numerically [27] is extremely computationally expensive, and requires

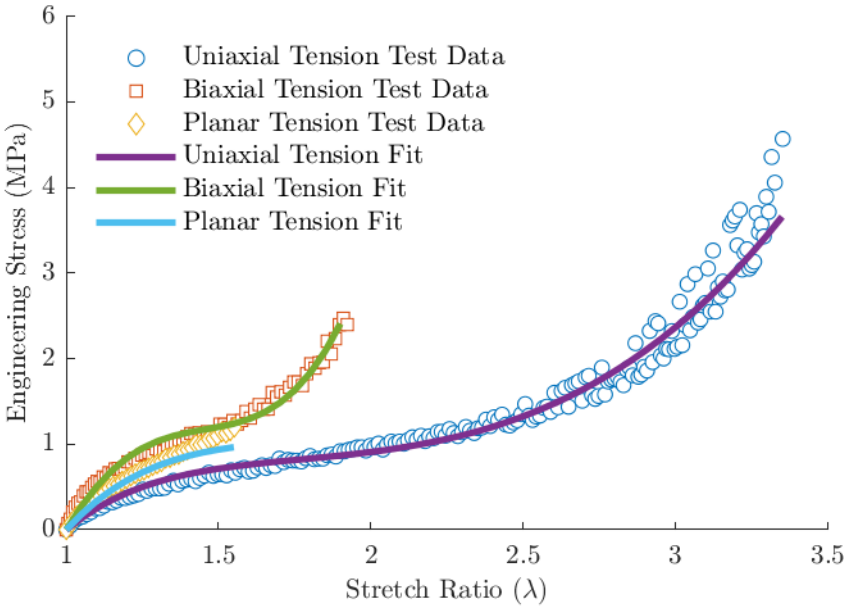

Figure 5.2: 6^{th} order Ogden model fit to data from multiple loading modes

the development of a multi-scale model. Since this is not the aim of the current work, it was chosen to treat the fibre as a continuum.

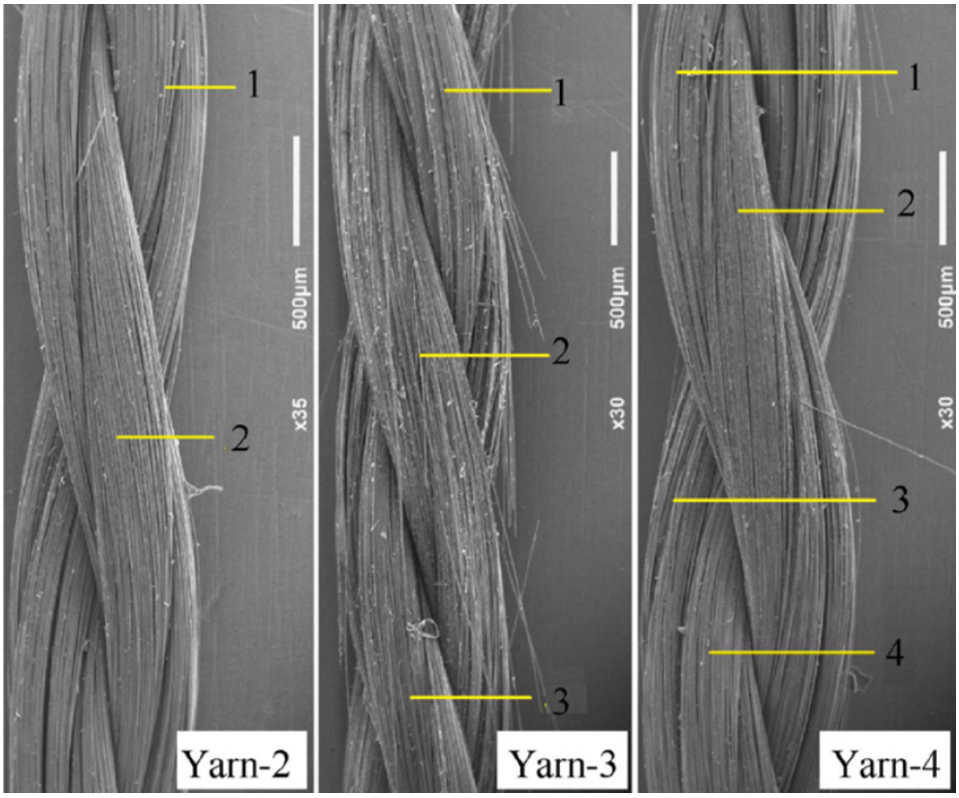

Figure 5.3: SEM image of twisted cords. Yellow markers indicate number of twisted fiber bundles in each cord [31]

To study the PET cord's behaviour as a continuum under tensile loading, monotonic tensile tests were carried out (see chapter 8) at the DASML. Despite the behaviour of solid homogeneous PET being roughly linear elastic [86], a characteristic hyperelastic shape emerges for these doubly twisted cords

- see figure 5.5. Li et. al [30] studied the behaviour of such doubly twisted nylon tire cords under monotonic loading and observed a similar response shape - see figure 5.4. It was theorised that the twisted structure itself, and the resulting interactions between filaments in the bundles were responsible for the unique non-linear response. With reference to figure 5.4, Li suggested that region A shows an initially high but rapidly deteriorating stiffness due to the breakdown of the polymer coating on the twisted cords. This binder coating helps to transmit load and is a vital component to prevent the twisted cord from opening up under low loads. However, as tensile loads build up, the cord twist tightens up, and the twisted structure is able to transmit loads via inter-bundle friction. This is characterised by the rapid increase in stiffness in region B. Finally, as the filaments approach their yield strength, another region of softening is observed in region C.

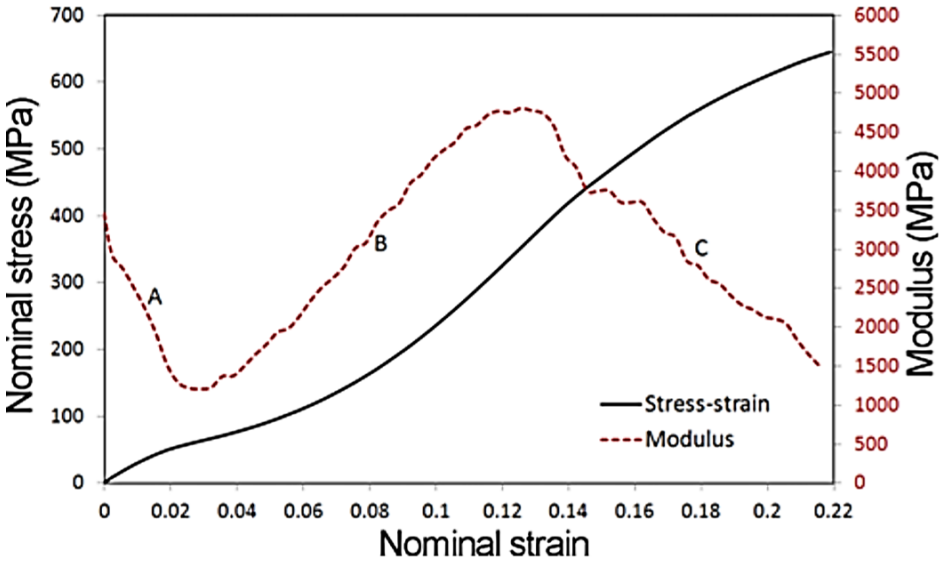

Figure 5.4: Tensile response of Nylon-66 cord [30]

Li then proposed a specialised hyperelastic Helmholtz energy potential with calibration constants $C_{i,j}$ to model such fibre behaviour - see equation (5.2). Here I_1, I_2 are the two invariants of the left (or right) Cauchy-Green deformation tensor.

$$\Psi = \sum_{i,j=0}^{N} C_{ij} \left(I_1 - 3\right)^i \left(I_2 - 3\right)^j, (C_{00} = 0) \tag{5.2}$$

On closer inspection of equation (5.2), it is evident that the model itself is purely phenomenological, and is made to fit only uniaxial tension data. Thus, any model that captures this uniaxial tension response reasonably may be considered for modelling the cord stress-strain response. One of the ideal models developed by and pre-implemented in ABAQUS is the Marlow material model [87]. This model assumes that for a single deformation mode, the Helmholtz strain energy density (Ψ) can be defined only in terms of the first invariant $I_1 = tr(\mathbf{B})$. This implies that no functional form of Ψ is needed to define the strain energy density, and thus the exact stress-strain response is captured without the need for curve fitting. A brief summary of the method described by Marlow is found in appendix B.

This time, a curve averaging approach using linear interpolation was used to collapse the stress-strain responses of all the cord test specimens into the single curve. ABAQUS's built-in model calibration tool was then used to fit the Marlow model to the averaged curve. The result is seen in figure 5.5, where the exact replication of the test data is evident.

It must be noted here that the cord material model created assumes that the cords are isotropic and perfectly incompressible. In reality, due to their twisted nature, the cords are much softer in their transverse direction compared to their axial direction [88]. This is especially true in transverse tension,

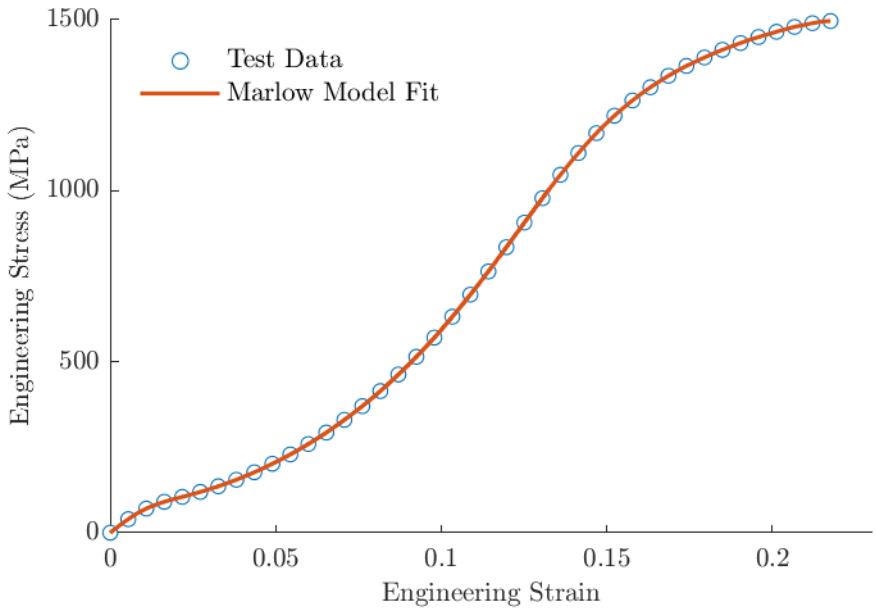

Figure 5.5: Marlow model describing the averaged uniaxial tensile response of the twisted PET cord

where the tension causes the yarn to unravel and untwist. The effect of this assumption on the model performance can be investigated in future studies using the recommendations listed in section 9.2.

5.3. Interface Material Model

With the goal of studying the cord-rubber interface using a cohesive model, pull-out tests were conducted at the DASML to help calibrate a bilinear traction-separation law. Here, a solitary fibre was pulled out of a vulcanised block of rubber under displacement-controlled conditions, and the force-displacement plot was recorded. For a detailed explanation of these experiments, readers may refer to chapter 8.

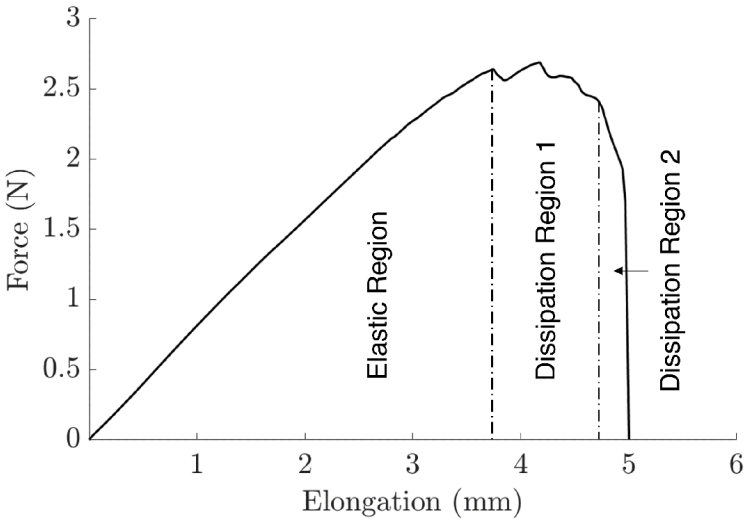

Figure 5.6: Force-displacement plot for single pull-out test specimen

On conducting these tests, it was noticed that due to the relatively low stiffness of both the cord and the rubber, large displacements were seen in the experimental data. These displacements made it difficult

to distinguish between normal elastic deformation, and deformation due to damage-induced inelastic sliding. The force-displacement response of a single representative pull-out sample is seen in figure 5.6, where three distinct regions are visible. The first region represents initial elastic deformation without damage. This is followed by the first dissipation region. Here, due to the nature of the tooling to create the test specimens (figure 8.12), there are trace amounts of rubber deposition around the fibre region forming a 'rubber lip' - see figure 5.7. Being highly elastomeric, these depositions undergo large deformations and carry load even after the complete failure of the interface. This balance of elastic and inelastic responses creates a plateau in the load-displacement response. Finally, there is the catastrophic failure of this rubber lip - see figure 5.7b leading to a sudden drop in carried load. This is depicted by the second dissipation region.

The presence of these three distinct regions in the response curve indicates that the captured response is not purely of the interface, but of the entire structure. This means that it is very difficult to separate regions of the curve dominated by interface degradation from regions of the curve affected by other processes. Additionally, despite care to ensure consistency, there was considerable variation in the production of these samples, leading to differing sizes of this rubber lip. These stochastic effects meant that getting a reliable prediction of the fracture toughness of the interface was extremely difficult. Thus, to avoid relying on assumptions, the data was not used and the cohesive material model was not formulated. Additional tests using improved tooling were also not conducted due to time limitations.

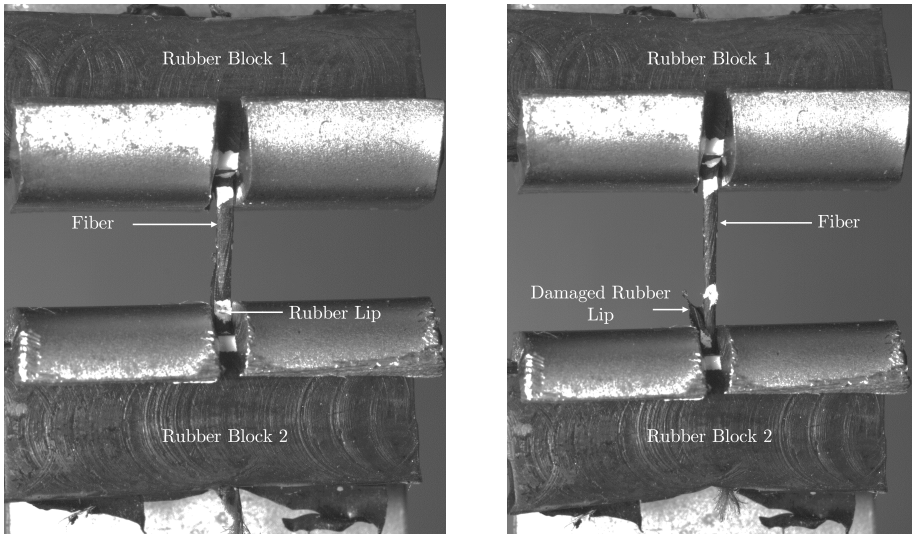

(a) Pre-damage **(b)** Post-damage

Figure 5.7: Interface pull out test specimen under uniaxial tensile loading

5.4. Conclusion

In this chapter, the decision to model the constituent fibres and rubber of the model with hyperelastic material models was motivated. The 6^{th} order Ogden model was chosen to model the rubber, with the model being calibrated with experimental data from all three modes of deformation - uniaxial tension, biaxial tension and planar tension. For the fibre, the decision to model the complex twisted structure as a continuum was motivated, followed by the decision to model the same using the Marlow hyperelastic model. Both the rubber and the fibre are modelled as perfectly incompressible solids. Experimental data was fit to the hyperelastic models using a curve averaging approach, which helped reduce multiple data sets to a single curve along a common X-axis. Finally, the challenges of creating an interface material model using the pull-out experiments conducted were highlighted. Due to these challenges, it was decided to not use the obtained material data for calibrating the interface material model for this project.

6

Building the FEA Model

This chapter elaborates on the creation of local and global models for the submodelling analysis. For this, a novel method to transfer the displacement boundary conditions was developed, which will be elaborated upon. Fibre damage is introduced in the model, which will be explained in detail.

6.1. Global Model

In this section, the development of the global model is highlighted. First, the choice to homogenise the fibre winding pattern with rebar is motivated. Subsequently, the performance of the rebar is compared with experimental data from the literature to test its feasibility. Finally, the details of its implementation in the global model are elaborated upon.

6.1.1. Rebar as a fibre homogenisation tool

As discussed in chapter 4, the task of the global model is to accurately transfer displacement boundary conditions to the local model without being computationally expensive. For this, a homogenised solution is often the most optimal approach, where global fidelity is traded for computational ease. For conventional composites, global-local analyses often use homogenised shell models to model the composite layup in the global domain [89], [90]. For the current project, homogenisation schemes could be explored to model the undulating fibre geometry using 2D surface elements.

Perhaps the most studied homogenisation scheme to model CRC structures is the use of *rebar* layers [49]–[53]. Here, an orthotropic continuum is created for the fibre layer based on material properties, fibre angles and fibre spacings defined by the user [91] - see figure 6.1. Using this technique, regions with uniform fibre spacing, fibre angles and fibre cross-sections can be represented as a singular rebar section.

Choosing the rebar homogenisation approach has several advantages:

- It has the capability to represent complex filament winding parameters by only the three parameters mentioned in figure 6.1.
- There is independent modelling of the rubber and fibre allowing each component to be modelled with its own representative material model.
- Rebar allows for hyperelastic material models to be used in its material definitions. This allows the Marlow model to be used for the fibre as detailed in chapter 5.

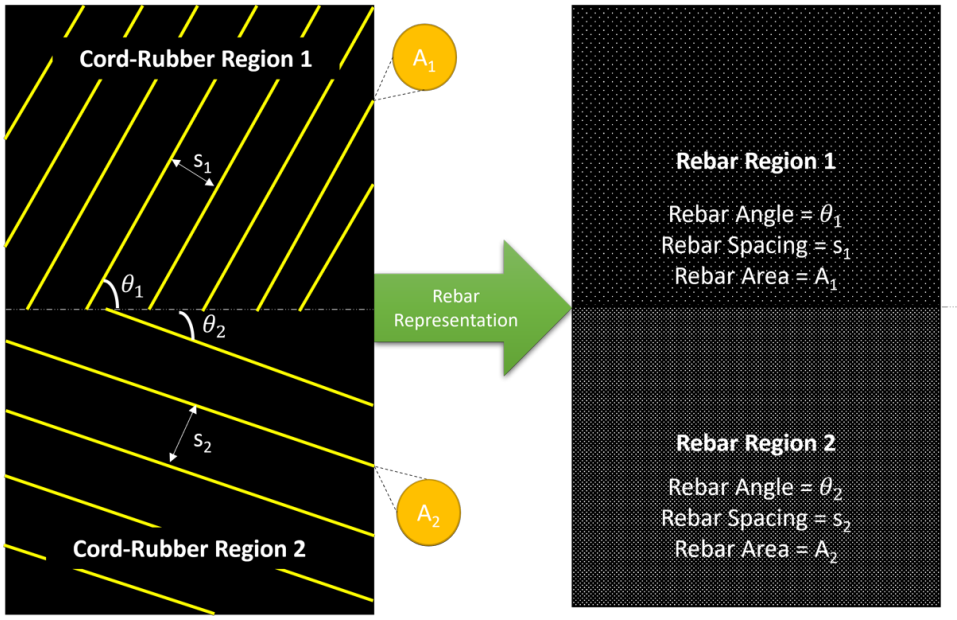

Figure 6.1: Representation of two different CRC regions with equivalent rebar formulations

- In non-linear analyses under large displacements, rebar accounts for the change in fibre cross-sectional areas, fibre angles and fibre spacings (see appendix A for brief continuum formulation). This means that the rotation of the fibres represents actual deformation, and hence should be able to capture key phenomena such as fibre scissoring and realignment.

6.1.2. Rebar Performance

Before committing to the rebar model to analyse the global behaviour of the CRC structure, it is worthwhile to examine its performance against experimental data. Specifically, the following parameters should have acceptable performance for the method to be considered:

1. Accuracy in displacement solution.
2. Accuracy in fibre angular rotations.
3. Rapid convergence of displacement solution.

To check the above parameters, experimental data by Weiser et. al. [25] was used. Weiser studied the performance of a two-layered CRC cylinder with fibre angle $\alpha = \pm 10°$ under simultaneous internal pressurisation, compression, and torsion. The product construction and its subsequent layers can be seen in figure 6.2. The exact experimental setup along with the boundary conditions can be found in [92].

Using provided measurements of fibre angles, fibre spacings and product dimensions from [25], a rebar model was created as shown in figure 6.2c. The hyperelastic Marlow material model was used to model both the rubber and the fibre behaviour as only uniaxial tension data was provided for the materials in the publication.

The comparison of the load vs. displacement curves for the rebar model and the experimental demonstrator is seen in figure 6.3. An acceptable level of deviation is seen, with the maximum error being 5.13%. Apart from errors due to homogenising the helical pattern, contributions to the deviation may also be due to ignoring the gap between the $+\alpha°$ and $-\alpha°$ layers, which are not filament-wound but rather produced as individual layers. Additionally, rebar is modelled as a 2D surface, and hence any

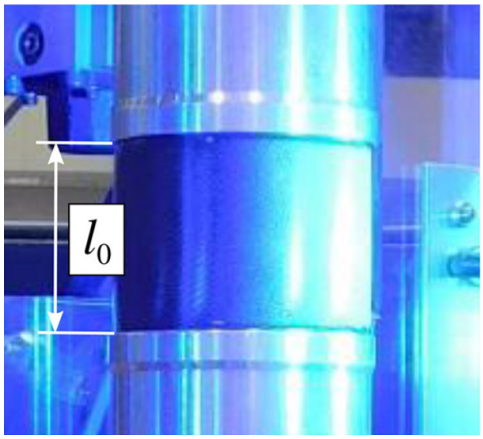

(a) Demonstrator pre-deformation

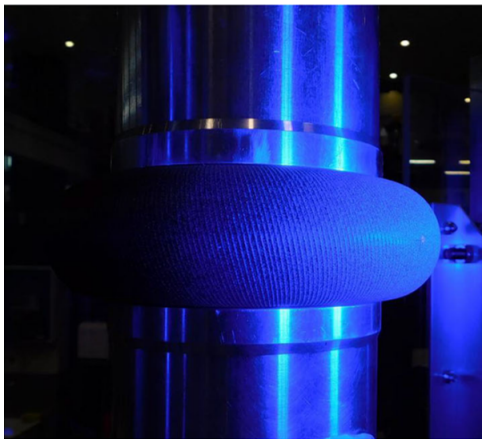

(b) Demonstrator post-deformation

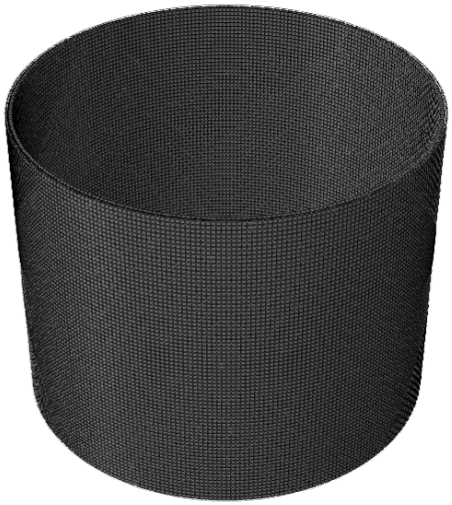

(c) Rebar model pre-deformation

(d) Rebar model post-deformation

Figure 6.2: Construction of CRC demonstrator by Weiser et. al. [25]

volume occupied by the fibres is ignored. This may affect the fibre volume fractions, and thus may also contribute to the error.

The second performance parameter to be studied is the fibre angle change (scissoring) under loads. The study by Weiser does not quote angular rotations of the fibres. Despite this, a rough estimate may be arrived at if the fibres are modelled using truss elements. To do so, a Python script was written that generated the required helical fibre geometry in ABAQUS - see figure 6.4. The resulting angular rotations of the truss elements are then compared with the rebar angles to check for agreement.

Figure 6.5 shows the comparison between the rebar fibre angles and the truss angles at the midsection of the demonstrator under a loading history defined in [92]. Despite not being a perfect match, the agreement between the data, with a maximum deviation of 8.3%, is an acceptable margin for rebar to be considered as an ideal modelling technique for the global model. This is because the source of this error is compounded due to modelling simplifications in both the rebar and the truss models, and hence no conclusion on the accuracy of the model, except a general higher-order agreement, can be drawn. For an exact comparison, experimental data would be needed.

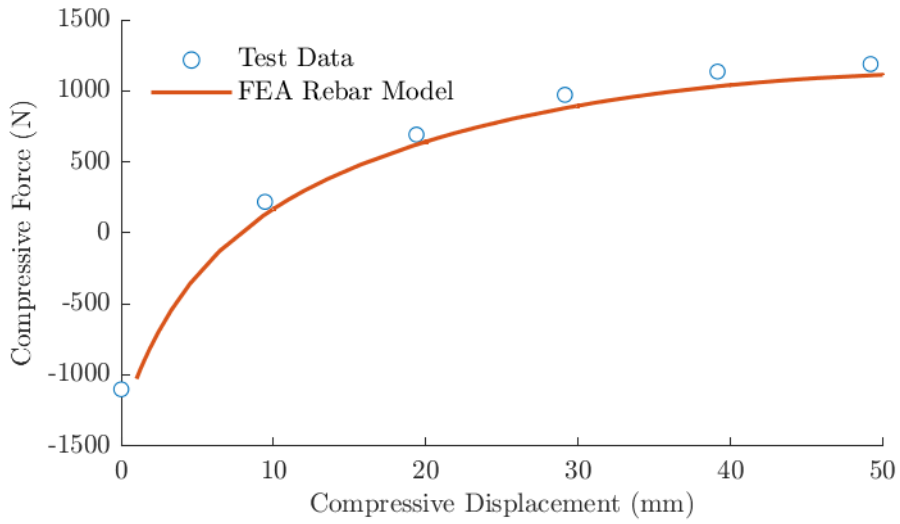

Figure 6.3: Comparison of experimental data by Weiser [25] with rebar FEA model

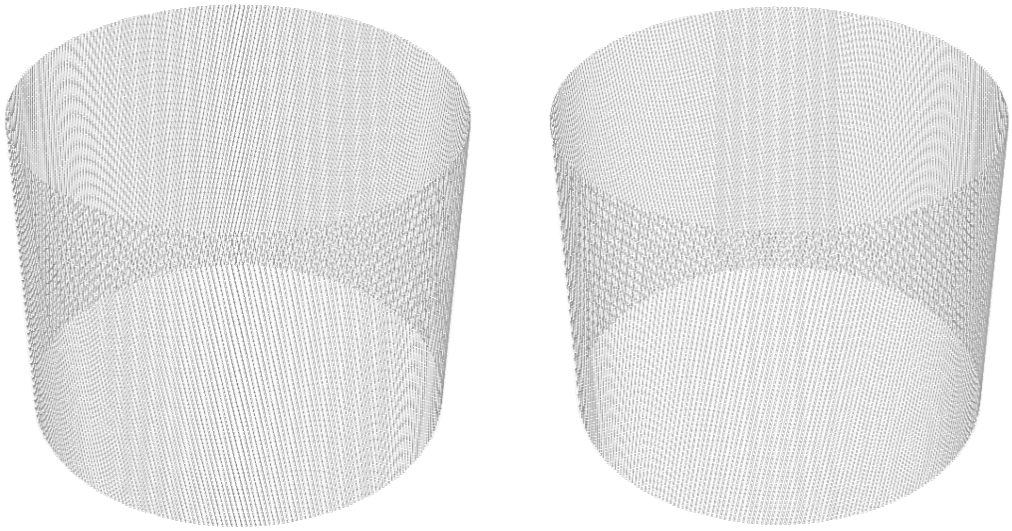

(a) $+\alpha^\circ$ layer **(b)** $-\alpha^\circ$ layer

Figure 6.4: Truss fiber model replicating demonstrator by Weiser [25]

Number of Elements	% Change in Elements	Average Reaction Force (N)	% Change in Reaction Force
3094	-	227.62	-
3370	8.92	226.53	0.48
3876	25.27	225.31	0.54
4862	57.14	224.36	0.42
7650	147.25	223.43	0.41
23256	651.65	222.39	0.47

Table 6.1: Rapid convergence of rebar reaction forces, which is indicative of the displacement convergence rate

The final requirement is that the global model should have rapid displacement solution convergence. To demonstrate the same, an earlier study by the author [59] was used. Here, the convergence behaviour of rebar was studied extensively using a representative CRC rectangular specimen with biased fibres at $\alpha = 60^\circ$ under uniaxial displacement loading. The rate of convergence of the rebar stresses was compared against that of the end reaction forces. Being a complementary quantity to displacements,

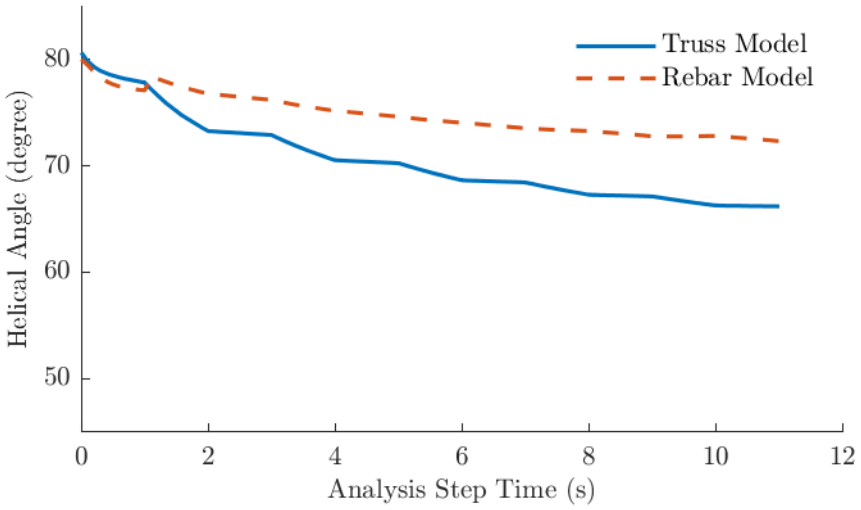

Figure 6.5: Comparison of fibre helical angles between the truss and rebar FEA models.

the force convergence should indicate the rate of displacement convergence when force loading is applied. Table 6.1 shows the data for five mesh sizes. Rapid convergence is seen for the reaction force solution, while the stress solution tends to be highly mesh dependant. Since only displacements are needed for the global model, this rate of convergence is more than sufficient.

6.1.3. Global Model Description

With the choice of rebar to model the fibre winding pattern in the global model made, the global model itself can be created. To model the CRC product accurately, its construction must first be understood. Figure 6.6 shows the construction of the prototype. The upper and lower metallic flanges are bolted tightly together, thus sealing the polar opening of the CRC prototype between them and forming a leak-proof connection. The seating of the flanges is an important step in ensuring the water pressure is contained by the prototype on internal pressurisation, and thus the bolts must be torqued adequately.

The chosen CRC product to be modelled is symmetric about its axis and also about its length. This allows the creation of a greatly reduced global model with symmetry about both the Z and the θ axes - see figure 6.7. The circumferential angle included in the model depends on the dimension of the local rhomboidal RVE. This aspect is detailed in section 6.2. The rubber region is modelled using 8-noded linear *hybrid* brick elements (C3D8H), while the fibres are modelled using quadrilateral surface elements (SFM3D4) with ABAQUS' inbuilt rebar formulation. Hybrid elements [93] are specifically developed to tackle incompressible material behaviour. In such materials, the displacement solution is not sufficient to obtain accurate results as hydrostatic pressure may be applied to incompressible materials without any changes in displacement. This is solved by treating the pressure stress as an independent variable, which is then coupled to the displacement solution using constitutive theory [94].

For modelling the flange, the local effects due to the clamping of the flanges and the subsequent squeezing of the rubber are ignored. Instead, the flange is modelled as an analytical rigid body that is connected to the lip of the rubber opening via tie constraints. Subsequently, to aid the stability of the solution, the flange itself is constrained to move only along the axial direction (Z) under pressure loads. Ignoring the local effects at the ends of the model is possible as the region of interest is the central cylindrical region, and thus any local effects occurring at the ends would be unlikely to have a major influence on the displacement solution in the cylindrical section.

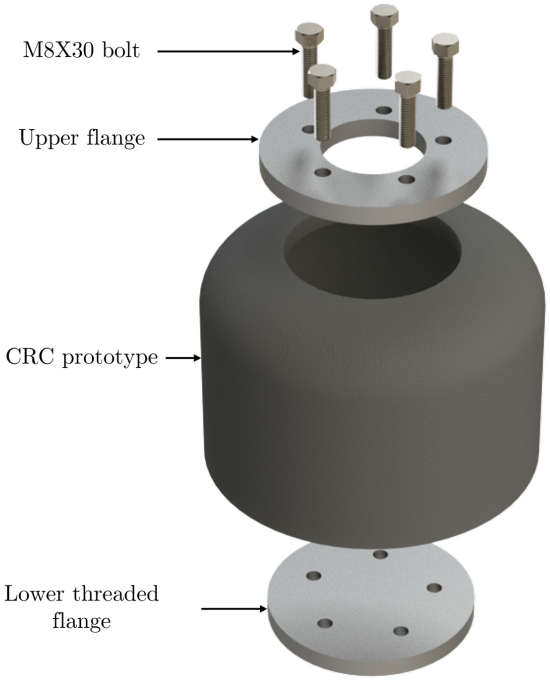

Figure 6.6: CRC prototype exploded view (half length)

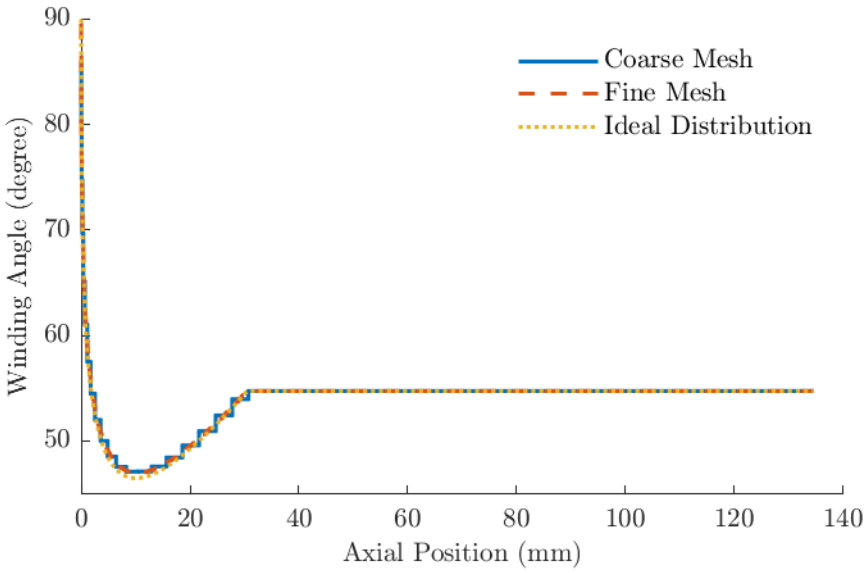

Figure 6.8: Effect of rebar mesh size on winding angle distribution along the length of the prototype (half-length shown here)

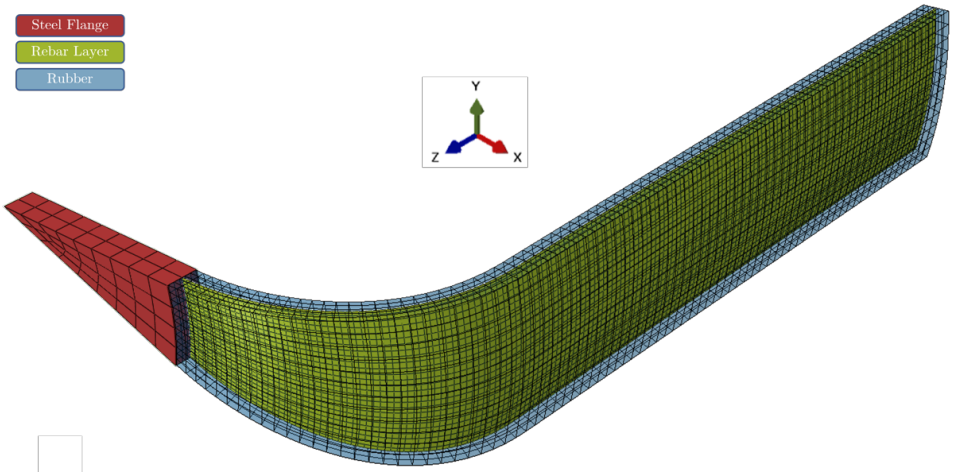

Figure 6.7: Global model

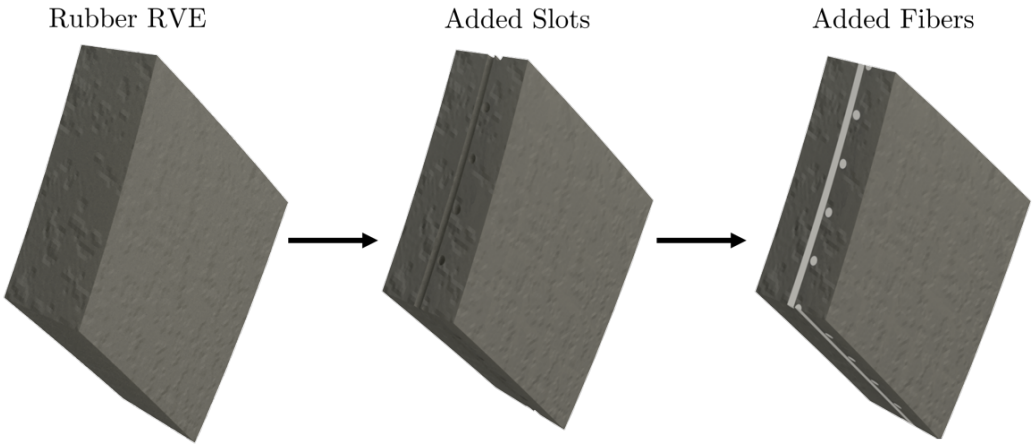

Figure 6.9: Stepwise creation of RVE solid model

To define the rebar section, three parameters are needed - the winding angles, the rebar spacing, and the fibre cross-sectional area. As seen in figure 4.7, the rebar winding angles are constant over the cylindrical region but change rapidly over the polar domes. This variation in winding angles affects the global displacement solution directly, and thus must be included in the model. Rebar sections can only be assigned discretely, with each section having a common winding angle and rebar spacing for all the material points in the element. Thus to do so, a Python script was written that interpolates between the winding angles generated by TaniqWind and then creates unique sections for each element based on the required winding angles and spacings at that location. This creates a step-wise discretisation of the fibre winding angles (see figure 6.8) - which can be adjusted to the required fidelity by adjusting the mesh size.

Finally, the rebar surface was placed along the centre of the rubber thickness using the embed constraint [95]. The embed constraint links the nodes of the embedded fibres to the nodes of the rubber matrix via a weighted set of kinematic constraints. Once this is done, the translational degrees of freedom of the fibre itself are deleted as they are now completely dependent on the translations of the linked rubber nodes.

6.2. Local Model

For the local model, a CRC rhomboidal RVE is created using the fibre overlap pattern shown in figure 3.9 by adding a rubber layer around it. The required geometry was created in Solidworks as shown in figure 6.9. The complexity of creating the rubber solid geometry lies in the fact each face of the rubber part is a complex 3D curve with no planar faces. This, coupled with the created fibre slots makes the rubber geometry extremely uneven, and thus it is not possible to model it using quadrilateral elements.

Instead, linear hybrid tetrahedral elements (C3D4H) were used to mesh the rubber. Usually, linear tetrahedral elements are avoided for modelling incompressible materials as they undergo volumetric locking that creates an overly stiff response [93]. However, as explained previously, *hybrid* elements use the pressure stress as an independent variable and thus are able to avoid the issue of volumetric locking. This allows linear tetrahedrons to be used without compromising the solution accuracy or increasing the mesh size a lot. The rubber mesh - see figure 6.10 was optimised to have maximum resolution near the fibre slots while having a coarser seed near the outer peripheries. This allows for good compatibility between the rubber and fibre meshes at the interface.

The fibres were modelled using quadratic hybrid wedge elements (C3D15H). Wedge elements were specially chosen for the fibre as they can be meshed circumferentially about the central axis of each fibre - see figure 6.10. This is desirable as material data for transverse deformation of the fibre is

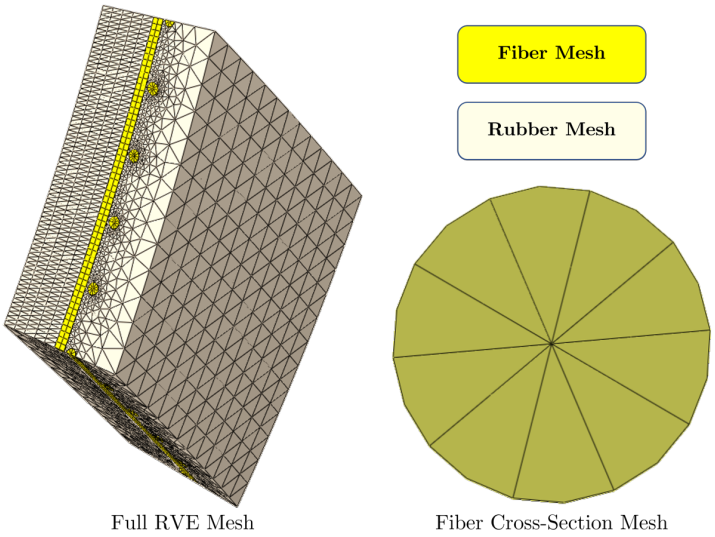

Figure 6.10: RVE Mesh

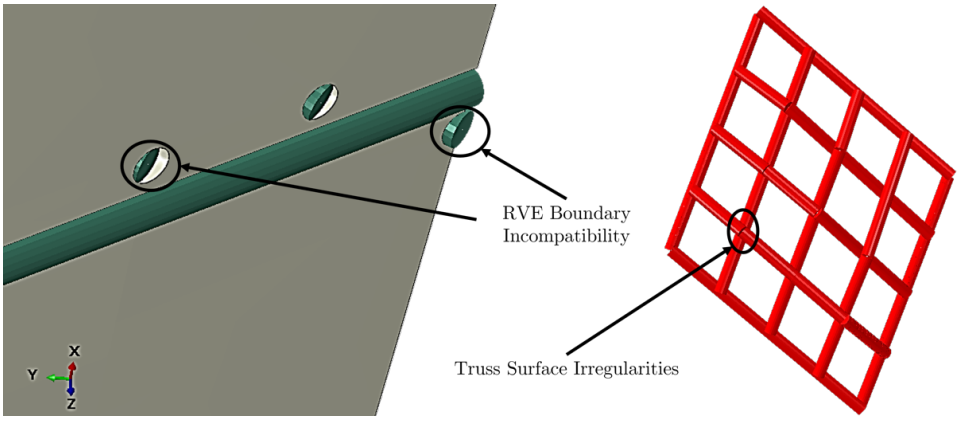

Figure 6.11: Issues with using 1D truss elements in local model

not available, and thus capturing fidelity in this direction by increasing mesh density is not beneficial. Initial attempts were made to model the fibres using truss elements to ensure that load is transmitted only axially. However, attempts to use the contact algorithm at the rubber-fibre interface using this formulation proved to be very troublesome due to irregularities in the truss projected surface created by ABAQUS (see figure 6.11). Additionally, due to their 1D nature, it was not possible to create the geometry at the RVE boundary accurately. This meant that solutions using truss elements actually took longer in terms of CPU time than comparable solutions with wedge elements.

6.3. Damage Model

With the creation of the local model, damage to the constituent materials may be added to predict the burst pressure of the product. This section details the inclusion of damage in the local model and explains its implementation.

6.3.1. Rubber Damage

Natural rubber, with a failure strain usually exceeding 100%, is unlikely to undergo tensile failure in the strain regime expected in this study. Additionally, even rubber shear-banding [96]–[101], which is

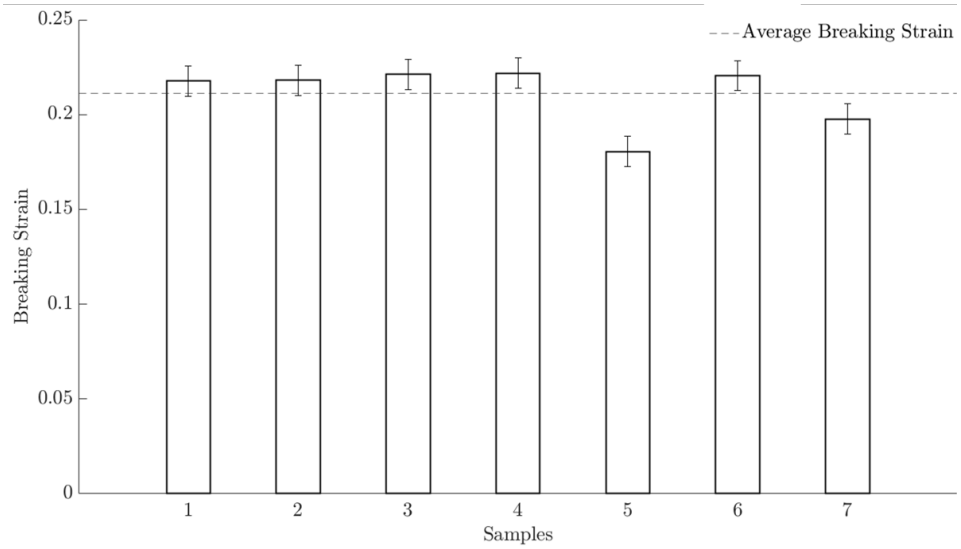

Figure 6.12: Fiber failure strains

an important failure mode in open-ended CRC structures, is irrelevant for this study considering the rubber has no 'free-ends' due to its asymmetric geometry. Hence, rubber damage is not modelled in this study. Modelling of any low-strain damage effects arising due to cyclic loading, such as Mullins damage[16], is not within the scope of this project.

6.3.2. Fiber Damage

Fibre damage is the principal source of damage in CRC structures [102]–[104]. This is especially true in filament wound structures, in which 'fibre-fretting' is a key cause of fibre failure in the regions of fibre overlap [63], [67]. Noting that only the uniaxial tensile behaviour of the fibres has been studied via tensile tests (for details, refer to chapter 8), a failure criterion that relies only on field variables in this direction is considered appropriate. Thus, a simple maximum axial strain (ϵ_{11}) failure criteria was used for the fibres. Based on seven experiments, the average failure strain was evaluated to be $\epsilon_{crit} = 0.211$ - see figure 6.12.

To define the axial direction of the undulating fibres in the local model, unique local material coordinate systems were defined for each fibre element using a Python script. The maximum strain criteria itself was implemented using the user subroutine - USDFLD [105] via a Fortran script. The subroutine modifies the formed tangent stiffness matrix at each material point in every increment and sets the stiffness to numerical zero for every material point that exceeds the set strain limit. In this way, the element can be 'deleted' without altering the element connectivity.

One crucial aspect to keep in mind while implementing such a solution is that element deletion does not allow the conservation of energy (or mass, for dynamic analyses). Every time an element is deleted, there is a sudden and irrecoverable loss of energy which is not in agreement with Griffith's theory of stable crack propagation [74]. This loss in energy is also highly mesh-dependent, with a courser mesh leading to a greater loss in energy per deleted element than a fine mesh. Despite this, this model may still be used, within engineering precision, as the fibres undergo a sudden and brittle failure - see figure 6.13.

6.3.3. Interface Damage Model

In most CRC products, including the one used for this project, the cords are dipped to form a coating that allows better adhesion at the cord-rubber interface. For this project, the cords were coated with a

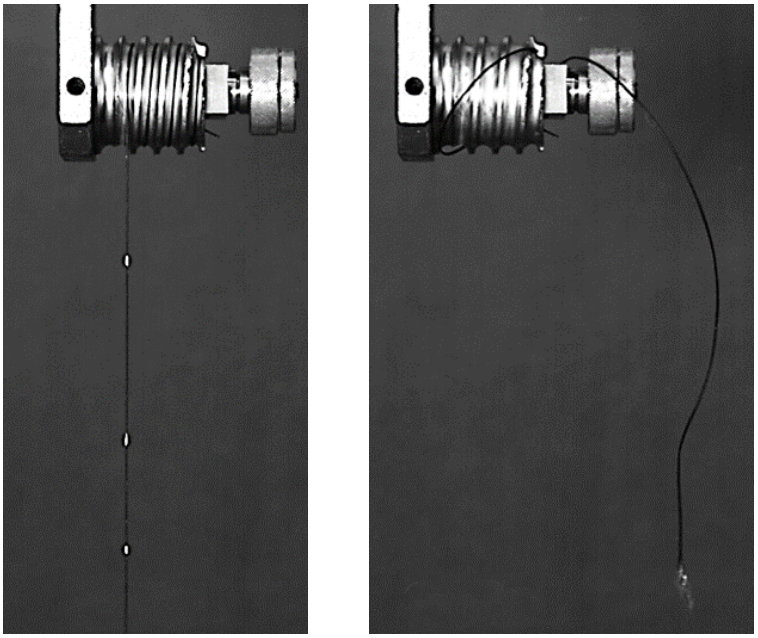

(a) Intact Fiber **(b)** Broken Fiber

Figure 6.13: Brittle failure of fibre under uniaxial tensile loading - images taken 0.5 s apart

Resorcinol–Formaldehyde–Latex (RFL) [106] coating, which is an adhesive system that allows textile-like materials to have better adhesion to rubber.

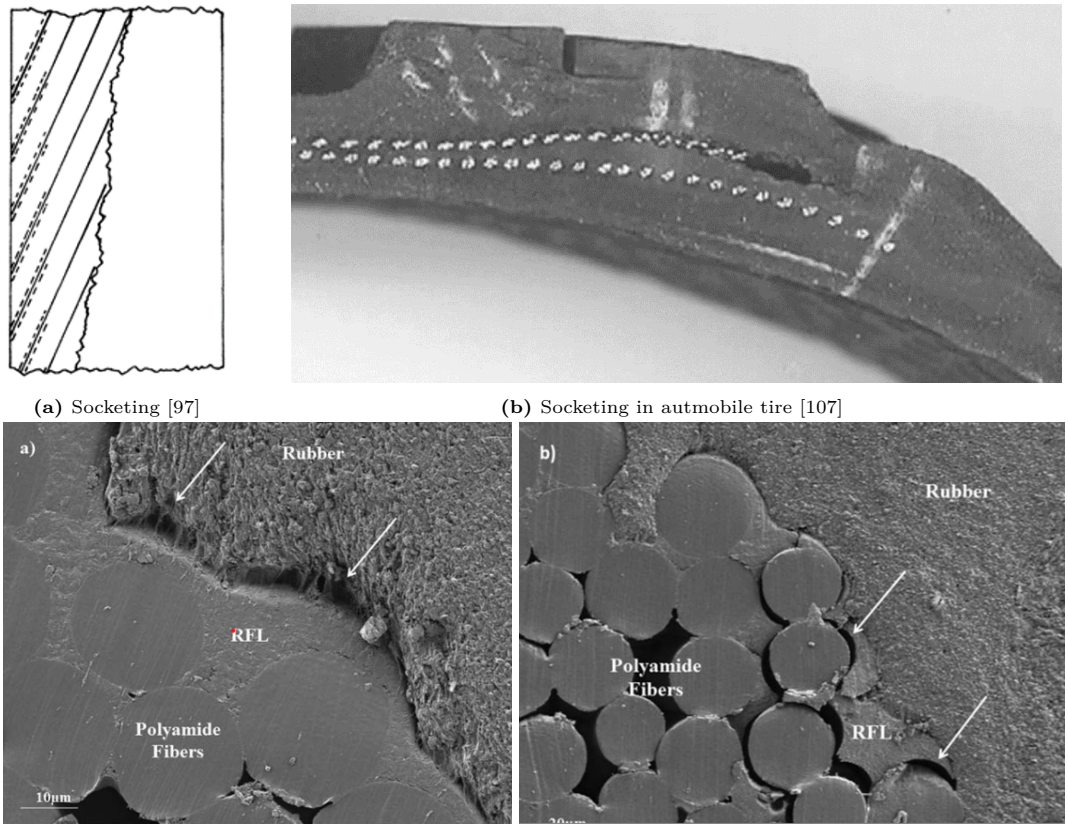

(a) Socketing [97] **(b)** Socketing in autmobile tire [107]

(c) Fibrillar microcracking at cord-rubber interface [108] **(d)** RFL-cord debonding [108]

Figure 6.14: Cord-Rubber interface damage modes

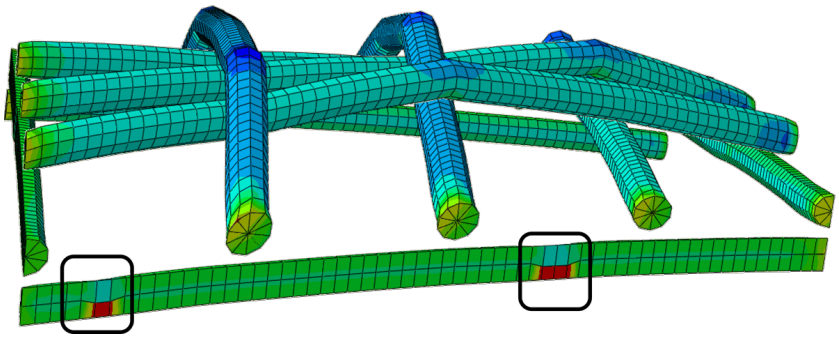

Figure 6.15: Regions of unrealistic distortion in local model using ABAQUS submodelling

Figure 6.14 shows commonly studied modes of interface damage in CRCs. Probably the most studied form of such failure is 'socketing' and fibre-matrix debonding [96], [100], [104], [109]. This is particularly common in CRCs due to the large stiffness differences between the cord and the rubber leading to a highly stressed interface. Here, a cylindrical debond grows along the length of the fibre at the cord-rubber interface - see figure 6.14a. Valatin et. al [108], via a multi-instrument experimental approach, ascertained that the interface debonding for an RFL coated cord-rubber interface is of two types - fibrillar microcracks at the RFL/rubber interface (figure 6.14c), and debonding between the RFL and the embedded cord - (figure 6.14d). These cracks are the first signs of failure in a loaded CRC and contribute to final failure via another mode by restricting load transfer between fibres via the matrix.

As detailed in section 5.3, creating a cohesive model was attempted but later rejected due to difficulty in interpreting experimental data to create the necessary model. Additionally, the complex geometry also made solution convergence very tricky in the damage (softening) phase of the cohesive law. In the time frame of this project, modelling interface damage, although highly desired, was not possible. Future studies may include the recommendations listed in section 9.2 to improve upon the model presented in this work.

6.4. Submodelling Implementation

With the creation of the local and global models individually, it is possible to link them via the submodelling approach. For the current case, a one-way submodelling approach is implemented, in which there is no feedback from the local model to the global model to correct for progressive stiffness degradation. The reasons for this are elaborated on in chapter 7.

ABAQUS has a built-in submodelling tool that was initially used [110]. In this method, the ABAQUS automatically interpolates between the nodal displacement solution of the global model and applies the necessary boundary conditions to appropriate nodes on the local model. The interpolation algorithm ensures that matching meshes between the boundaries of the local and global model are not needed for the consistent application of boundary conditions. Despite this, the interpolation is not always perfect, resulting in spots of unrealistic deformation - see figure 6.15. These nodes with excessive deformation often lead to non-convergence of the entire solution.

To combat the above issue, a novel implementation of the submodelling approach was created. Here, the local model boundary mesh is copied via a MATLAB script to form a surface mesh (SFM3D3/SFM3D4 elements) in the global model. This boundary mesh is then placed in the global model at the correct location via the embed constraint - see figure 6.16. The role of this surface mesh is to act as a $1:1$ representation of the local model within the global model and collect the boundary displacements. Having no material assignment, this surface mesh is free to deform without resistance according to the surrounding conditions in the global model. The displacements of this surface can then be applied as boundary conditions to the local model without any transformation or interpolation, thus fixing the issue seen in figure 6.15. A detailed flowchart representing the implementation of this submodelling

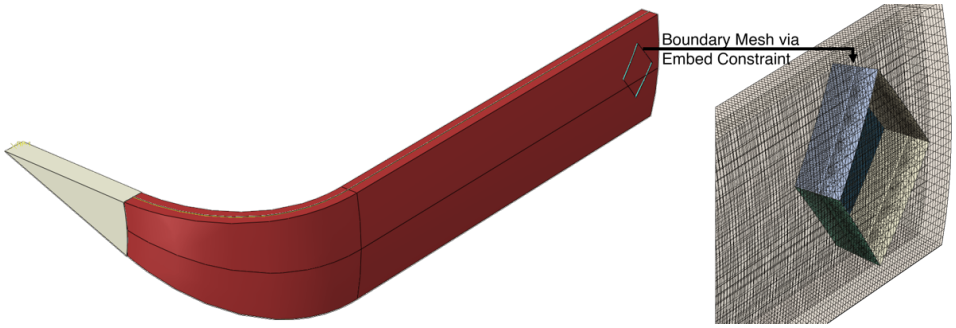

Figure 6.16: Positioning of surface mesh within global model using embed constraints

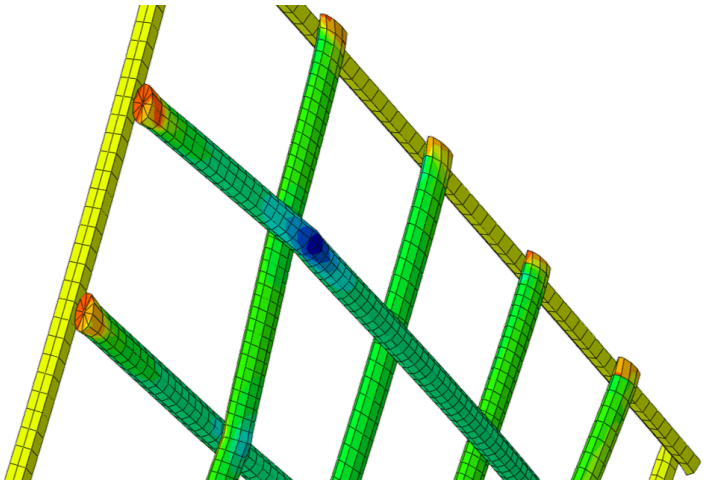

Figure 6.17: Yellow, orange and red elements signify boundary regions in local model with excessive deformation

method is seen in figure 6.20.

6.4.1. Effect on Damage Model

Transfer of boundary conditions using the submodelling approach as described poses a unique deformation state in the local model close to the boundary. In this region, the fibres show especially high transverse deformation - see figure 6.17. This can be explained by the fact that the global model has only a 2D rebar layer representing the fibres. Thus, all the boundary conditions are transferred to the local model from the deformation of the rubber elements only. Since these rubber elements are orders of magnitude softer than the fibre, the displacements are proportionately large, thus causing this effect.

Fortunately, these boundary effects are extremely local, and die out within only a few elements - see figure 6.18. To ensure that the damage model is not affected by the deformation of these elements, these boundary elements are excluded from the damage analysis. Thus, the only function of these elements is to transfer displacements to the interior elements without undergoing any damage themselves.

6.4.2. Automated Usage

Using the submodelling approach detailed in this section manually can be a painstaking process. This is because, for every new iteration of the model, a new local model has to be created, followed by the generation of a new boundary surface mesh, which then has to be embedded in a new global model. Additionally, transferring the nodal displacements back from the global to the local model for each node is almost impossible if done manually. Hence, an automation scheme was developed to allow the rapid creation of models with minimal user effort.

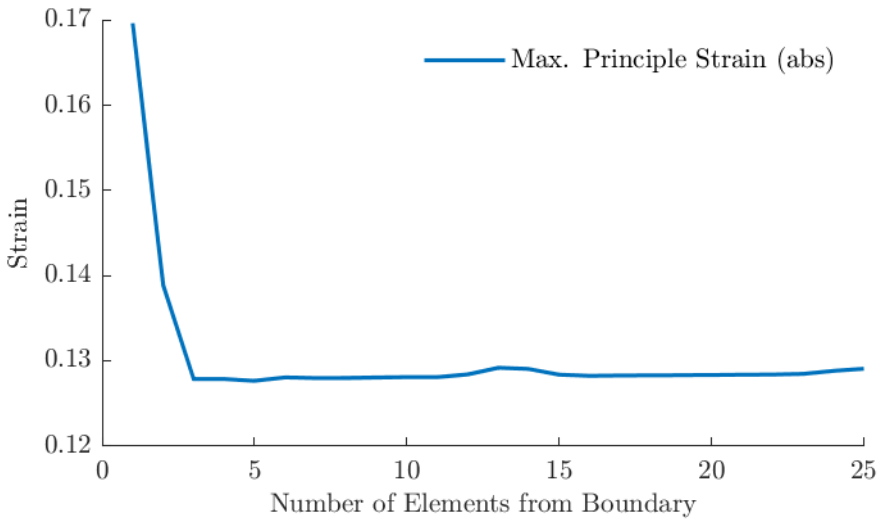

Figure 6.18: Number of elements from the edge of the local model undergoing excessive deformation due to the boundary effect

As seen in figure 6.19, the only manual steps for the user are to design the prototype on the TaniqWind software, choose the required RVE, and create the local model. All the remaining steps, including the complete automation of the global model input file creation, are automated using two MATLAB scripts. One script creates the fibre overlap pattern from the output files of TaniqWind, while the other automates the submodelling process.

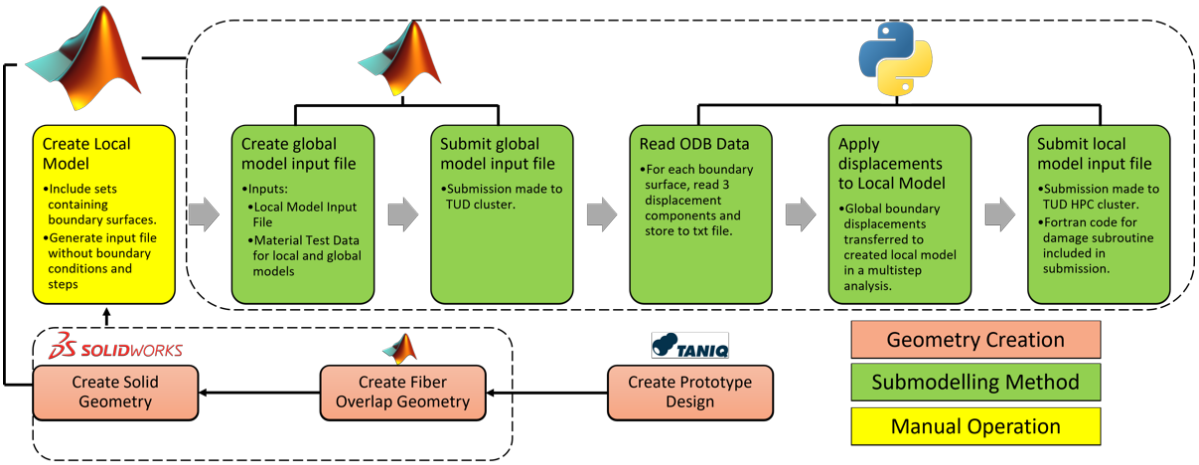

Figure 6.19: Automated submodel generation scheme

6.5. Conclusion

In this chapter, the creation of the FEA model was detailed. For capturing the global model displacement response, modelling the fibre winding pattern as a rebar layer was motivated as a suitable candidate. This was then compared against experimental data from literature to confirm its validity. The creation of the rebar layer was then detailed, in which the winding angles were assigned as a discrete property for each element. Finally, the rebar layer was placed in the solid rubber elements using embed constraints.

The local model was created with explicit modelling of the undulating fibres and the rubber, both with solid elements. Tie constraints were used at the rubber-fibre interface to model a perfectly bonded interface. Failure was introduced via element deletion for the fibre elements based on maximum axial strain criteria. This was achieved via the USDFLD user subroutine in ABAQUS.

Finally, a novel submodelling approach was introduced which allows the exact transfer of displacement boundary conditions from the global to the local model without the need for interpolation. This was achieved by embedding copies of the local model boundary as surface meshes in the local model and using its displacements as the boundary conditions for the local model. In this manner, the aberrations seen in the built-in ABAQUS submodelling tool were avoided. The entire submodelling process was automated via code to make the user interaction minimal.

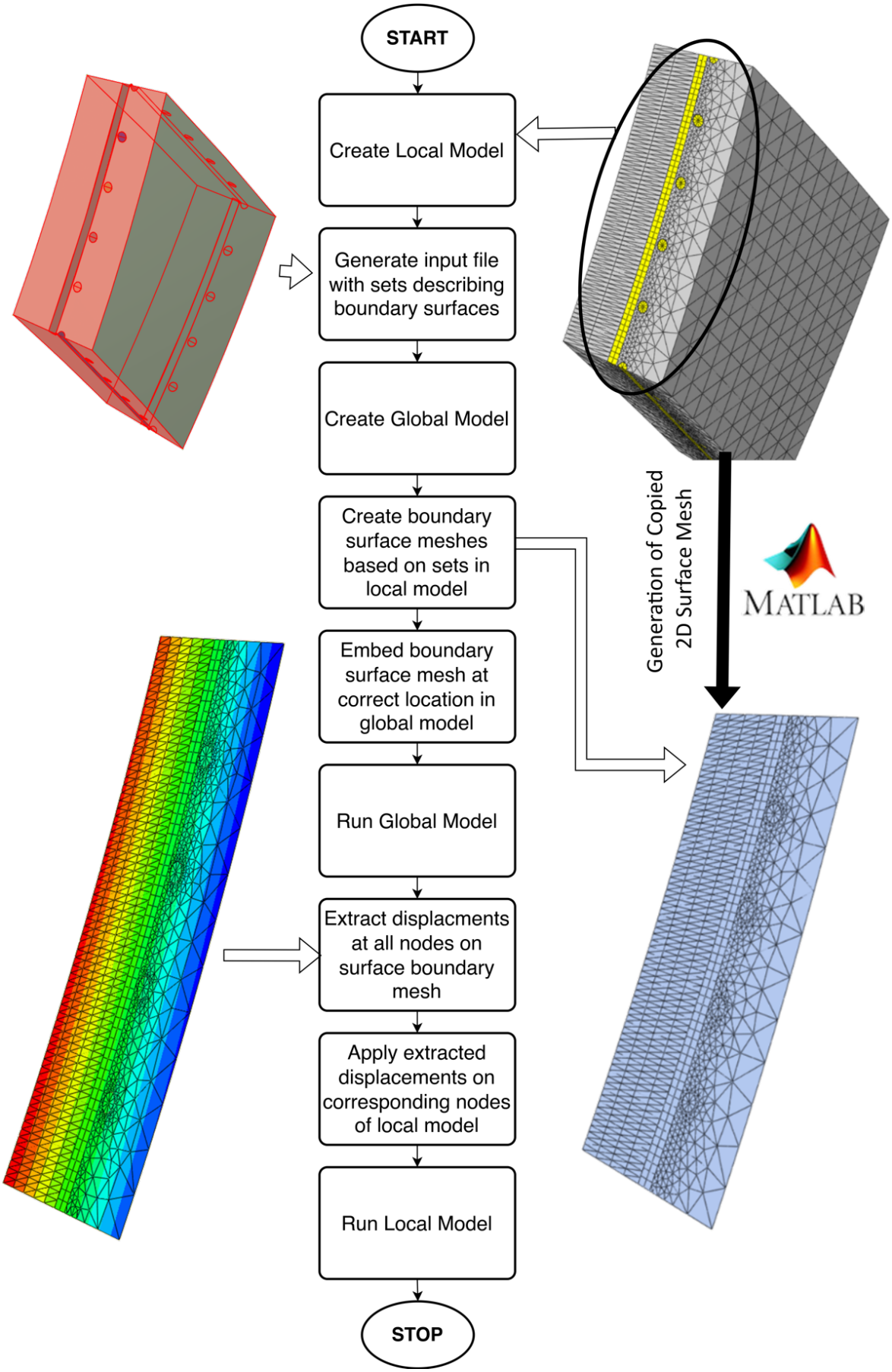

Figure 6.20: Submodelling Implementation

This page was intentionally left blank.

7

Results and Sensitivity Studies

In this chapter, the performance of the submodelling approach will be studied and compared against experimental data collected as a part of this project. Additionally, parametric studies to study the effect of certain parameters on the burst pressure of the CRC pressure vessel are presented.

7.1. Model Performance

Firstly, the results of the global and local models are each compared against experimental data obtained via burst tests conducted - see chapter 8 for details. Additionally, a mesh refinement study is provided for each model to showcase the convergence of the obtained solution.

7.1.1. Global Model Performance

For the global model, the displacement solution is the most important for transferring the correct boundary conditions to the local model. To validate this behaviour, burst tests for three samples were conducted using image-based data logging equipment designed for this project - see chapter 8. The maximum diameter and height of the product were then plotted against the internal pressure, and the resulting data was compared against similar data from the rebar global model.

The comparison between the maximum diameter and internal pressure is seen in figure 7.1a. In terms of displacement errors, an excellent correlation is seen, with a maximum deviation of 1.13% at lower pressures. A similar plot is seen in figure 7.1b for the comparison between experimental and global model flange-to-flange axial elongation. Again, excellent correlation is seen with the maximum deviation being 2.49% at pressures close to burst.

The slight deviation of the experimental data shape from that of the global model can be due to the following reasons:

1. The sampling rate of the experimental data may be too low at 2 Hz, which may lead to the non-linear response not being accurately captured.
2. The camera used for the image measurements did not have a linear field of view throughout. This affects the conversion from pixels to mm.
3. As seen in figure 8.16, the experimental prototype has no constraints on displacement at the top flange. This is in contrast to the global model, which allows the upper flange to only displace axially. Any imperfections in the prototype may cause the experiment to deviate from this idealisation, which will be reflected in the experimental data.

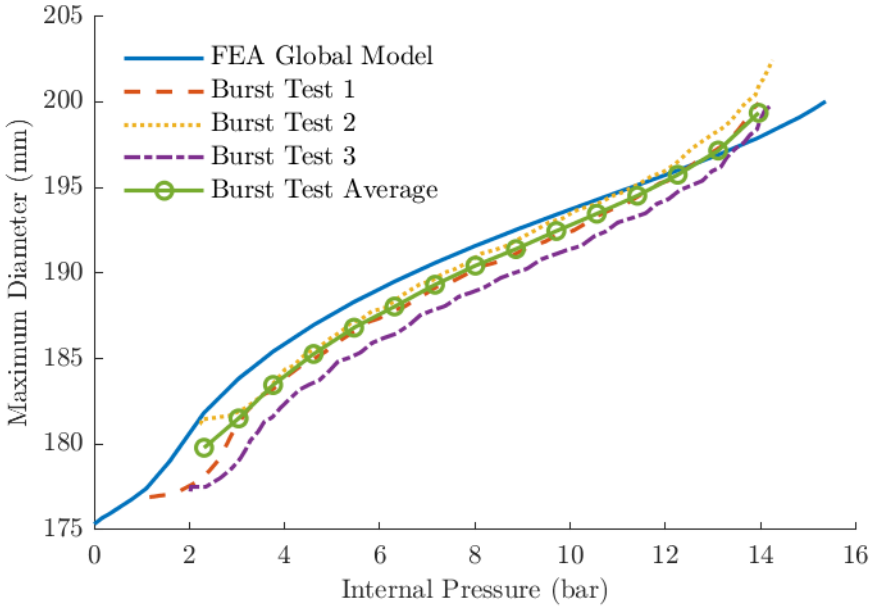

(a) Maximum diameter comparison

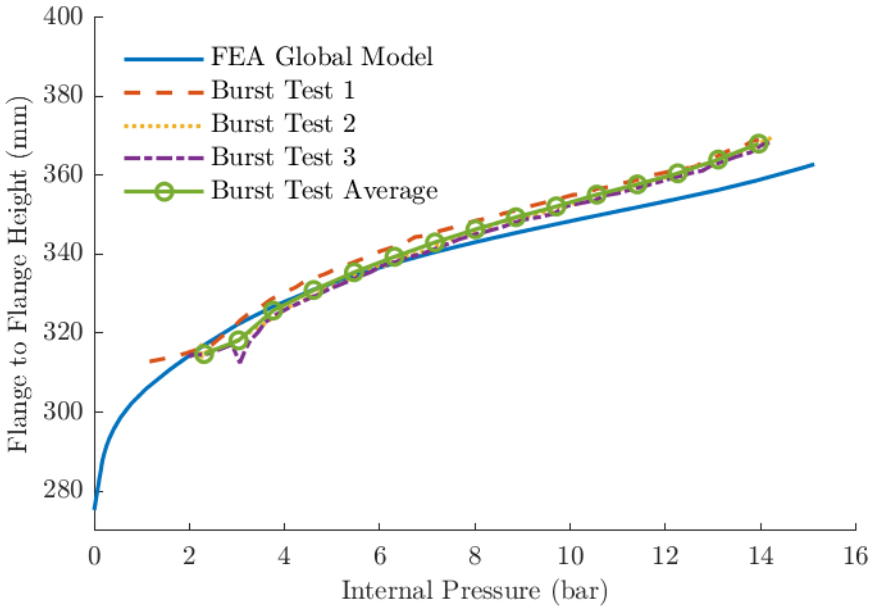

(b) Flange to flange height comparison

Figure 7.1: Comparison of experimental displacements with FEA global rebar model

4. Due to equipment limitations, it was not possible to have an even rate of pressurisation in the experimental data. Thus, some dynamic effects may influence the data collected.

Thus, it can be shown that the rebar model is able to capture the global displacements with sufficient fidelity to serve as the boundary conditions for the local model.

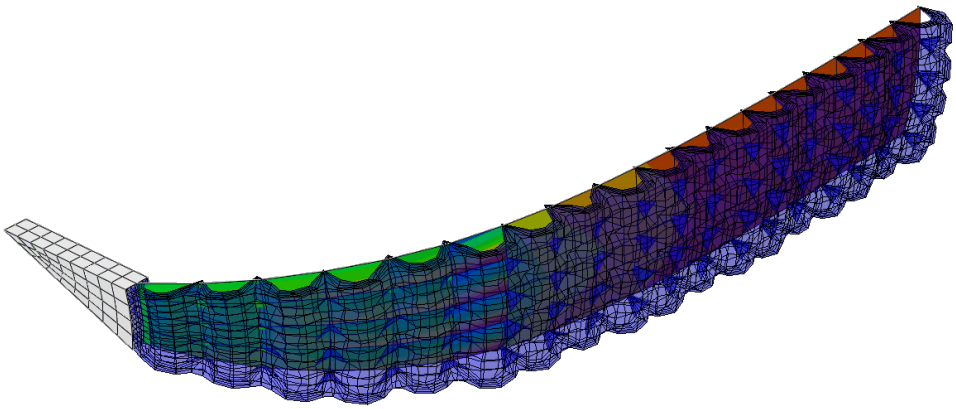

Figure 7.2: Effect of rebar mesh being coarser than rubber mesh

7.1.2. Global Model Mesh Convergence

To check the convergence of the obtained solution, a mesh study was conducted by altering the rebar mesh size and checking the maximum and minimum displacements on the embedded boundary surface mesh - see table 7.1. It can be observed that as expected, there is a rapid convergence of the displacement solution. However, to allow the embed constraint to work as expected, the rebar element needed to be smaller than the rubber element it is embedded in - see figure 7.2. It was decided to have a fairly fine rebar mesh to allow accurate interpolation of the fibre winding angles at the dome region.

Number of Rebar Elements	% Change	Min. Displacement	% Change	Max. Displacement	% Change
560.00	1355.18	12.01	0.25	13.64	0.22
8149.00		12.04		13.67	

Table 7.1: Global Model Convergence

7.1.3. Local Model Performance

The burst pressure prediction made by the local model is discussed in this section. The local model, as described in section 6.2, was modelled allowing progressive fibre failure using the maximum axial strain failure criteria. At this stage, perfect bonding between the interface and fibre is assumed throughout the analysis.

Figure 7.3 shows the progression of fibre failure in the local model. Initially, stress peaks are formed near the fibre overlap regions due to local restrictions on deformation - see figure 7.3a. Here, a kinked fibre is unable to straighten out under the applied load due to the presence of a fibre under it, thus causing stress concentrations on both the participating fibres. Once the fibre elements in this overlap region reach the critical axial strain, they fail, causing a local stress drop - see figure 7.3b. Finally, the failure of some fibres causes accelerated loading of the other fibres, leading to a near-simultaneous failure of multiple fibres.

It must be kept in mind that first-fibre failure in the RVE doesn't imply the failure of the first fibre in the product as a whole. Rather, it may be treated as a representative simultaneous failure of $1/n^{th}$ of all the fibres in the cylindrical region, where n is the number of non-boundary fibres in the local model. In this case, due to the presence of 8 non-boundary fibres in the model, the failure of one fibre represents a failure of 12.5% of the fibres in the model. Due to this, it is apt to define failure by the load at which there is a complete cross-sectional failure of the first fibre in the local model. In reality, the choice of failure criteria has little impact on the burst pressure prediction as a near-simultaneous failure of most of the fibres is seen in the local model after the failure of the first fibre - see figure 7.3c.

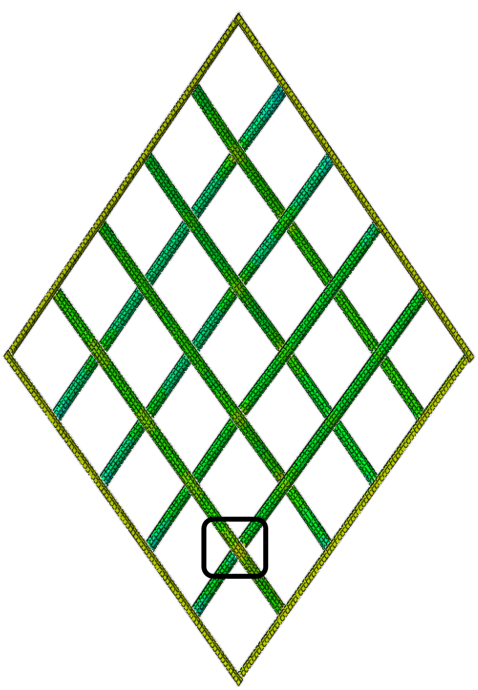

(a) Initial strain concentrations at overlap zones

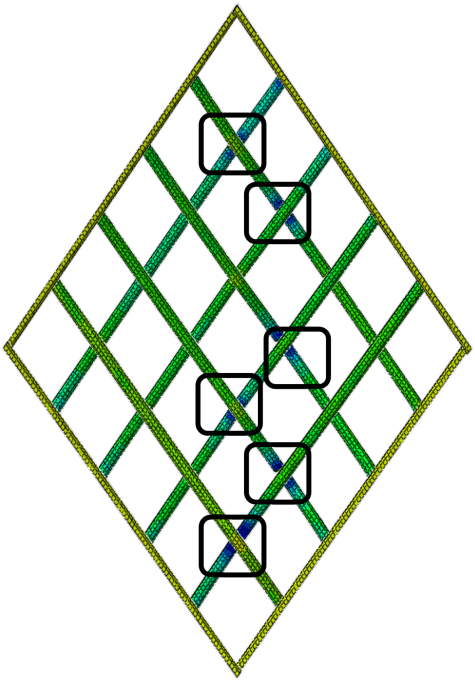

(b) Near-simultaneous fiber failure initiation

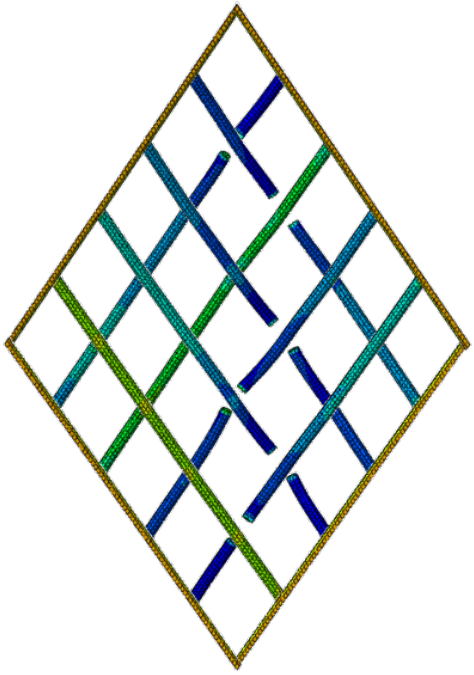

(c) Complete fiber failure

Figure 7.3: Local model fibre damage sequence

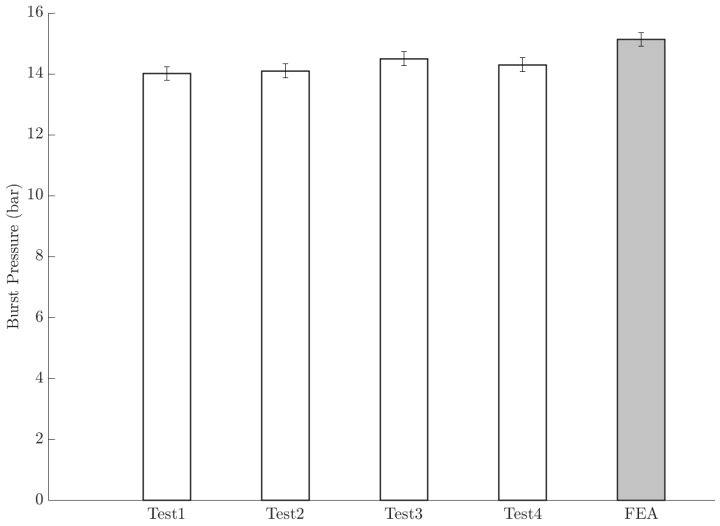

Figure 7.4: Comparison of experimental and FEA burst pressures

To check the accuracy of the solution, the burst pressure obtained using the FEA model was compared against failure pressures from experimental burst tests. Figure 7.4 shows the experimental burst pressures of four CRC prototypes, having an average burst pressure of 14.23 bar. In comparison, the FEA model predicts the burst pressure to be 15.13 bar.

This error of 6.3% is already an acceptable solution within engineering precision. The over-prediction of the burst pressure may be due to:

- Non-inclusion of structural softening due to interface damage.
- Assumption of an isotropic material model for the twisted cord that is inherently much softer in the transverse direction.

7.1.4. Local Model Mesh Convergence

A similar mesh convergence study was carried out for the local model. Here, the number of circumferential and axial seeds was proportionately increased, thus increasing the size of the fibre mesh. Once again, as seen in table 7.2, rapid convergence is seen.

Fiber Circumferential Seed	Number of Fiber Elements	% Change	Burst Pressure	% Change
6	2592	-	15.92	-
8	3456	33.33	15.44	3.02
10	4320	25.00	15.18	1.68
12	7776	80.00	15.13	0.33

Table 7.2: Local Model Convergence

7.2. Parametric Studies

An advantage of building the FEA model and validating its accuracy is that it may be then used for conducting parametric studies to ascertain the sensitivity of various design aspects on product performance. In this section, the sensitivity of the burst pressure to the rubber thickness, the fibre winding angle, and the overlap pattern will be studied.

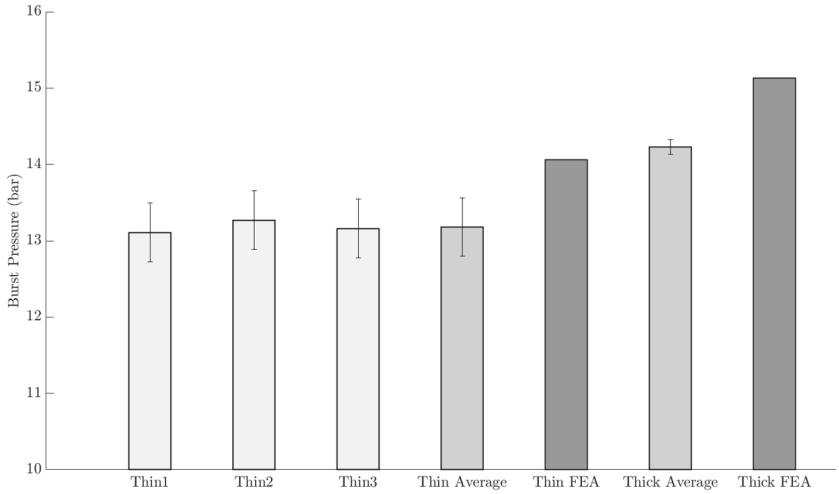

Figure 7.5: Comparision of burst pressures for thick and thin samples - both FEA and experimental

7.2.1. Effect of Rubber Thickness

It is often assumed that in CRC structures, the fibres are responsible for bearing all load due to the compliant nature of the rubber. This leads to simplistic estimations, such as netting analyses, to be widely used within the industry to analyse product failure. In this section, a study is made using two sets of prototypes with the same fibre pattern, but different rubber thicknesses to ascertain the effect of the rubber layer on the burst pressure.

	Design 1	**Design 2**	**% Change**
Mass (g)	1157.96	1051.43	8.45
Average Thickness (mm)	5.89	5.44	

Table 7.3: Prototype designs used for study

Table 7.3 shows the average dimensions of the study specimen chosen for the study. Burst tests were conducted for three specimens of the thinner design, and the results were compared against the average data from the thicker specimens seen in figure 7.4. The results are seen in figure 7.5. An average change of $\approx 8.5\%$ in rubber thickness leads to a proportional increase in burst pressure of $\approx 8\%$. Although not a surprising result, the following important conclusions may be drawn:

1. CRC products are often of sizeable thickness. This means that the thickness itself often contributes to the product stiffness geometrically, even if the matrix material stiffness itself is very low.
2. With relatively small changes in thicknesses, such as in this study, a nearly linear change in percentage burst pressure may be expected with a change in percentage thickness.

Another noteworthy result seen in figure 7.5 is the relative differences in the FEA and experimental results for both the thin and thick samples. The percentage difference for both is very similar, with a difference of $\approx 6.3\%$ for the thick specimen and $\approx 6.6\%$ for the thin specimen. This agreement in deviation validates that the model is working consistently and predictably.

7.2.2. Effect of Winding Angle

To validate the ability of the model to capture relevant physical phenomena during deformation, an additional winding angle of $\alpha = 45°$ was chosen. Until now, the geodesic angle ($\alpha_g \approx 54.74°$) used for this project allowed minimal fibre reorientation. Any fibre winding pattern whose angle deviates

from this angle will experience fibre reorientation upon loading such that it tends towards the geodesic winding angle. This section aims to compare the expected behaviour of such a winding angle with the model prediction. Three parameters, namely fibre scissoring, model deformation and predicted burst pressures are studied. No comparison is made with experimental data due to constraints on time and project costs.

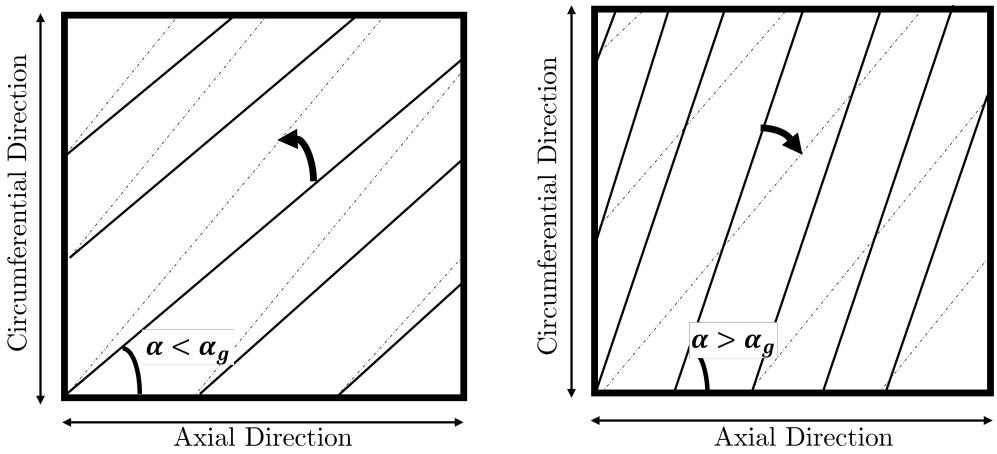

(a) Winding angle less than geodesic angle **(b)** Winding angle more than geodesic angle

Figure 7.6: Fiber scissoring directions for non-geodesic winding. The dotted lines indicate the geodesic winding angle of $\alpha_g \approx 54.74°$

Fiber Scissoring

The fibre scissoring behaviour was studied for both the local and the global models. In figure 7.7, it can be seen that on pressurising the sample, there is a rapid reorientation of the fibres towards $\alpha = \alpha_g$. During this period, the fibre strains are comparatively low, with most of the deformation being rigid body rotation. Once the fibres are reoriented, they rapidly take up load, seen in the sudden change in the slope of the strain curve at around 1.5 bar.

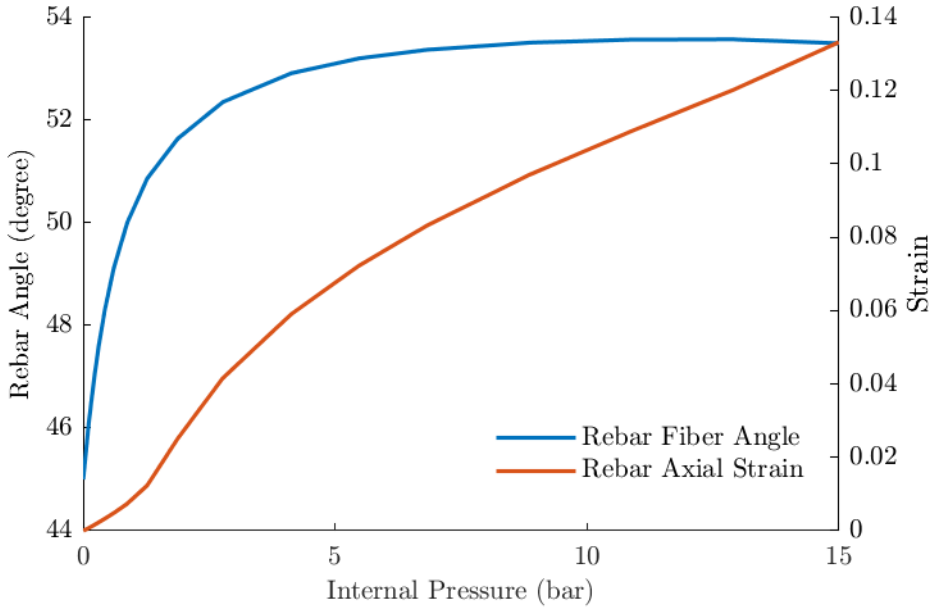

Figure 7.7: Variation of global model fibre winding angles and strains with pressure in the cylindrical region.

A similar reorientation can also be seen in the local model. Here, the angle is measured using the 2D projected image of the fibres as seen in

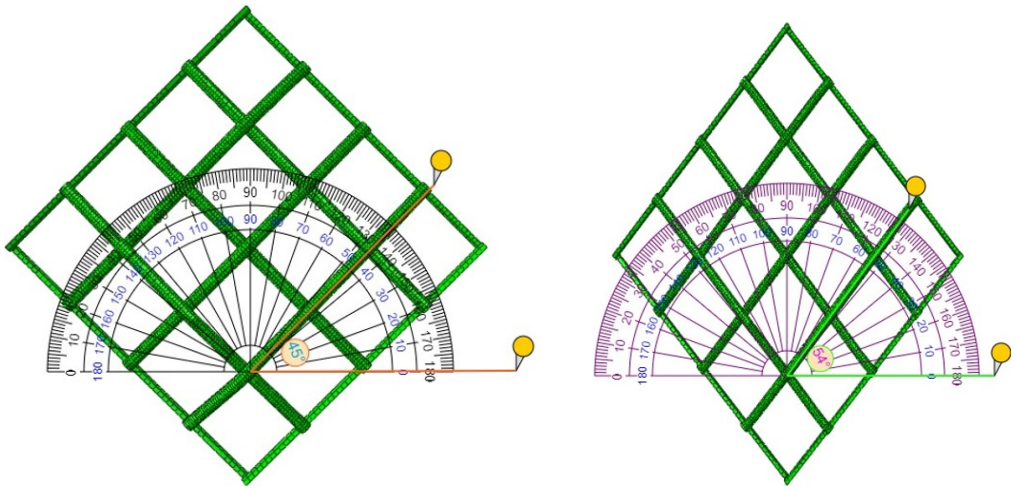

(a) Pre-deformation **(b)** Post-deformation

Figure 7.8: Fiber scissoring in local model

Deformation

The deformation tendencies of patterns deviating from the geodesic pattern can be explained with the help of figure 7.6. For angles less than the geodesic angles (figure 7.6a), there is an anticlockwise rotation of the fibres (in the illustrated reference frame) towards $\alpha = \alpha_g$. This means that under pressure, perfectly rigid fibres would undergo pure rotation leading to axial shortening and diametrical bulging of the structure. The exact opposite is seen in angles greater than the geodesic angles (figure 7.6b). Here, contraction of the winding angle under pressurisation leads to axial lengthening and diametrical compaction of the structure.

For comparison, axial and diametrical displacement readings can be taken from the global models of the 45° and the 54.74° models - see table 7.4.

	Axial Elongation (mm)	**Diametrical Expansion (mm)**
45.00° Model	21.99	27.39
54.74° Model	43.53	12.03
Change (%)	-49.47	+127.72

Table 7.4: Deformation comparison between 45° model and 54.74° model

Here, the trends of increasing diametrical displacement and lower axial elongation are clearly seen. An important observation is that in both cases, axial elongation is seen. With reference to figure 7.6a, one may assume there to be axial shortening. However, this prediction is valid only if the cords are perfectly rigid. In reality, the cords themselves undergo stretching which may contribute to the dimensional changes of the sample. This is especially true for the chosen nylon cords, which are known to undergo large deformations.

Burst Pressure

It can be theorised that if all production and design parameters other than the winding angle are held constant, then the burst pressure of the specimen is directly related to the surface area of the inner wall on which the pressure acts. The higher the internal surface area for a given pressure, the larger the force on the structure, and thus the greater the load in each fibre. Thus, winding angles that create the lowest surface area with increasing load will have the highest burst pressure.

	Burst Pressure
45° Model	15.13
54.74° Model	12.92
Change (%)	-17.11

Table 7.5: Burst pressure comparison between 45° and 54.74° sample

For $\alpha < \alpha_g$, there is a tendency for the product to expand radially and constrict axially as explained earlier. However, the surface area is proportional to r^2, and thus, for angles lower than the geodesic angle, an increase in internal surface area is to be expected, leading to lower burst pressures. This is observed in table 7.5 for the $\alpha - 45°$ winding angle. Conversely, on the other side of α_g, the diameters tend to reduce on pressurising, which may indicate an increase in burst pressures.

7.2.3. Effect of Overlap Pattern

Up until now, the discussion relating to modelling the overlap pattern has been purely theoretical, with the motivation to do so mainly sourced from literature - see section 3.2. However, with the development of the model, a direct comparison can be made between the burst pressures of a model with and without a fibre overlap pattern.

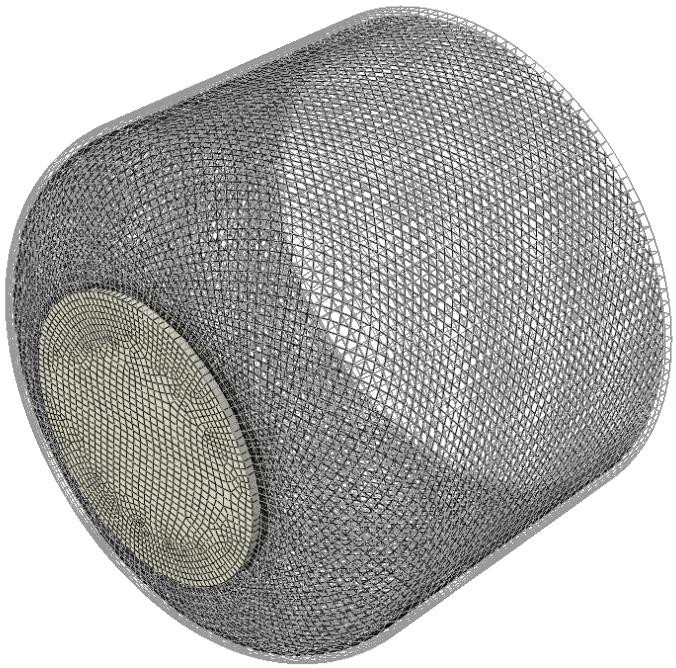

Figure 7.9: Half CRC model (axial Symmetry) without fibre overlap using truss elements. Rubber elements are made transparent here to highlight the fibre layer.

For the model without an overlapping pattern, a truss network was used to model the fibre layer, which was then embedded into the solid rubber elements using embed constraints. The advantage of the truss model is that:

- It can carry load only in the axial direction, which is the only direction in which material data is available.
- Based on the truss mesh size, the winding path can be very closely replicated.
- If the winding pattern is known, the connectivity matrix for the fibre layer can be very easily scripted.

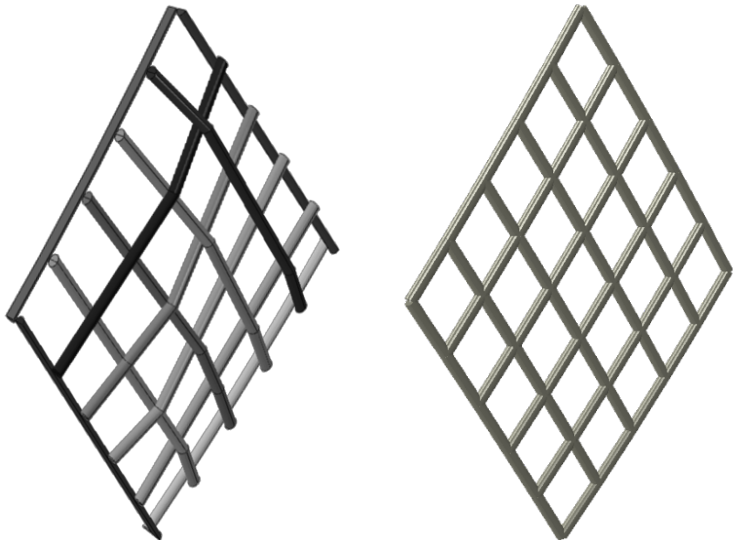

(a) Rhombus with overlap pattern

(b) Rhombus without overlap pattern

Figure 7.10: Comparison of fibre RVE with and without overlap

Figure 7.9 shows the developed truss model. Here, instead of fibre overlaps, intersecting fibres share a common node at the intersection point - see figure 7.10. Similar material models as described in chapter 5 were used for the truss model too. Figure 7.11 shows the comparison between the FEA models with and without fibre overlap. While the overlap model over-predicted the burst pressure by $\approx 6.3\%$, the truss model over-predicts the solution by $\approx 26.7\%$. This validates the need to model the fibre overlap geometry to obtain accurate stress states in filament wound rubber structures.

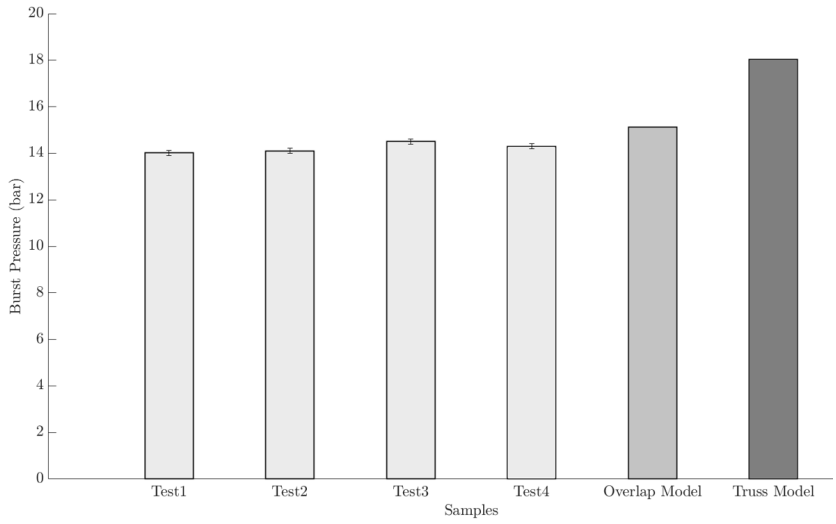

Figure 7.11: Comparison of experimental burst pressure data with FEA model burst pressures with and without overlap

7.3. Conclusion

In this chapter, the performance of the submodelling approach was evaluated against experimental data. First, the global model solution was compared against axial and diametrical displacements of experimental specimens, for which a maximum error of 1.13% and 2.49% respectively was seen. The local model burst pressure prediction was then compared to the burst pressures of the same experimental

specimens, where an over-prediction of 6.3% was seen. This error percentage ($\approx 6\% - 7\%$) was fairly consistent even when compared against experimental prototypes with a differing rubber thickness, thus validating that the model captures the basic physics of the CRC prototype.

Following the experimental validation, parametric studies were carried out to study the effect of the rubber thickness, fibre winding angle and fibre overlap on the burst pressure predictions of the model. It was noticed that due to the thick wall of the CRC prototypes, the rubber wall thickness plays a geometric role in increasing its burst pressure. This percentage increase in burst pressure is roughly linear with increasing percentage wall thickness.

The effect of fibre winding was studied by using the submodelling approach to build a model with $\alpha = 45deg$. Since this bias angle is lower than the geodesic angle, it was predicted that this model would undergo larger diametrical and lower axial deformation. Additionally, lower burst pressures were expected due to this higher deformation. The created submodelling tool was able to validate these predictions, and thus prove that it captures the main highlights of the deformation process.

Finally, the effect of fibre overlap was studied by creating a model in which the fibre pattern was represented by linear truss elements. Instead of overlapping, the fibres cross each other and share a common node at their point of intersection. A difference of $\approx 26.7\%$ was seen between the experimental and truss model, compared to the $\approx 6.3\%$ for the overlap model. This validated the need to model the fibre overlap pattern created by the filament winding process.

This page was intentionally left blank.

8

Experimental Campaign

8.1. Rubber Characterisation

The experimental procedures required to fit a hyperelastic material model for the rubber are described in this section. The calibration of the material model depends on a state of homogeneous deformation [84] in the rubber, and thus special samples need to be made that adhere to this requirement, at least in the region of interest. The three main deformation modes - uniaxial tension, uniaxial compression, and simple shear are experimentally tested independently. Due to equipment limitations, these tests were outsourced to Axel Testing Inc, USA. All tests were done under slow cyclic loading (SCL) at a strain rate of $0.01s^{-1}$.

8.1.1. Uniaxial Tension Test

The ASTM D412 standard [111], a popular choice for the uniaxial tensile testing of vulcanised rubbers, was used for the tensile characterisation of the rubber specimens. Dumbbell specimens were used with their length being more than ten times their width to allow a state of homogeneous deformation in the neck region. A non-contact extensometer was used along with tracker - tabs on the rubber specimen to prevent influencing the test data. The specimens, as used, are seen in figure 8.1.

The strain state in the dumbbell region can be approximated as follows, where λ_i and t_i are the principle stretch and developed traction in the i$^{\text{th}}$ direction respectively.

$$\begin{aligned} \lambda_1 &= \lambda_A \\ \therefore t_2 &= t_3 = 0 \\ \therefore \quad \lambda_2 &= \lambda_3 = \lambda_T \end{aligned}$$

Due to incompressibility, there can be no volume change.

$$\begin{aligned} \therefore \quad \lambda_1\lambda_2\lambda_3 &= 1 \\ \therefore \quad \lambda_A \cdot {\lambda_T}^2 &= 1 \\ \therefore \quad \lambda_T &= 1/\sqrt{\lambda_A} \end{aligned}$$

Then,

$$\Psi(\lambda) = \Psi\left(\lambda, \lambda^{-\frac{1}{2}}\right)$$

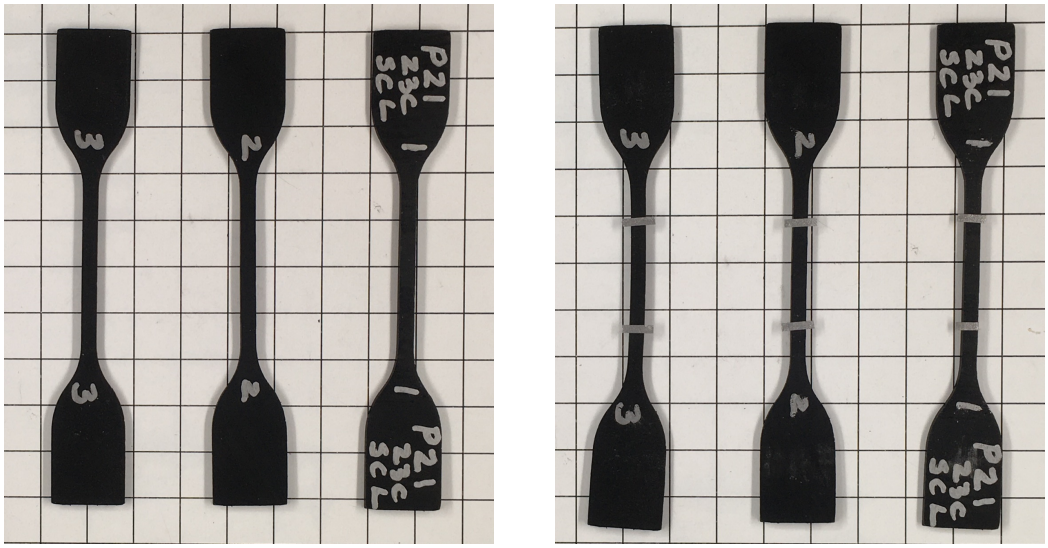

(a) Pre-test **(b)** Post-test

Figure 8.1: Dumbbell specimens used for uniaxial tensile tests.

Then, the engineering stress-stretch curve can be fit to the strain energy functional - Ψ expressed in the following form:

$$t = \frac{d\Psi(\lambda)}{d\lambda}$$

Three samples each were tested cyclically through three strain targets - 60%, 100% and 250% for five cycles each. The collected experimental data is seen in figure 8.2. A stark difference is seen between the initial loading cycle and the remaining cycles. This can be attributed to the Mullin's effect [26], where rubber suffers irreversible softening post initial loading cycles. This response quickly stabilises to form a hysteresis loop, whose loading curve can be then used to define the material response.

8.1.2. Equibiaxial Tension Test

The equibiaxial tension test is performed by imposing equal strains along the two planar directions of a rubber specimen. Apart from simulating a specimen under equibiaxial loading, this test also simulates a specimen under uniaxial compression in the following manner due to the assumption of perfect incompressibility:

$$\lambda_2 = \lambda_3 = \lambda_B$$

Due to incompressibility:

$$\lambda_1 \lambda_2 \lambda_3 = 1$$

$$\lambda_1 \cdot {\lambda_B}^2 = 1$$

$$\therefore \quad \lambda_1 = 1/{\lambda_B}^2$$

Then, the deformation gradient for equibiaxial tension (F_B) can be expressed as:

$$F_B = \begin{bmatrix} 1/{\lambda_B}^2 & 0 & 0 \\ 0 & \lambda_B & 0 \\ 0 & 0 & \lambda_B \end{bmatrix}$$

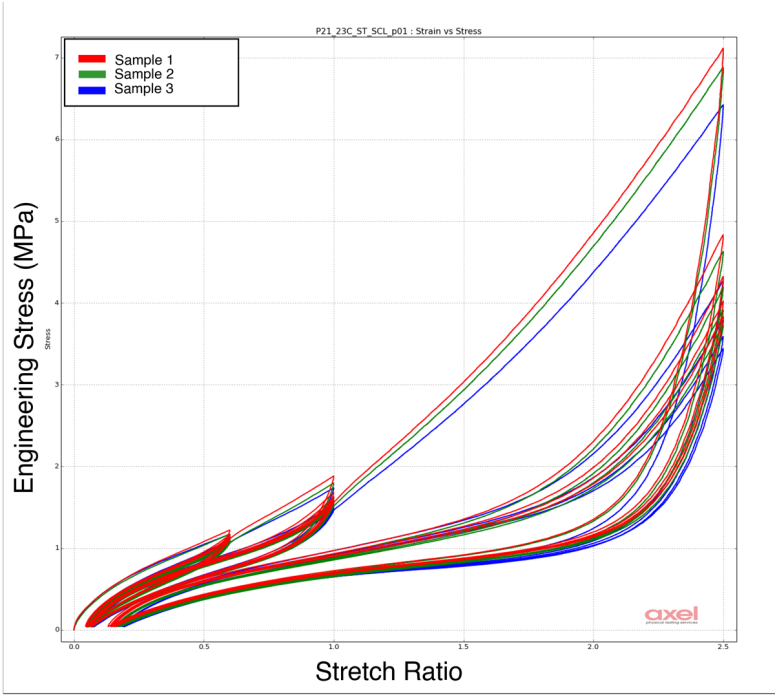

Figure 8.2: Uniaxial tensile test data for rubber specimen

Similarly, for uniaxial compression:

$$F_{UC} = \begin{bmatrix} \lambda c & 0 & 0 \\ 0 & 1/\sqrt{\lambda c} & 0 \\ 0 & 0 & 1/\sqrt{\lambda c} \end{bmatrix}$$

In the limit $\lambda_B = \sqrt{2}$ and $\lambda_c = 0.5$:

$$F_B = F_{UC} = \begin{bmatrix} 0.5 & 0 & 0 \\ 0 & \sqrt{2} & 0 \\ 0 & 0 & \sqrt{2} \end{bmatrix}$$

The stresses can then be computed for uniaxial compression as:

$$\sigma_{UC} = \begin{bmatrix} \sigma_C & 0 & 0 \\ 0 & 0 & 0 \\ 0 & 0 & 0 \end{bmatrix}$$

And for equibiaxial compression as:

$$\sigma_{EB} = \begin{bmatrix} 0 & 0 & 0 \\ 0 & \sigma_B & 0 \\ 0 & 0 & \sigma_B \end{bmatrix}$$

Separating the indeterminate pressure stresses yields:

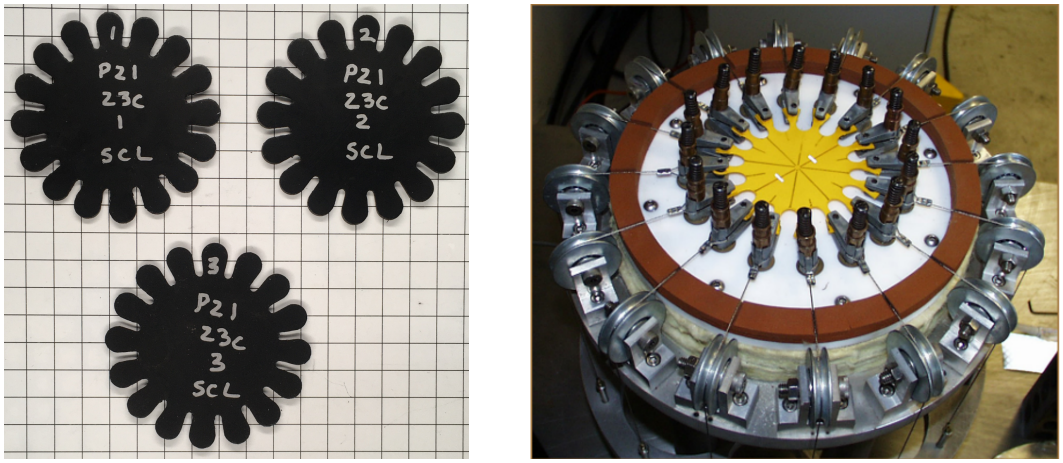

(a) Circular test specimen **(b)** Test setup

Figure 8.3: Specimens and machinery used for equibiaxial tension test

$$\sigma_{EB} = \begin{bmatrix} -\sigma_B & 0 & 0 \\ 0 & 0 & 0 \\ 0 & 0 & 0 \end{bmatrix} + p\mathbf{I}$$

Thus, for perfectly incompressible rubbers, the deformation state is identical for uniaxial compression and equibiaxial tension within the given stretch limits. The stress has equal magnitude, but opposite sign.

The equibiaxial tensile test is conducted using circular disks as shown in figure 8.3. The samples are strained radially via multiple cable bearing systems, which creates a region of equibiaxial tensile strain in the centre of the sample irrespective of thickness or radial position [112]. Keeping in mind the strain limits, three samples were tested cyclically through two strain targets - 60% and 100% for five cycles each. However, data from sample 2 was not complete due to the premature failure of the radial tabs. The collected experimental data is seen in figure 8.2.

8.1.3. Planar Tension Test

Simple shear tests can be used to determine the shear response of the material as shown in figure 8.5a. However, such a test strongly depends on a strong bond between the rubber and the grip which is not always possible. A common alternative is to use a state of pure shear via a planar tension test - see figure 8.5b. In such a test, a planar sample is used in which the width is much larger than its length - see figure 8.6.

It can be proven that a state of pure shear lies along the diagonal of a planar tension specimen in the following way:

For an incompressible material under pure shear, the deformation gradient (F_{PS}) may be written as [14]:

$$F_{PS} = \begin{bmatrix} 1/\left(1-\lambda_s^2\right) & 0 & 0 \\ 0 & 1 & \lambda_s \\ 0 & \lambda_s & 1 \end{bmatrix}$$

Here, the factor $1/(1-\lambda_s^2)$ is introduced to ensure that $\det(F) = 1$ to preserve volume.

Now, for a state of planar tension, the deformation gradient (F_{PT}) can be expressed as:

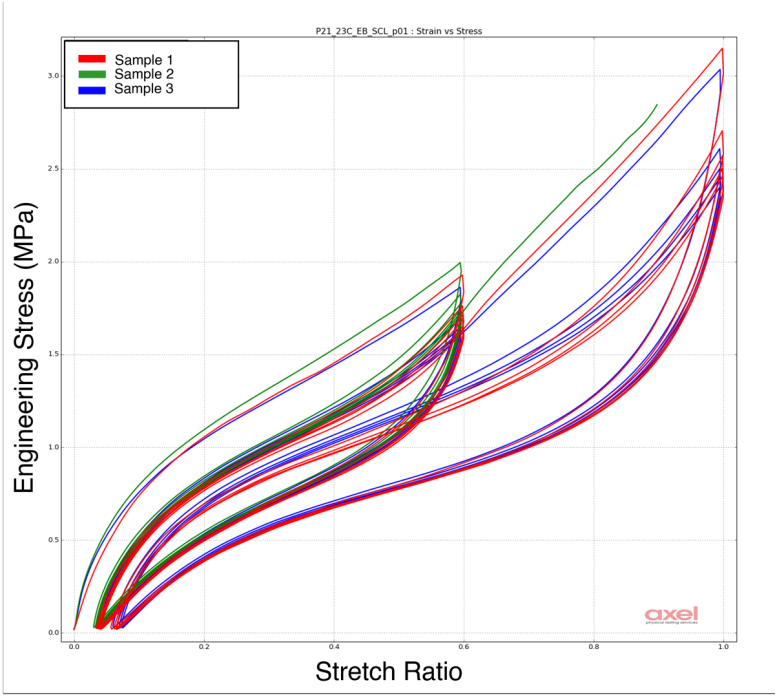

Figure 8.4: Equibiaxial tensile test data for rubber specimen

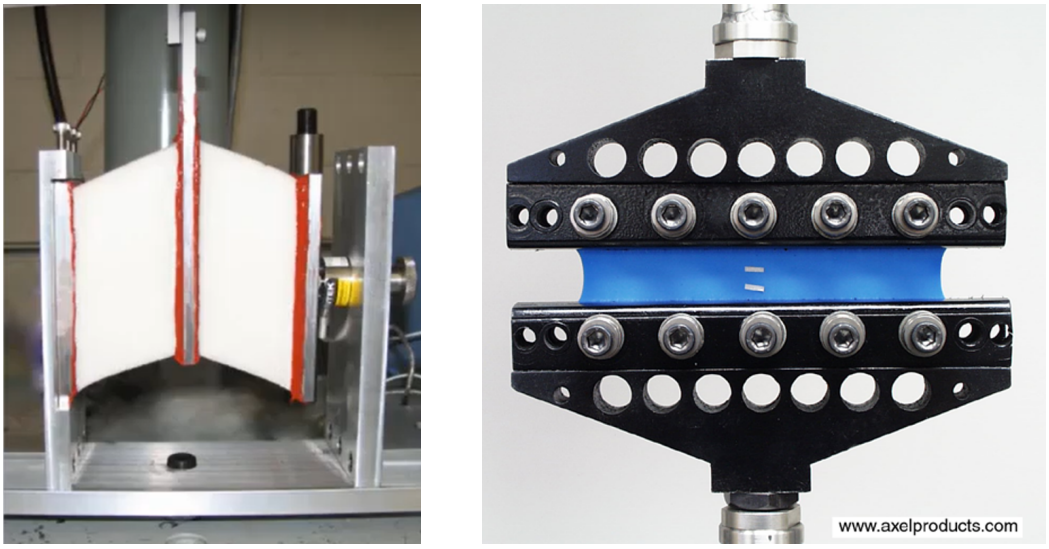

(a) Simple shear test **(b)** Planar tension test

Figure 8.5: Methods to test the shear response of elastomers [12]

$$\lambda_1 = \lambda_s$$
$$\lambda_2 = 1$$

$\therefore$ By the incompressibility constraint:

$$\lambda_3 = {}^1/_{\lambda_s}$$

$$\therefore F_{PT} = \begin{bmatrix} 1 & 0 & 0 \\ 0 & 1+\lambda_s & 0 \\ 0 & 0 & 1/(1+\lambda_s) \end{bmatrix}$$

If F_{PT} is rotated by 45° to align along the diagonal, then:

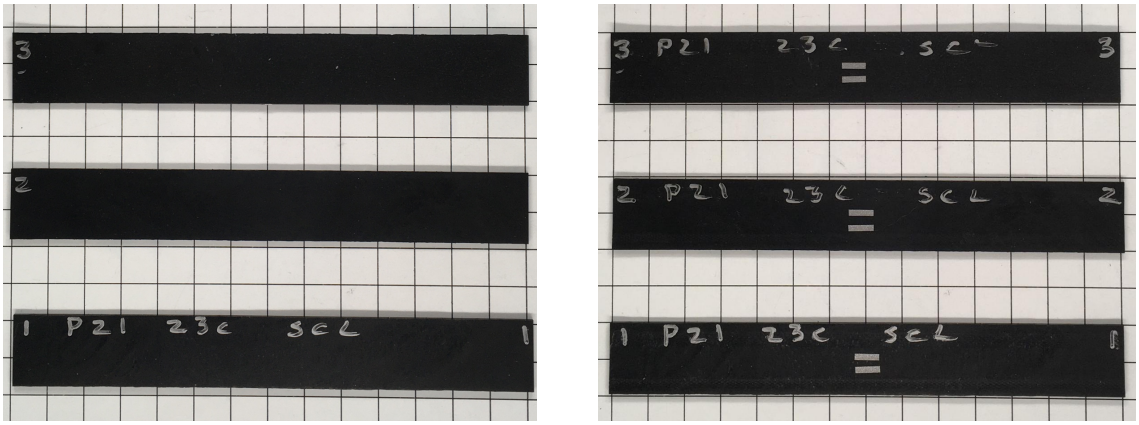

(a) Pre-test **(b)** Post-test

Figure 8.6: Wide specimens used for planar tension tests.

$$F_{PT} = Q^{\top} \begin{bmatrix} 1 & 0 & 0 \\ 0 & 1+\lambda_s & 0 \\ 0 & 0 & 1/(1+\lambda_s) \end{bmatrix} \cdot Q$$

Where;

$$Q = \begin{bmatrix} 1 & 0 & 0 \\ 0 & \cos 45° & \sin 45° \\ 0 & -\sin 45° & \cos 45° \end{bmatrix}$$

Simplifying for small strain and imposing incompressibility leads to:

$$F_{PT} = \begin{bmatrix} 1+\Delta & 0 & 0 \\ 0 & 1+\mathcal{O}\left(\lambda_s^2\right) & \lambda_s - \mathcal{O}\left(\lambda_s^2\right) \\ 0 & \lambda_s - \mathcal{O}\left(\lambda_s^2\right) & 1+O\left(\lambda^2\right) \end{bmatrix}$$

Where Δ is a minor term added to ensure $\det(F) = 1$. If the higher-order terms are neglected then,

$$F_{PT} = F_{SS} = Q^{\top} \begin{bmatrix} 1 & 0 & 0 \\ 0 & 1+\lambda_s & 0 \\ 0 & 0 & 1/(1+\lambda_s) \end{bmatrix} \cdot Q$$

Thus, for $\lambda_s \ll 1$, the deformation state along the diagonal of the planar tension specimen is the same as pure shear. Practically, this limit can be as low as $\lambda_s = 0.4$ as seen in figure 8.7.

The results for the planar tension test are seen in figure 8.8. Three samples were tested cyclically through three strain targets - 45%, 60% and 100% for five cycles each. It is very evident in the test data that a general 'up-turn' is seen in the data post $\approx \lambda_s = 0.45$ similar to that seen for the planar tension theoretical prediction in figure 8.7. This proves that data from the planar tension test should only be used in the approximate limit $\lambda_s < 0.45$.

8.2. Fiber Characterisation

The fibre used for this project was a 1880/2 110Z polyamide-66 twisted cord. This means that the cord construction consists of two fibre bundles twisted together in an anticlockwise manner with 110 twists per meter. The cord construction weighs 1880 g/km. This section elaborates on the tensile tests and fibre measurements used to calibrate the hyperelastic Marlow material model for the FEA model.

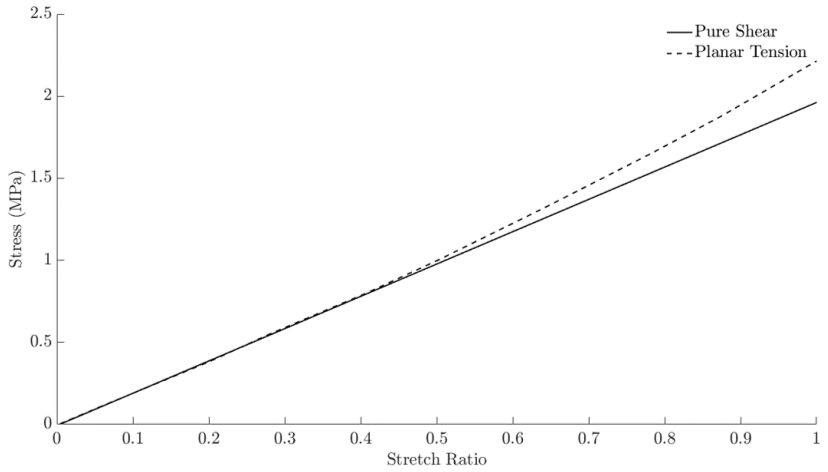

Figure 8.7: Comparison of diagonal stresses in planar tension specimen and stresses in a specimen under pure shear

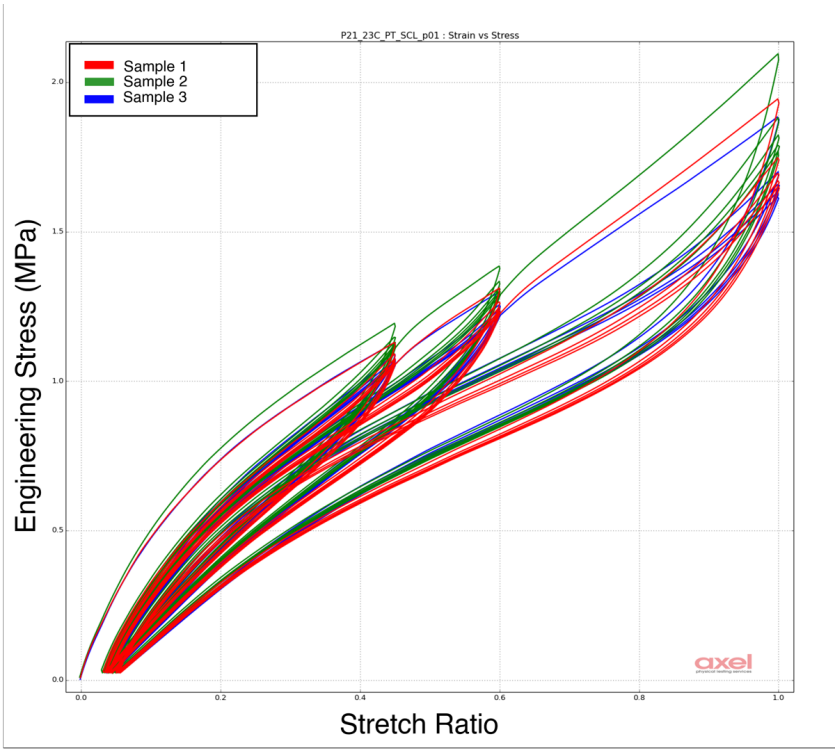

Figure 8.8: Planar tension test data for rubber specimen

8.2.1. Fiber Tensile Tests

The tensile fibre tests were performed on the 250 kN Zwick Roell test bench at the faculty of Aerospace Engineering, TU Delft. Despite the low failure load of a single fibre, the high-capacity test bench was solely used due to its integrated high-accuracy contact extensometer. ASTM-D885/D885M [113], a standard specific to the tensile characterisation of coated cords for placement in rubber, was used to define the parameters for the tests. Standard spiral grips - see figure 8.9 were used to avoid concentrating load near the clamped ends.

Two parameters were tracked during the experiments: the load-displacement response and the breaking load. Due to the risk of damaging the extensometer, it was disconnected just before fibre failure. The fibre failure strains were then computed using the failure loads and the calibrated Marlow material

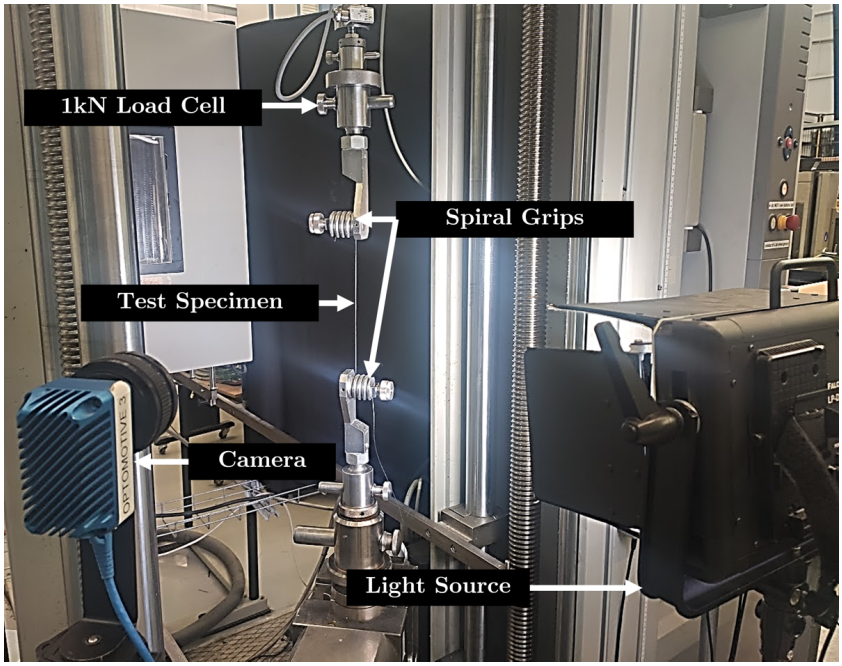

Figure 8.9: Fiber tensile test setup - extensometer removed

model. The fibre failure strains were already documented in figure 6.12. The raw experimental data is seen in figure 8.10.

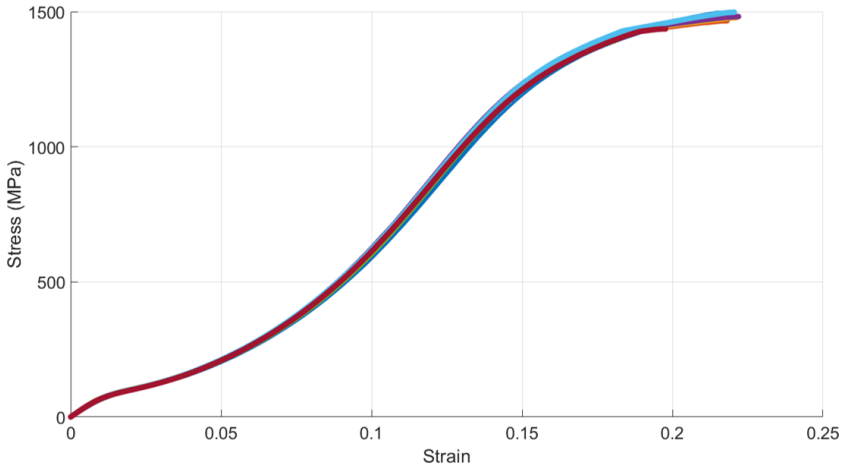

Figure 8.10: Nominal stress-strain data of 7 fibre specimen with extensometer

8.2.2. Fiber Cross Sectional Measurements

To calculate the average nominal tensile stress for the fibre, a measurement of their initial cross-sectional area is needed. To calculate the same, it was assumed that the fibre has a perfectly circular cross-section, and thus the diameter measurement was sufficient to calibrate the fibre cross-section.

Twenty fibre diameter measurements were taken over a 2 m sample of the cord at equal intervals. A micrometre screw gauge was used for the measurements, with a standard 'single-click' protocol used to determine its clamping force. The measurements are seen in figure 8.11, with an average diameter of 0.61 mm.

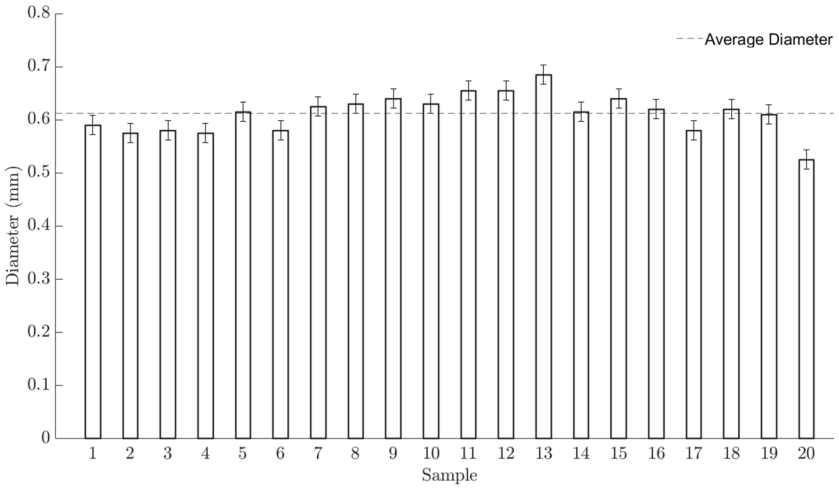

Figure 8.11: Fiber diameter measurements using micrometre screw-gauge

It must be kept in mind that despite the assumption, the cord being studied is more elliptic than circular. This means that due to its shape, it is more likely that the measurement is taken along the cord's minor axis instead of the major axis. Thus, the measurements may slightly under-predict the cross-sectional area, and thus the nominal stress. This further strengthens the argument to use strain as a failure criterion rather than stress. This is because the strain is directly computed from experimental measurements, and needs no additional data.

8.3. Interface Pull Out Tests

The procedures used for conducting the fibre pull-out tests to evaluate the rubber-fibre interfacial properties are elaborated on in this section. Despite finally not being used in the project, this section is still included to serve as a reference to readers who wish to improve the current setup.

For CRCs, a well-defined standard to measure the force to cause interface failure is ASTM D4776/D4776M [114]. This involves the preparation of an H-type specimen (figure 8.12) in which the cord is embedded within two rubber blocks. The blocks are then loaded in a tensile testing machine and tested until the cord is separated from the rubber under controlled displacement loading. To create the specimens, a mould was machined at TANIQ with slots for the rubber strips and the cords - see figure 8.12. The cords are sandwiched between the rubber sheets and are laid under tension (see figure 8.12b) using suspended end-weights. Non-stick PTFE tape was filled in the rubber grooves to minimise rubber flow during curing - see figure 8.12c. The mould is then closed using retainer bolts, and the specimen is cured at 158C to achieve vulcanisation.

Since the aim of the current experiment was to capture the complete load-displacement history, and not only the failure load, the samples were modified from 'H' specimens to 'T' specimens - see figure 8.13b. This has the following benefits:

1. Each test will capture the pull-out response of only one fibre-rubber interface in a 'T' specimen, while the response of an 'H' specimen includes the response of two such interfaces. This means that with a 'T' specimen, the obtained data may be used as-is without additional data filtering or averaging.
2. Double the number of 'T' specimens can be created from a single moulding batch by splitting one 'H' sample into two.

To prevent clamping force from affecting the pull-out results, 'L' grips were constructed from sheet metal to be used with the 10 kN Zwick-Roell tensile testing bench (figure 8.13a). A special camera

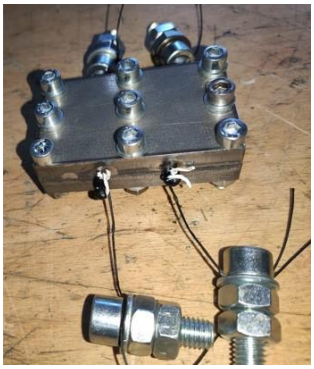

(a) Fully constructed mould

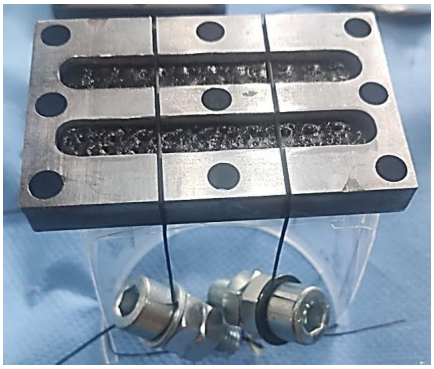

(b) Use of bolts for fiber tensioning

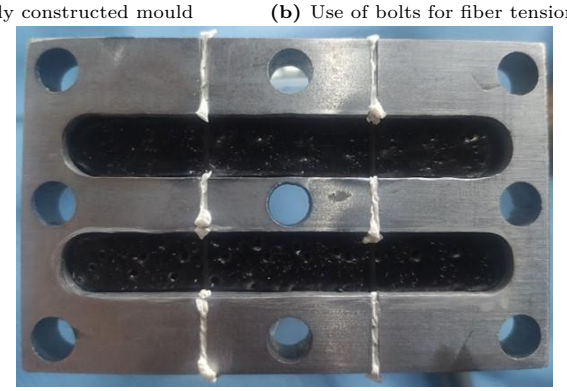

(c) Packing of fiber grooves with PTFE tape to minimise rubber ingress

Figure 8.12: Mould used for fibre pull-out tests

setup with an 80 mm lens and an additional extension tube was arranged to click highly zoomed pictures of the specimen every 1/4 s to allow precise measurement of relative displacement between the rubber block and the embedded fibre. This measurement was based on the spacing of two white marker dots that were placed on the specimen prior to loading - see figure 8.13c. A MATLAB script was written to post-process the data from the images and the load cell to produce a load-displacement plot.

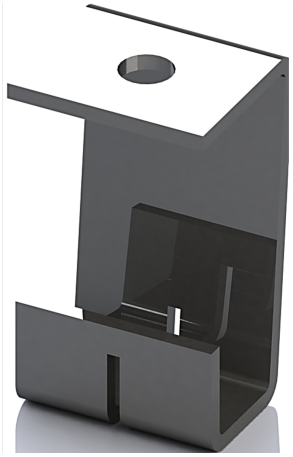

(a) 'L' attachment for holding specimen

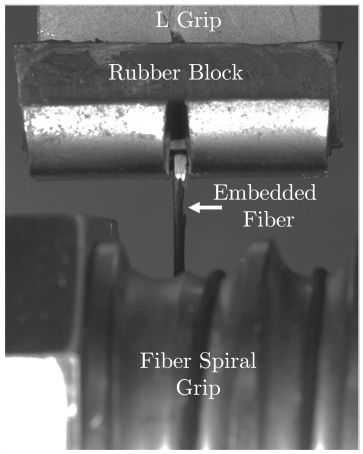

(b) Experimental setup for pullout test

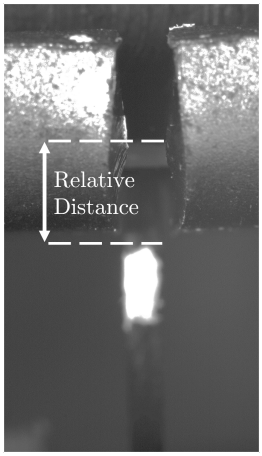

(c) Tracking fiber pull out displacements

Figure 8.13: Fiber pull-out test - experimental setup

To calibrate a traction separation law, data for the maximum pull-out traction and the area under the traction-separation curve is needed. This area may be interpreted as the fracture toughness G of the interface. The traction-separation curves obtained for five 'T' samples after data processing are seen in

figure 8.14a. The calculated values for maximum traction and G are seen in figure 8.14b and figure 8.14c respectively.

The numerical measure of data scatter for the pull-out tests is determined by the ratio of the standard deviation and the mean value. For the maximum traction, this value is at 11.38%, while for G, this is even higher at 21.09%. This scatter was too high to be considered a statistically homogeneous data set, and thus the collected data was not used further.

8.4. Burst Tests

This section focuses on the experimental setup developed to conduct the burst tests on-site at TANIQ B.V. Firstly, the mechanical and electrical design for the burst-test rig is detailed, following which the software for image processing is elaborated upon. Finally, key observations made in the specimens are highlighted post the burst tests.

8.4.1. Burst Test Rig

Burst tests were conducted by pressuring the CRC specimen with water via a pump. Pneumatic pressurisation is avoided due to its explosive nature. Conventionally, burst tests are conducted at TANIQ without a dedicated test bench as seen in figure 8.15. This setup was convenient for obtaining only the final burst pressure as a single data point. However, for this project, a test rig was considered important for the following reasons:

1. Having a test rig allows for the specimen boundary conditions to be clearly defined. This helps create matching boundary conditions in the FEA model, thus leading to a better correlation between experiments and models.
2. Having the specimen vertical, along with the addition of data collection electronics, allows for the progressive collection of pressure and displacement data which can be then used to compare against the loading history in the FEA model.

A burst test rig was designed and constructed using standard aluminium 20×20 extrusions and brackets as shown in figure 8.16. This allowed a modular design that could be easily dismantled, stored, and modified for other products used at TANIQ. In terms of boundary conditions, the product was clamped to the base plate using M8 bolts, while the top was free to expand. Provisions were made for two Wenglor CP35MHT80 high-precision laser distance sensors for axial and diametrical length measurements.

Despite the provision for laser distance sensors, the following issues prevented their use:

1. As the test specimen is pressurised, it will grow axially. This means that the diameter measurements taken by the fixed laser sensor will be at differing points on the specimen throughout the load cycle. This is not very convenient while validating the FEA model.
2. There were concerns regarding the laser sensors suffering water and impact damage during the burst tests.

Instead, photographic measurements were chosen to obtain the axial and diametrical displacements. As an added advantage, this method allows for a full-field measurement, rather than just a single point. A Sony Alpha 7S digital camera was used to obtain the required photographs. To obtain a continuous log of internal pressure within the product, an RS-Pro $0 - 40$ bar analogue pressure transducer was used. An Arduino-Uno based digital data collection brick was created as shown in figure 8.17 to collect the data from the camera and the pressure sensor (with additional provisions to collect data from the laser sensor in the future). Here, the analogue inputs from the laser and pressure sensors are converted to digital signals using a 16-bit ADC, while a digital switch controls the shutter click of the camera

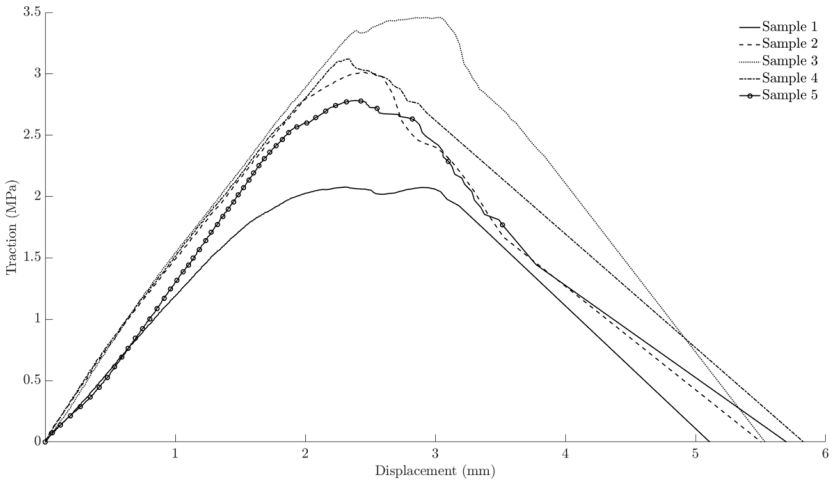

(a) Traction separation curve

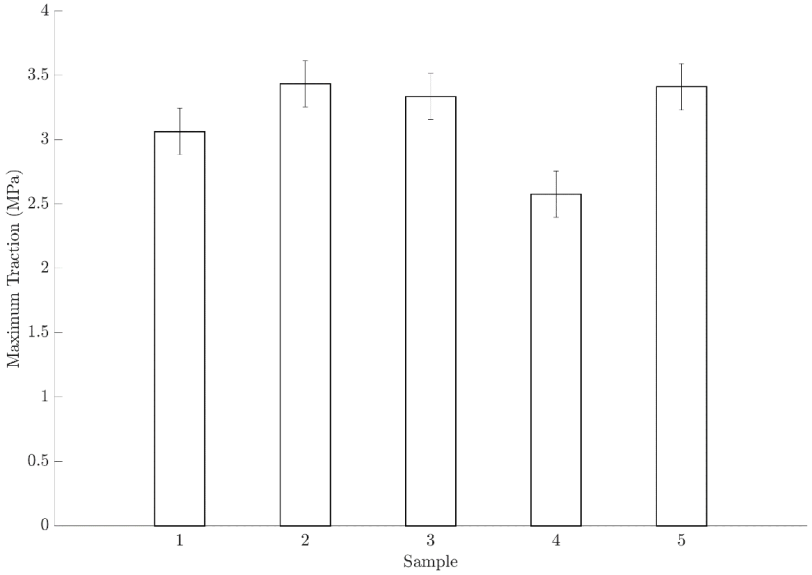

(b) Maximum tractions

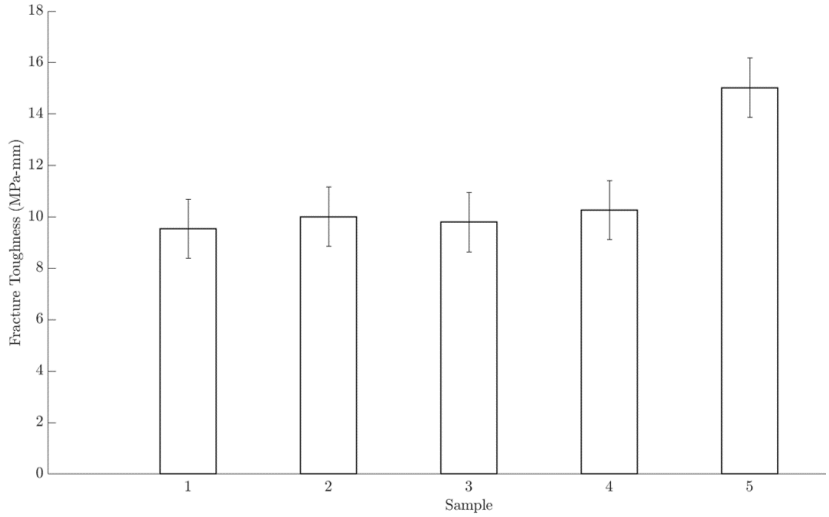

(c) Fracture toughnesses

Figure 8.14: Fiber pullout processed data for T specimen

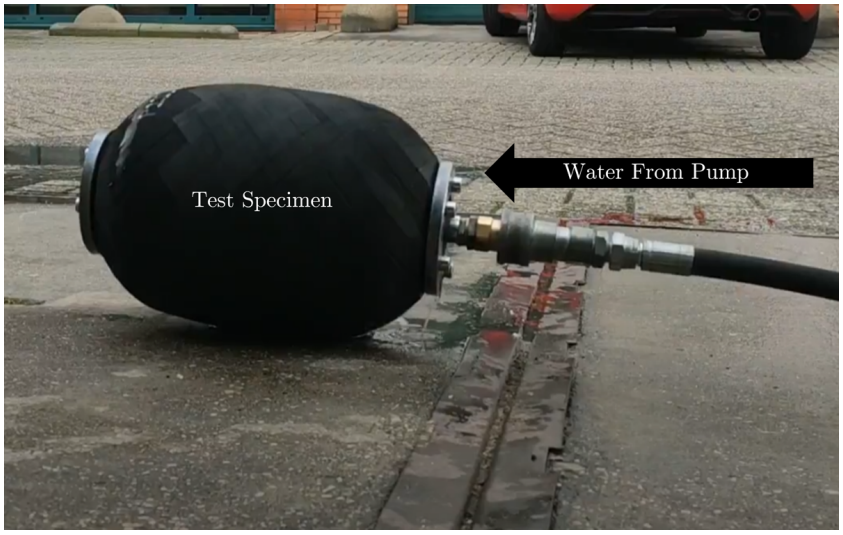

Figure 8.15: Conventional burst test method without test rig

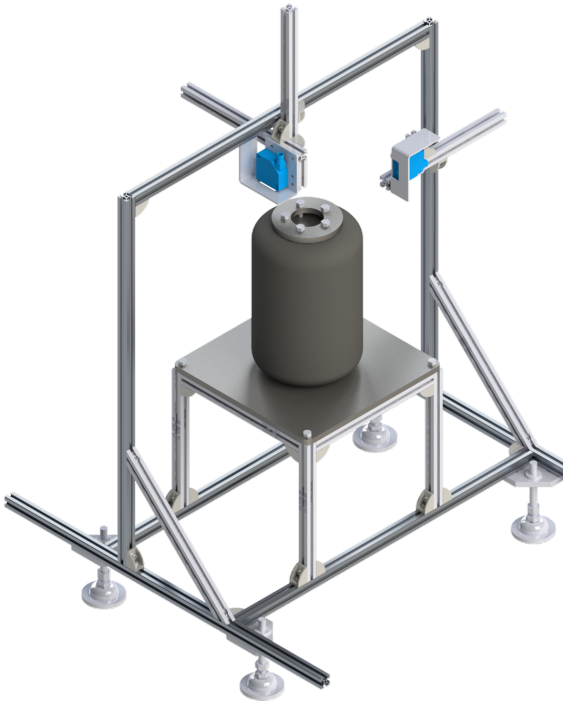

Figure 8.16: Burst test rig with laser distance sensors (blue)

automatically. The data streams from the camera and the pressure transducer were synchronised using an onboard real-time clock (RTC) module and then were stored on an SD card in real-time as a .csv file. The setup as constructed on site is seen in figure 8.18.

8.4.2. Measurements via Image Processing

For the specimen measurements, an image processing script was written in MATLAB that extracted the boundary of the specimen from a high-contrast image taken by the data collection brick - see figure 8.19. To create sufficient contrast, a high-intensity backlight was used as seen in figure 8.18. The image was further binarised in MATLAB to get a crisp boundary definition. Horizontal and vertical rulers present

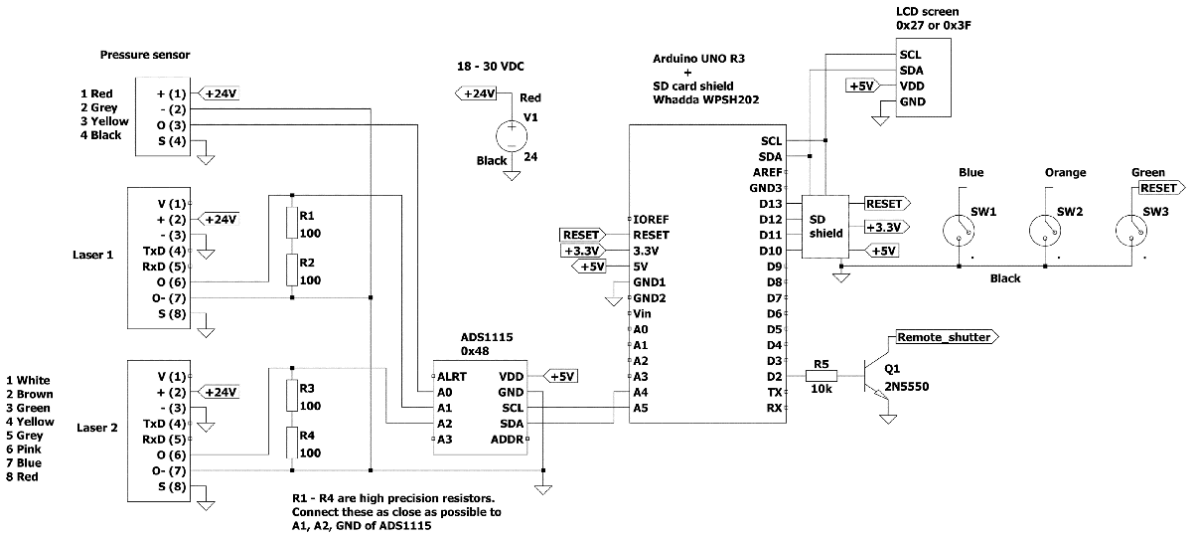

Figure 8.17: Circuit diagram for data collection brick

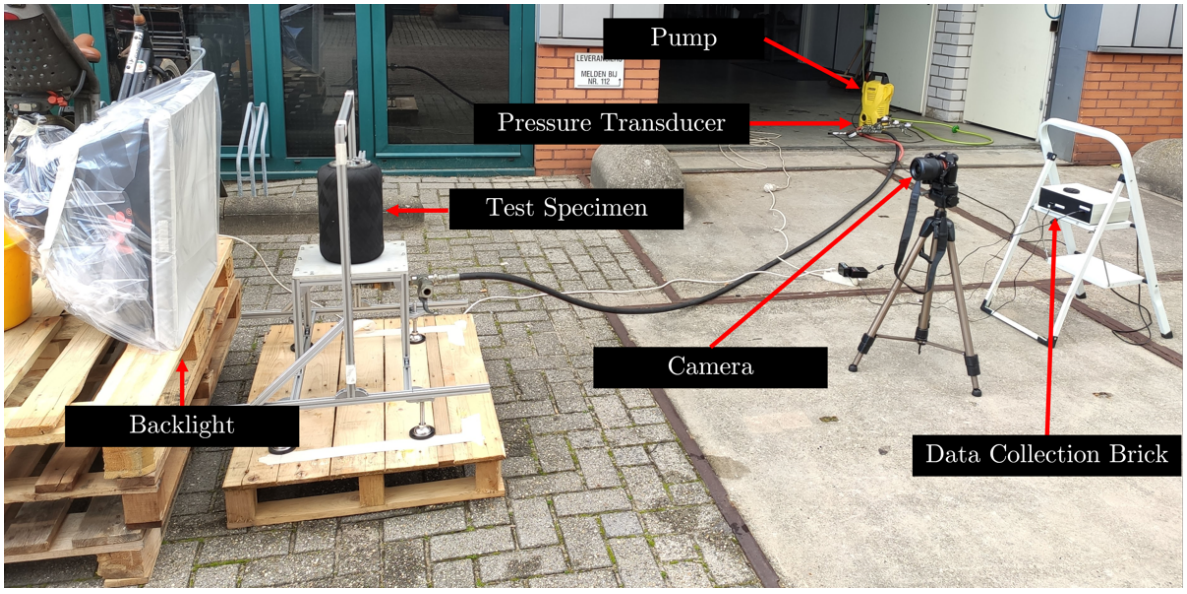

Figure 8.18: Burst test setup at TANIQ B.V.

on the test-rig frame helped to calibrate distances from pixels to mm.

8.4.3. Burst Test Qualitative Data

Apart from data regarding the burst pressure and specimen deformation, a lot of qualitative observations may be made from the burst test specimens. The burst phenomenon itself is an interesting one in which there is not a complete rupture of the specimen. Instead, a large blister forms at the site of fibre failure - see figure 8.20. This indicates that at the burst pressure, the strains in the specimen are low enough for the rubber to take up the loads despite fibre failure. This reinforces the argument in section 6.3 that product failure is dominated by rubber and interface damage and not rubber damage.

The blister itself is formed due to the ingress of water between the fibres and the two rubber layers after the burst. This suggests a complete degradation of the interface at the failure location. To investigate this effect, each specimen was cut open at the burst site for observation. The exact position of failure

(a) Image from camera

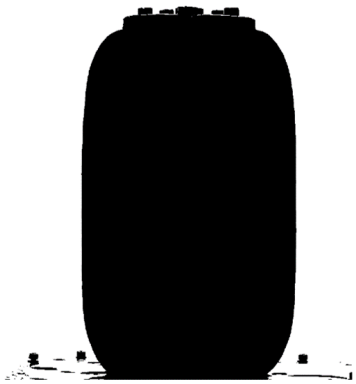

(b) Binarised image

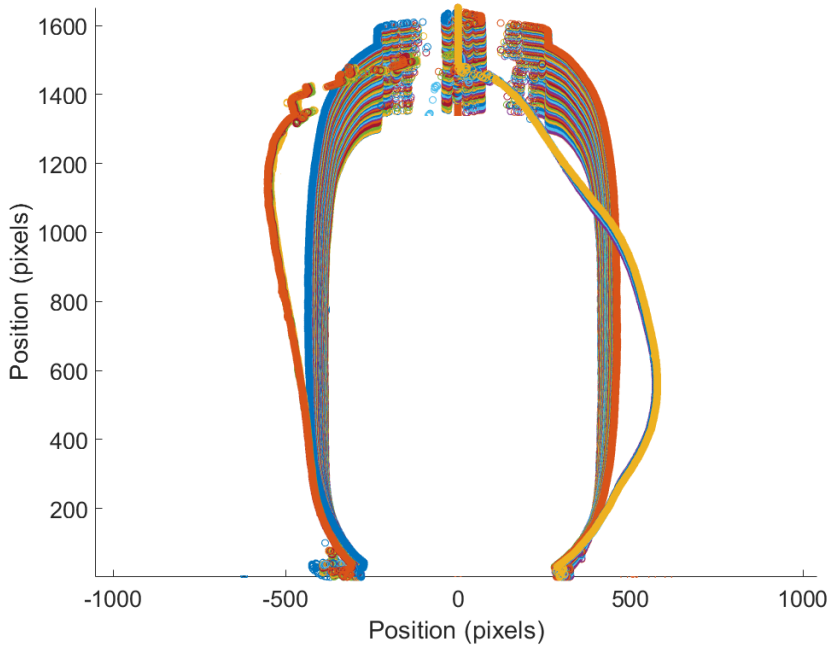

(c) Obtained boundaries from all images

Figure 8.19: Specimen deformation measurements via image processing

is marked by a failure of the inner rubber layer - see figure 8.21a. This is probably the region where the ingress of water initiates. As expected, in regions away from the failure site, there is perfect bonding between the rubber and cord at the interface. However, within the blistered region, there is a visible separation of the rubber and the cord - see figure 8.21c. Here, the cord can be pulled out of the rubber with minimal force. Additionally, 'sockets' of debonded regions are observed that follow the fibre winding pattern, which indicates regions of interfacial failure and subsequent water penetration.

8.5. Conclusion

In this chapter, the experimental package of the project is detailed. First, the material characterisation tests are presented. Rubber characterisation was achieved via simple tension, planar tension and equibiaxial tension tests. These tests were proven to have an equivalent deformation state to uniaxial tension, simple shear, and uniaxial compression respectively under certain limits. For the fibres, procedures followed to obtain the uniaxial tensile data and the cross-sectional area are then presented. Finally, an

Figure 8.20: Blister formation post burst

(a) Rubber damage at damage initiation point

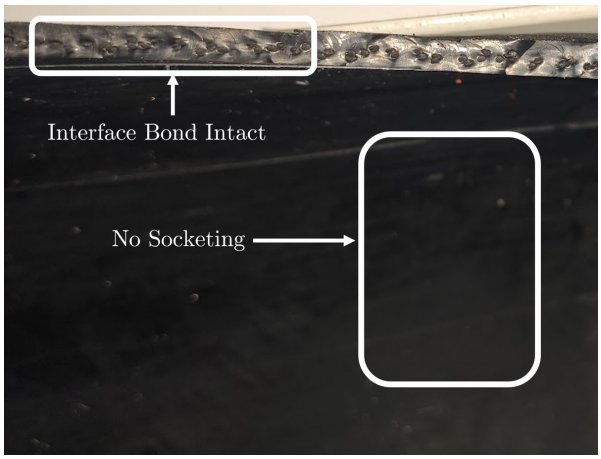

(b) Undamaged region

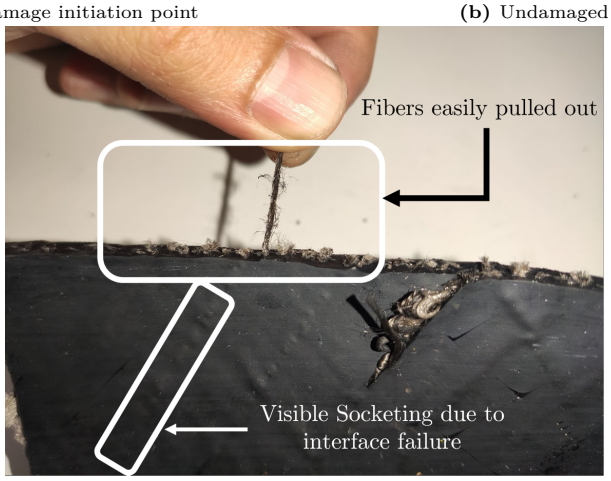

(c) Damaged region

Figure 8.21: Specimen autopsy post burst

overview of the fibre pull-out tests to characterise the interface was provided. Due to the high scatter in the data, it was not used for the project.

The second part of the chapter focuses on the burst tests conducted to validate the FEA model. To obtain data continuously throughout the load history, a burst test rig was designed and manufactured

that clamps the specimen in a vertical position. Additionally, an electronic data collection brick was designed that controlled and stored input from an analogue pressure transducer, a camera, and (optionally) two laser distance sensors to digitise the complete pressure-displacement response of the specimen. Finally, the burst specimens were cut open at the region of the burst, and the cross-section was studied qualitatively. It was observed that in the region of burst, fibre and interface failure dominated the damage response, which validated the decision to not model rubber damage.

This page was intentionally left blank.

9

Conclusions and Recommendations

Considering the research questions presented in section 1.2, the main research objective for this project can be formulated as follows:

Research Objective

To model and experimentally verify the burst pressure of a cylindrical CRC structure under internal pressurisation using a computationally efficient non-linear FEM model.

This project has achieved the above objective by creating a global-local non-linear FEA model to capture the response of the CRC structure. The local model in particular is able to capture progressive fibre degradation, along with the stress states at the rubber-fibre interface and in the rubber matrix. A simplified fibre overlap model is also created that is able to predict the undulating fibre geometry created as a result of filament winding. The stress concentrations in the regions of overlap have proved critical in driving failure and are consistent with discussions in literature.

Computational efficiency is obtained by modelling a very small rhomboidal region in high fidelity, while the rest of the structure is modelled using a homogenised global rebar model. Correlation is shown with experimental data from the burst tests of multiple CRC specimens using a created burst test rig. Excellent agreement ($1\% - 3\%$ deviation) is seen between the global displacement solution of the rebar model and the displacements logged by the test setup. Additionally, consistent agreement for the burst pressures between the local model and the experimental data is seen, with deviation being between 6% and 7% across two different specimen designs with varying rubber thicknesses.

To complete the discussion of the results, and also to serve as a summary to the project, this chapter first presents the main highlights packaged as answers to the main research questions in section 9.1. Then, the shortcomings of the current research along with recommendations for future work are presented in section 9.2.

9.1. Answering the Research Questions

With reference to the primary research question presented in section 1.2, key highlights of the project can be revisited by providing relevant answers to each research sub-question. This will be discussed in this section.

9.1.1. CRC Damage Modes

Identifying Relevant Damage Modes

Via an analysis of literature, the main damage modes for a CRC structure were identified as rubber damage, fibre damage, and interface damage in section 6.3. Despite having several damage modes within it, rubber damage as a whole was ignored in the analysis due to the relatively low strains encountered in the analysis. Rubbers usually have failure strains exceeding 100%, and thus must be included if a highly compliant structure is created. Fibres, being the critical load-bearing members in the structure, are critical in determining the final failure load of the structure, while early degradation of the rubber-fibre interfacial layer was found to be an important factor in disrupting the load-path of the structure, thus leading to early fibre failure. Thus, in this project, fibre and interfacial failure were chosen as the critical damage modes for predicting the single-cyle burst pressure.

Experimental Characterisation of Materials and Damage Modes

Despite the twisted nature of the cords used for this project, it was decided to treat the cord structure as a continuum. The load-displacement curves obtained from uniaxial tensile tests of the cords were used to define a hyperelastic Marlow material model for the fibre, along with defining its failure points. The Marlow material model was chosen due to its ability to replicate experimental data exactly for a single testing mode.

Fibre pullout tests, as described in chapter 8, were attempted to characterise the rubber-fibre interface. However, due to excessive data scatter, along with inconclusive traction-separation curves, this data was not used for the study. Finally, despite not being considered for damage, experimental characterisation of the rubber was necessary to calibrate an appropriate hyperelastic material model. Tensile tests in three modes - uniaxial tension, biaxial tension, and planar tension were conducted, and via the method of least-squares, a 6^{th} order Ogden model was fit to the data.

Specimen Design

Keeping in mind the damage modes identified, along with the analysis methodology chosen, a specimen with the following characteristics was required:

1. The specimen should be representative of a typical CRC product, with all the design, production, and damage tendencies captured in it.
2. To allow for the analysis methodology chosen, a constant state of deformation should exist over the non-dome regions of the specimen.
3. Since the specific clamping and end conditions for a specific product are not the topic of study in this project, the chosen design should not have failure driven by the conditions in the polar domes.

Considering the said requirements, a close-ended cylindrical design was chosen as the specimen of study for this project (see section 4.4). To offset the issue of the small axial length of the available sample, a geodesic winding angle was chosen to cause minimal fibre rotation during loading, and hence ensure a near-constant deformation state in the cylindrical region.

9.1.2. FEA Modelling Methodology

Choice of Modelling Scale

Modelling the chosen CRC is inherently a multi-scale problem. There are a total of three scales that can be modelled just for the fibre, starting from a single filament, right up to the cord construction

comprising multiple twisted filament bundles. Additional modelling complexity can be considered if a scale small enough to notice fibre undulation is considered.

A survey of literature for modelling techniques for filament wound composites (see section 3.2) showed that modelling fibre overlap is an essential aspect of capturing local fibre stress concentrations accurately in the development of a damage model. Additionally, modelling interface damage is only relevant if the interface surrounds a geometrically accurate version of the fibre. Keeping these requirements in mind, a global-local model was developed to obtain the necessary fidelity in the most efficient manner. The overall global displacement response was captured using a macro-level rebar model, while the local inhomogeneities were captured using a meso-level rhomboidal RVE with fibre overlap.

Choice of Damage Laws

During the tensile tests presented in chapter 8, it was observed that the fibres undergo sudden brittle failure. Keeping this in mind, it was chosen to have element deletion using a maximum axial strain criteria failure law for the fibres. Doing so has the following benefits:

1. Axial strain is directly measured from the tensile testing bench, while quantities such as stress need additional area measurements to be used. Thus, using axial strain reduces one level of averaging and measurement inaccuracies.
2. Using element deletion prevents having a softening response with a negative slope in the load-displacement response, thus allowing better convergence using the Newton-Raphson algorithm.

For the interface, a cohesive traction-seperation law was initially planned to model damage. However, due to unreliable material data along with convergence issues in the model, this attempt was not used. Correspondingly, there are no included damage laws for the interface.

9.1.3. Experimental Burst Tests

Choice of Logged Data

Due to the separated global-local analysis methodology used, appropriate data needed to be collected from a data-logging rig that helped evaluate the performance of each model individually. From the comparison with literature data done in section 6.1, it was concluded that displacement data is sufficient to validate the functionality of the local model. Thus, it was decided to log the displacements in the axial and radial directions of the specimens during the burst tests. Doing this allowed for the local model to be used only to validate the maximum burst pressure encountered in the experimental specimens. Thus, in total, axial and diametrical displacements, along with a real-time feed of internal pressure data was needed to help validate the FEA model.

Test Setup Design

Section 8.4 details the burst test rig designed to collect displacement and pressure data. A vertical mounting stand was constructed to have controlled boundary conditions for the specimen, while a combination of photographic measurements and analogue pressure transducer data streams was used for constructing the load-displacement response. An Arduino-Uno based data collection brick was designed to collect, process and store the experimental data.

9.2. Recommendations for Future Work

The created model had a relatively small but consistent over-prediction of the burst pressure. Depending on the type of product, having such a non-conservative solution may not be ideal. The following section

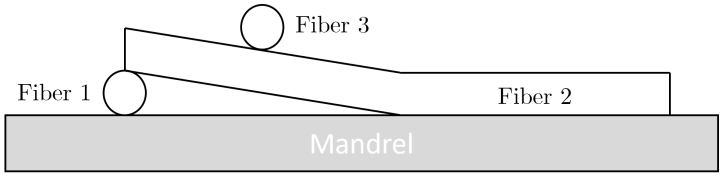

(a) Current Model

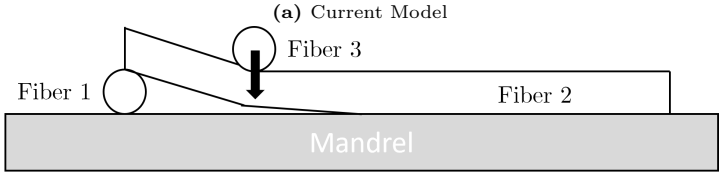

(b) Proposed Model

Figure 9.1: Comparison of fibre overlap geometry between current and proposed models

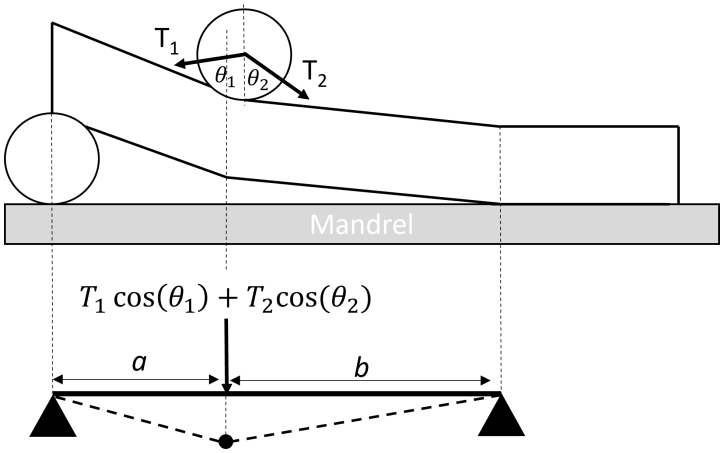

Figure 9.2: Beam model for fibre pushdown

suggests possible improvements to the model that may make it more accurate, and also may help to make the created model more widely applicable across several product types.

9.2.1. Fiber Overlap Model

The developed fibre overlap model in chapter 3 makes a simplifying assumption in which it ignores the downward compaction of the fibre. This can be demonstrated in 2D via figure 9.1, where figure 9.1a shows the overlap fibre placement as is described by the model, and figure 9.1b shows how it would be in reality.

This mismatch is because the current model is purely geometric, and does not account for fibre tension, which is the driving force that pushes the fibres radially downward. This solution can be improved by incorporating an analytical beam model solution for the fibre being pushed down as shown in figure 9.2. Here, the downward force consists of the sum of force components on either side of the overlap point that contributes to the compacting force. This force is applied at an appropriate point on a beam, whose flexural modulus is dictated by the fibre's geometry and the tensile forces it is wound with. Boundary conditions for this bridging beam model would need careful consideration, as, depending on the friction conditions and the clamping forces at the fibre ends, the conditions could vary between fully pinned to fully clamped. This would need to be finalised after comparison with experimental measurements.

The new points generated via this beam analysis may then be used to recalculate the convex hull as suggested in chapter 3. It must be kept in mind that although this solution may be an improvement over the current model, it is still highly simplified, and is used only for generating the initial fibre geometry.

In doing so, the initial stress state in the fibre is ignored during the analysis.

9.2.2. Fiber Material Model

The Marlow material model used to describe the fibre material response in chapter 5 is an isotropic one, implying an equal stiffness in all material directions. Studies have shown that there are as many as four orders of magnitude differences in the axial and transverse moduli of twisted cord constructions [52]. Despite not using transverse damage as a critical failure mode for the CRC, including this soft response in the transverse direction can be vital in obtaining representative displacements at the cord-rubber interface. This, in turn, may lead to earlier interface failure, and consequently a more conservative burst pressure estimation.

Including this transverse orthotropy is a straightforward task using Spencer's model [32], [33] introduced in section 2.5. Such an invariant formulation can be coded into ABAQUS using the UANISOHYPER_STRAIN user subroutine [115], or by the creative implementation of the generalised Fung or Holzapfel anisotropic strain energy functionals already implemented in ABAQUS [116]. If the latter is chosen, it must be kept in mind that these models were primarily created for modelling biological tissues, as introduced in section 2.5.

Since characterising the transverse response of fibres is a tricky task experimentally, a conservative estimate may be used, in which the transverse stiffness can be made equivalent to the rubber response. Despite this, some critical failure modes of the fibre, such as catastrophic transverse tensile failure due to fibre twist-uncoiling are not included. Additionally, factors such as inter-fibre bundle friction are also not included, which are shown to have a noticeable impact on fibre failure. Including these effects warrants a multi-scale analysis, in which data from a detailed twisted cord micro-model is homogenised and used as the material model for larger-scale analyses. This already is too complex a task for the current project objective.

9.2.3. Interface Modelling

As detailed in section 6.3 and chapter 8, there were considerable shortcomings in the modelling of the interfacial layer in the project. Literature has shown interfacial damage to be a critical damage mode in CRCs, and hence efforts must be made to understand the causes of these shortcomings and suggest relevant corrections.

Tooling

The erratic traction-separation curves obtained via the pull-out tests (see figure 6.14) can be linked to inadequate control over the specimen production and clamping in the tensile bench. As per the ASTM standard, there should be no rubber present on the fibres except in the region where it is embedded in the block. To achieve such a finish, a mould with much tighter machining tolerances would have to be used, which was not possible due to the lack of a CNC mill. Due to this, rubber lips as seen in figure 5.7 were present on the cords, which caused sudden fluctuations in the load-displacement plots, rendering them unusable.

Additionally, solid metal machined hooks were recommended by the standard to be used with the test bench to allow accurate rubber positioning - see figure 9.3. The hooks made for this project were from bent sheet metal, which were manufactured with much higher tolerances. This meant that the spacing between the hooks had to be wider apart, implying that fibre strain had a larger influence on the logged displacement response.

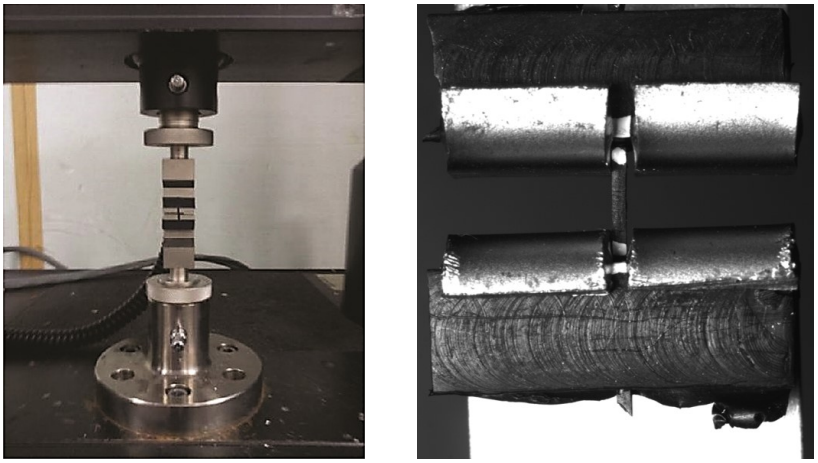

(a) Ideal test setup [117] **(b)** Test setup used for this project

Figure 9.3: Comparision of ideal and current test setup for the ASTM D4776 fiber pullout test

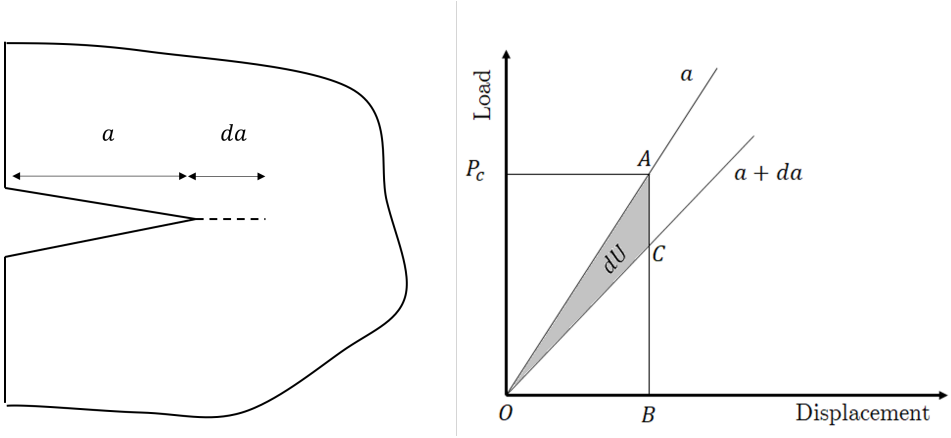

Figure 9.4: Illustration of energy released dU for crack growth by length da [118]

Testing Procedures

The ASTM D4776 standard aims at obtaining the maximum fibre pull-out force of the cord from the cord-rubber H-specimen. It is not designed to be used to calibrate a traction-separation law, and thus suitable changes should have been made for the same. An important parameter to formulate a traction separation law is the fracture toughness of the interface, which is the amount of energy released when the crack propagates by a unit length in the material. To have accurate measurements of this property, the sample can be progressively loaded and unloaded quasi-statically across several strains. This allows the exact point of damage initiation to be identified, while also allowing the energy lost for a certain crack length growth to be clearly visualised - see figure 9.4. This is in contrast to the monotonic loading of the sample to failure as specified by the standard.

Convergence Issues

Modelling damage, in general, can lead to convergence issues due to consistently negative tangent stiffnesses in the softening regime. To overcome this issue, a 'zig-zag' bilinear traction-separation law may be defined instead of a smooth one as shown in figure 9.5 [119]–[121]. Here, the secant stiffness of the material is degraded in a step-wise manner, which leads to the following benefits:

1. At all points in the traction-separation curve, there is a positive tangent modulus, which aids the convergence of the solution.

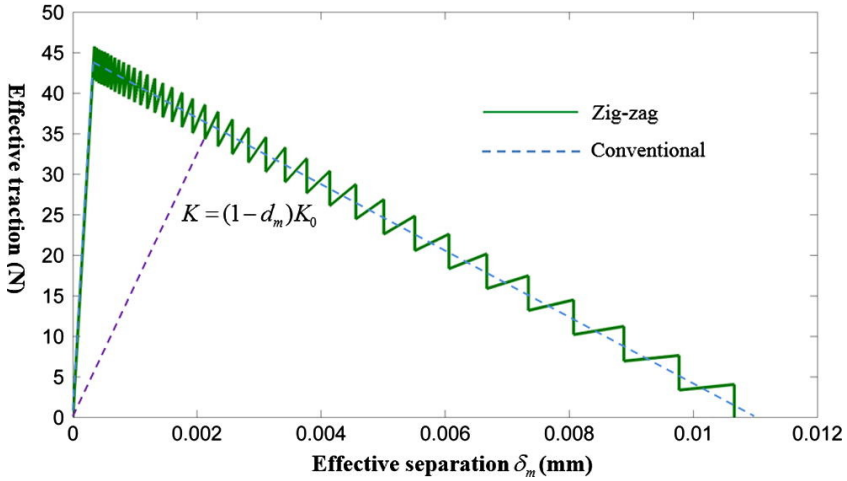

Figure 9.5: Zig-zag type bilinear softening curve [119]

2. In each step of the zig-zag curve, the tangent modulus, and hence also the damage variable, is a constant. On the contrary, if a smooth bilinear curve is used, these values must be recalculated and updated for every displacement increment, no matter how small. Avoidance of these repeated calculations allows for significant savings in computational effort.

9.2.4. Feedback loop between global and local model

The current implementation of the submodelling approach is one-way, which implies that there is no feedback from the local model back to the global model. Feedback is not necessary until the product starts undergoing damage. However, after damage initiation, the subsequent response of the structure under loading will be softer, which means the global model should undergo larger deformation. This in turn drives faster damage progression in the local model, thus forming a closed loop. For products such as those modelled in this study, these failure progressions are not very important since the cord volume fraction is considerably low. However, with increasing cord-volume fractions, failure may not be dictated by the failure of a single fibre in the rhomboidal RVE, and hence accurate progression of damage should be modelled.

As discussed, for an RUC, this is a straightforward task if periodic boundary conditions are implemented. In each increment in the local model where damage occurs, a new homogenised material response can be created and applied to the global model which takes into account softening due to the current level of damage. However, for an RVE, such homogenisation is not as straightforward. In such a case, as a first-order estimation, the parameters of the rebar material can be adjusted - specifically the rebar spacing. It can be assumed that for every fibre break in the local model, there is a corresponding increase in the fibre spacing in the global model, which decreases its stiffness. A fibre can be considered as fully failed when there is the deletion of all elements in one fibre layer along the circumference. The workflow for such an implementation may be as seen in figure 9.6.

9.2.5. End Effects

The present work assumes that failure will always occur away from the domes of the product. For many CRC products such as expansion joints (figure 1.1), the metallic flanges present at the product ends are pinch-points and sources of damage initiation. To allow damage to be captured in these regions, a detailed submodel would have to be created that incorporates all the relevant phenomena such as contact, pressure penetration, and flange plasticity. The work of van der Linden [122] on a similar subject may be used as a starting point to explore such modelling solutions.

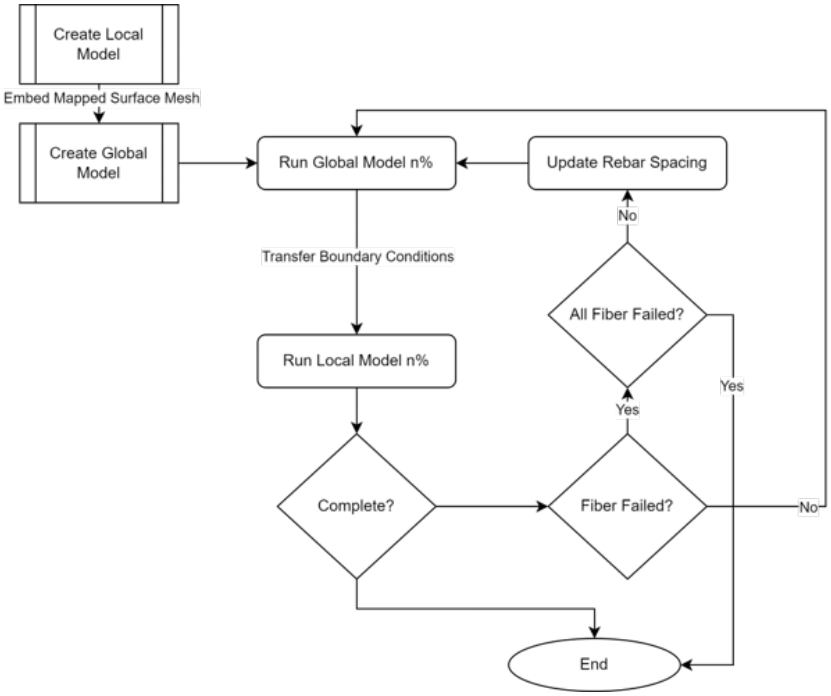

Figure 9.6: Possible workflow for implementing a two-way submodel with progressive fiber failure.

9.2.6. Production Parameters

Finally, one of the main components missing in the current study is the effect of initial conditions. These initial conditions are the effect of the production parameters, which are influenced by the filament winding process and vulcanisation in the oven. Some important effects not considered in this study include:

1. Effect of the initial stress state in the fibres due to winding under tension.
2. Effect of fibre deviation due to fibre slippage and winding with multiple fibres (see figure 9.7).
3. Stochastic analysis of defects, such as voids and regions of under-cured rubber.

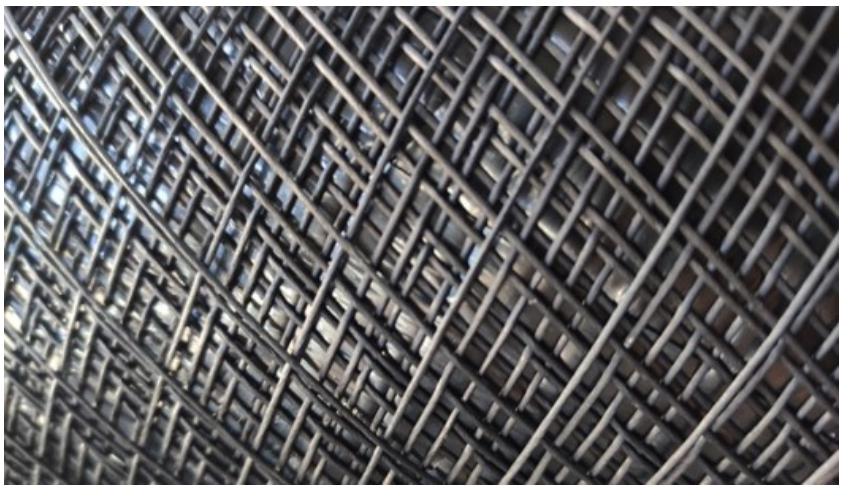

Figure 9.7: Uneven spacing between fibres due to slippage. Slippage occurs either due to insufficient friction, or because the winding program does not account for radial buildup during the winding process.

For a link between production parameters and product performance, a manufacturing simulation, similar

to the one presented by Zhou et. al [123] may be conducted. Stochastic defects may be characterised and included in the model using Monte-Carlo simulations as proposed by Rafiee and Torabi [124].

This page was intentionally left blank.

References

[1] J. D. Walter, *Cord-Rubber Tire Composites: Theory and Applications.* 1978. DOI: 10.5254/1.3535749.

[2] A. Bhosale, "Literature Review: Burst Pressure Prediction of Cord-Rubber Composite Structures using FEA Modelling," TU Delft, Delft, Tech. Rep., Feb. 2022.

[3] S. K. Clark, "The Plane Elastic Characteristics of Cord-Rubber Composites," The University of Michigan Research Insitute, Ann Arbor, Tech. Rep., 1960.

[4] C. Kassapoglou, *Design and analysis of composite structures with Applications to Aerospace Structures*, 2nd. Delft: John Wiley and Sons, 2013, ISBN: 9780470972632.

[5] J. L. Turner and J. L. Ford, "Interply Behavior Exhibited in Compliant Filamentary Composite Laminates," *Rubber Chemistry and Technology*, vol. 55, no. 4, pp. 1078–1094, Sep. 1982, ISSN: 1943-4804. DOI: 10.5254/1.3535915.

[6] J. L. Ford, H. P. Patel, and J. L. Turner, "Interlaminar shear effects in cord-rubber composites," *Fibre Science and Technology*, vol. 17, no. 4, pp. 255–271, 1982, ISSN: 00150568. DOI: 10.1016/0015-0568(82)90021-5.

[7] T. Akasaka and M. Hirano, "Approximate elastic constants of fiber reinforced rubber sheet and its composite laminate," *Composite Materials and Structures*, vol. 1, no. 1, pp. 70–76, 1972.

[8] J. Halpin and S. Tsai, "Effects of Environmental Factors on Composite Materials," Tech. Rep. June, 1969, pp. 67–423.

[9] V. E. Gough, "Stiffness of Cord and Rubber Constructions," *Rubber Chemistry and Technology*, vol. 41, no. 4, pp. 988–1021, Sep. 1968, ISSN: 1943-4804. DOI: 10.5254/1.3547240.

[10] H. P. Patel, J. L. Turner, and J. D. Walter, "Radial Tire Cord-Rubber Composites," *Rubber Chemistry and Technology*, vol. 49, no. 4, pp. 1095–1110, Sep. 1976, ISSN: 1943-4804. DOI: 10.5254/1.3534991.

[11] B. Chen, "Lecture 2: Material Nonlinearity," in *Lecture Notes: Non-Linear Modelling*, Delft: TU Delft, 2020.

[12] K. Miller, "Testing Elastomers for Hyperelastic Material Models in Finite Element Analysis," Axel Products, Ann Arbor, Tech. Rep.

[13] T. Belytschko, W. K. Liu, B. Moran, and K. I. Elkhodary, *Nonlinear Finite Elements for Continua and Structures*, 2nd. Chichester: John Wiley and Sons, 2014, ISBN: 9781909507227.

[14] J. Bergström, "Elasticity/Hyperelasticity," in *Mechanics of Solid Polymers*, Elsevier, 2015, pp. 209–307. DOI: 10.1016/B978-0-323-31150-2.00005-4.

[15] M. E. Gurtin, *An Introduction to Continuum Mechanics.* Academic Press, 1981.

[16] G. Holzapfel, *Nonlinear Solid Mechanics: A Continuum Approach for Engineering Science*, 1st. John Wiley and Sons, 2000.

[17] R. Rivlin, "Large elastic deformations of isotropic materials IV. further developments of the general theory," *Philosophical Transactions of the Royal Society of London. Series A, Mathematical and Physical Sciences*, vol. 241, no. 835, pp. 379–397, Oct. 1948, ISSN: 0080-4614. DOI: 10.1098/rsta.1948.0024.

[18] R. Ogden, *Non Linear Elastic Deformations.* Glasgow: Dover Publications, 1997, ISBN: 978-0-486-31871-4.

[19] O. H. Yeoh, "Characterization of Elastic Properties of Carbon-Black-Filled Rubber Vulcanizates," *Rubber Chemistry and Technology*, vol. 63, no. 5, pp. 792–805, Nov. 1990, ISSN: 1943-4804. DOI: 10.5254/1.3538289.

[20] S. Kawabata and H. Kawai, "Strain energy density functions of rubber vulcanizates from biaxial extension," in 1977, pp. 89–124. DOI: 10.1007/3-540-08124-0{_}2.

[21] E. M. Arruda and M. C. Boyce, "A three-dimensional constitutive model for the large stretch behavior of rubber elastic materials," *Journal of the Mechanics and Physics of Solids*, vol. 41, no. 2, pp. 389–412, Feb. 1993, ISSN: 00225096. DOI: 10.1016/0022-5096(93)90013-6.

[22] I. D. Külcü, "A hyperelastic constitutive model for rubber-like materials," *Archive of Applied Mechanics*, vol. 90, pp. 615–622, 2020. DOI: 10.1007/s00419-019-01629-7.

[23] D. Besdo and J. Ihlemann, "A phenomenological constitutive model for rubberlike materials and its numerical applications," *International Journal of Plasticity*, vol. 19, no. 7, pp. 1019–1036, 2003, ISSN: 07496419. DOI: 10.1016/S0749-6419(02)00091-8.

[24] R. Landgraf and J. Ihlemann, "Application and extension of the MORPH model to represent curing phenomena in a PU based adhesive," in *Constitutive Models for Rubber*, 10th, CRC Press, 2017, pp. 137–143, ISBN: 9781315223278.

[25] S. Weiser, T. Lehmann, R. Landgraf, N. Goldberg, H. Donner, and J. Ihlemann, "Experimental and numerical analysis of cord–elastomer composites," *Journal of Rubber Research*, vol. 24, no. 2, pp. 211–225, 2021, ISSN: 1511-1768. DOI: 10.1007/s42464-021-00091-x.

[26] L. Mullins, "Softening of Rubber by Deformation," *Rubber Chemistry and Technology*, vol. 42, no. 1, pp. 339–362, Mar. 1969, ISSN: 1943-4804. DOI: 10.5254/1.3539210.

[27] W. G. Jiang, M. S. Yao, and J. M. Walton, "A concise finite element model for simple straight wire rope strand," *International Journal of Mechanical Sciences*, vol. 41, no. 2, pp. 143–161, 1999, ISSN: 00207403. DOI: 10.1016/S0020-7403(98)00039-3.

[28] N. K. Naik and V. Madhavan, "Twisted impregnated yarns: elastic properties," *Journal of Strain Analysis for Engineering Design*, vol. 35, no. 2, pp. 83–91, 2000, ISSN: 03093247. DOI: 10.1243/0309324001514044.

[29] N. K. Naik and M. N. Singh, "Twisted impregnated yarns: Transverse tensile strength," *The Journal of Strain Analysis for Engineering Design*, vol. 36, no. 4, pp. 347–357, May 2001, ISSN: 0309-3247. DOI: 10.1243/0309324011514520.

[30] X. Li, Y. Wei, Q. Feng, and R. K. Luo, "Mechanical behavior of nylon 66 tyre cord under monotonic and cyclic extension: Experiments and constitutive modeling," *Fibers and Polymers*, vol. 18, no. 3, pp. 542–548, 2017, ISSN: 12299197. DOI: 10.1007/s12221-017-6961-x.

[31] X. Teng, D. Shi, X. Jing, S. Lyu, and X. Yang, "Experimental , analytical and numerical investigation on tensile behavior of twisted fiber yarns," *Chinese Journal of Aeronautics*, vol. 34, no. 5, pp. 278–288, 2021, ISSN: 1000-9361. DOI: 10.1016/j.cja.2020.08.006.

[32] A. J. Spencer, "Constitutive Theory for Strongly Anisotropic Solids.," *Courses and Lectures - International Centre for Mechanical Sciences*, no. 282, pp. 1–32, 1984, ISSN: 02541971. DOI: 10.1007/978-3-7091-4336-0{_}1.

[33] A. Spencer, "Theory of Invariants," in *Mathematics*, A. C. Eringen, Ed., Academic Press, 1971, pp. 239–353, ISBN: 9780122408014. DOI: 10.1016/B978-0-12-240801-4.50008-X.

[34] G. A. Holzapfel, T. C. Gasser, and R. W. Ogden, "A new constitutive framework for arterial wall mechanics and a comparative study of material models," *Journal of Elasticity*, vol. 61, no. 1-3, pp. 1–48, 2000, ISSN: 03743535. DOI: 10.1023/A:1010835316564.

[35] N. H. Nguyen, H.-j. Raatschen, and M. Staat, "A hyperelastic model of biological tissue materials in tubular organs," in *IV European Conference on Computational Mechanics*, Paris: Center for Research and Technology Hellas, 2010.

[36] D. Zhalmuratova, T. G. La, K. T. T. Yu, *et al.*, "Mimicking "j-Shaped" and Anisotropic Stress-Strain Behavior of Human and Porcine Aorta by Fabric-Reinforced Elastomer Composites," *ACS Applied Materials and Interfaces*, vol. 11, no. 36, pp. 33 323–33 335, 2019, ISSN: 19448252. DOI: 10.1021/acsami.9b10524.

[37] X. Q. Peng, Z. Y. Guo, and B. Moran, "An anisotropic hyperelastic constitutive model with fiber-matrix shear interaction for the human annulus fibrosus," *Journal of Applied Mechanics, Transactions ASME*, vol. 73, no. 5, pp. 815–824, 2006, ISSN: 00218936. DOI: 10.1115/1.2069987.

[38] X. Peng, G. Guo, and N. Zhao, "An anisotropic hyperelastic constitutive model with shear interaction for cord-rubber composites," *Composites Science and Technology*, vol. 78, pp. 69–74, 2013, ISSN: 02663538. DOI: 10.1016/j.compscitech.2013.02.005.

[39] A. Aboshio, S. Green, and J. Q. Ye, "New constitutive model for anisotropic hyperelastic biased woven fibre reinforced composite," *Plastics, Rubber and Composites*, vol. 43, no. 7, pp. 225–234, 2014, ISSN: 17432898. DOI: 10.1179/1743289814Y.0000000097.

[40] X. Xu, X. Yao, Y. Dong, H. Yang, and H. Yan, "Mechanical behaviors of non-orthogonal fabric rubber seal," *Composite Structures*, vol. 259, no. November 2020, p. 113 453, 2021, ISSN: 02638223. DOI: 10.1016/j.compstruct.2020.113453.

[41] H. Yang, X. F. Yao, Y. C. Ke, Y. j. Ma, and Y. H. Liu, "Constitutive behaviors and mechanical characterizations of fabric reinforced rubber composites," *Composite Structures*, vol. 152, pp. 117–123, 2016, ISSN: 02638223. DOI: 10.1016/j.compstruct.2016.05.021.

[42] H. Donner and J. Ihlemann, "An anisotropic large strain plasticity model for multifilament yarns," *Pamm*, vol. 14, no. 1, pp. 373–374, 2014. DOI: 10.1002/pamm.201410174.

[43] H. Donner and J. Ihlemann, "An anisotropic large strain plasticity model for multifilament yarns," *Pamm*, vol. 14, no. 1, pp. 373–374, 2014. DOI: 10.1002/pamm.201410174.

[44] H. Donner, "FEM-basierte Modellierung stark anisotroper Hybridcord-Elastomer-Verbunde," Ph.D. dissertation, Technischen Universität Chemnitz, 2017.

[45] H. Donner and J. Ihlemann, "On the efficient finite element modelling of cord-rubber composites," in *Constitutive Models for Rubber*, N. Gil-Negrete and A. Alonso, Eds., 8th, 2013, pp. 149–155, ISBN: 9780429227936. DOI: https://doi-org.tudelft.idm.oclc.org/10.1201/b14964.

[46] H. Donner and J. Ihlemann, "FE analysis of hybrid cord-rubber composites," in *Constitutive Models for Rubber*, 10th, CRC Press, 2017, pp. 437–443, ISBN: 9781315223278.

[47] S. Reese, "Meso-macro modelling of fibre-reinforced rubber-like composites exhibiting large elastoplastic deformation," vol. 40, pp. 951–980, 2003.

[48] S. B. Sharma and M. P. Sutcliffe, "A simplified finite element model for draping of woven material," *Composites Part A: Applied Science and Manufacturing*, vol. 35, no. 6, pp. 637–643, 2004, ISSN: 1359835X. DOI: 10.1016/j.compositesa.2004.02.013.

[49] S. Oman and M. Nagode, "On the influence of the cord angle on air-spring fatigue life," *Engineering Failure Analysis*, vol. 27, pp. 61–73, Jan. 2013, ISSN: 13506307. DOI: 10.1016/j.engfailanal.2012.09.002.

[50] W. Wang, S. Yan, and S. Zhao, "Experimental verification and finite element modeling of radial truck tire under static loading," *Journal of Reinforced Plastics and Composites*, vol. 32, no. 7, pp. 490–498, Apr. 2013, ISSN: 0731-6844. DOI: 10.1177/0731684412474998.

[51] P. Helnwein, C. Liu, G. Meschke, and H. Mang, "A new 3-D finite element model for cord-reinforced rubber composites—Application to analysis of automobile tires," *Finite Elements in Analysis and Design*, vol. 14, no. 1, pp. 1–16, Aug. 1993, ISSN: 0168874X. DOI: 10.1016/0168-874X(93)90075-2.

[52] C. Barry, F. Panerai, K. Bergeron, S. Stapleton, and J. Sherwood, "Mesomechanical modeling of braided cords," *Procedia Manufacturing*, vol. 47, no. 2019, pp. 162–168, 2020, ISSN: 23519789. DOI: 10.1016/j.promfg.2020.04.163.

[53] W. Sprenger and W. Wagner, "On the formulation of geometrically nonlinear 3D-Rebar-elements using the enhanced assumed strain method," *Engineering Structures*, vol. 21, no. 3, pp. 209–218, Mar. 1999, ISSN: 0141-0296. DOI: 10.1016/S0141-0296(97)00182-X.

[54] S. Oman, M. Nagode, and J. Klemenc, "Rubber–fibre composite modelling and its influence on fatigue damage assessment," *Fatigue and Fracture of Engineering Materials and Structures*, vol. 44, no. 2, pp. 521–532, 2021, ISSN: 14602695. DOI: 10.1111/ffe.13377.

[55] R. M. Pidaparti, H. T. Yang, and W. Soedel, "Modeling and Fracture Prediction of Single Ply Cord-Rubber Composites," *Journal of Composite Materials*, vol. 26, no. 2, pp. 152–170, 1992, ISSN: 1530793X. DOI: 10.1177/002199839202600201.

[56] R. M. V. Pidaparti, "Hierarchical bending analysis of cord-rubber composites," *AIAA Journal*, vol. 33, no. 12, pp. 2359–2363, Dec. 1995, ISSN: 0001-1452. DOI: 10.2514/3.12992.

[57] S. Kocak and R. M. V. Pidaparti, "Three-Dimensional Micromechanical Modeling of Cord-Rubber Composites," *Mechanics of Advanced Materials and Structures*, vol. 7, no. 1, pp. 19–34, Jan. 2000, ISSN: 1537-6494. DOI: 10.1080/107594100305401.

[58] R. Pidaparti, S. Jayanti, J. Henkle, and H. El-Mounayri, "Design simulation of twisted cord–rubber structure using ProE/ANSYS," *Composite Structures*, vol. 52, no. 3-4, pp. 287–294, May 2001, ISSN: 02638223. DOI: 10.1016/S0263-8223(01)00021-6.

[59] A. Bhosale, "A Study of Cord-Reinforced Rubber FEA Modelling Techniques (Internship Report)," TANIQ B.V, Rotterdam, Tech. Rep., Nov. 2021.

[60] J. van Campen, "Pattern Search," TANIQ B.V., Rotterdam, Tech. Rep., Nov. 2013.

[61] P. Hipp and D. Jensen, "Design and analysis of filament-wound cylinders in compression," in *33rd Structures, Structural Dynamics and Materials Conference*, Reston, Virigina: American Institute of Aeronautics and Astronautics, Apr. 1992, pp. 2442–2452. DOI: 10.2514/6.1992-2307.

[62] C. Shen, X. Han, and Z. Guo, "A New Method for Calculating the Stiffness of Filament Wound Composites considering the Fibre Undulation and Crossover," *Advanced Composites Letters*, vol. 23, no. 4, p. 096 369 351 402 300, Jul. 2014, ISSN: 2633-366X. DOI: 10.1177/096369351402300402.

[63] J. Rousseau, D. Perreux, and N. Verdière, "The influence of winding patterns on the damage behaviour of filament-wound pipes," *Composites Science and Technology*, vol. 59, no. 9, pp. 1439–1449, Jul. 1999, ISSN: 02663538. DOI: 10.1016/S0266-3538(98)00184-5.

[64] D. M. Yin, B. M. Li, and H. Ch Xiao, "Prediction of three-dimensional elastic behavior of filament-wound composites based on the bridging model," *Journal of Physics: Conference Series*, vol. 1507, no. 6, p. 062 008, Apr. 2020, ISSN: 1742-6588. DOI: 10.1088/1742-6596/1507/6/062008.

[65] S. P. Pai and D. W. Jensen, "Influence of Fiber Undulations on Buckling of Thin Filament-Wound Cylinders in Axial Compression," *Journal of Aerospace Engineering*, vol. 14, no. 1, pp. 12–20, Jan. 2001, ISSN: 0893-1321. DOI: 10.1061/(ASCE)0893-1321(2001)14:1(12).

[66] X. Li, J. Dufty, and G. M. Pearce, "Automation of tow wise modelling for automated fibre placement and filament wound composites," *Composites Part A: Applied Science and Manufacturing*, vol. 147, Aug. 2021, ISSN: 1359835X. DOI: 10.1016/j.compositesa.2021.106449.

[67] Y. Zhang, Z. Xia, and F. Ellyin, "Two-scale analysis of a filament-wound cylindrical structure and application of periodic boundary conditions," *International Journal of Solids and Structures*, vol. 45, no. 20, pp. 5322–5336, 2008, ISSN: 00207683. DOI: 10.1016/j.ijsolstr.2008.05.026.

[68] T. Cormen, C. Leiserson, R. Rivest, and C. Stein, "Finding the Convex Hull," in *Introduction to Algorithms*, 3 ed., Cambridge, Massachusetts: MIT Press, Jul. 2009, ch. 33, pp. 1029–1039.

[69] M. H. Nagaraj, M. Petrolo, and E. Carrera, "A global–local approach for progressive damage analysis of fiber-reinforced composite laminates," *Thin-Walled Structures*, vol. 169, Dec. 2021, ISSN: 02638231. DOI: 10.1016/j.tws.2021.108343.

[70] A. Visrolia and M. Meo, "Multiscale damage modelling of 3D weave composite by asymptotic homogenisation," *Composite Structures*, vol. 95, pp. 105–113, Jan. 2013, ISSN: 02638223. DOI: 10.1016/j.compstruct.2012.07.018.

[71] D. Pulungan, G. Lubineau, A. Yudhanto, R. Yaldiz, and W. Schijve, "Identifying design parameters controlling damage behaviors of continuous fiber-reinforced thermoplastic composites using micromechanics as a virtual testing tool," *International Journal of Solids and Structures*, vol. 117, pp. 177–190, Jun. 2017, ISSN: 00207683. DOI: 10.1016/j.ijsolstr.2017.03.026.

[72] G. Zhou, Q. Sun, D. Li, *et al.*, "Meso-scale modeling and damage analysis of carbon / epoxy woven fabric composite under in-plane tension and compression loadings," *International Journal of Mechanical Sciences*, vol. 190, 2021. DOI: 10.1016/j.ijmecsci.2020.105980..

[73] M. Okereke and S. Keates, *Finite Element Applications* (Springer Tracts in Mechanical Engineering). Cham: Springer International Publishing, 2018, ISBN: 978-3-319-67124-6. DOI: 10.1007/978-3-319-67125-3.

[74] J. Lemaitre, *A Course on Damage Mechanics*. Berlin, Heidelberg: Springer Berlin Heidelberg, 1996, ISBN: 978-3-540-60980-3. DOI: 10.1007/978-3-642-18255-6.

[75] S. Hühne, J. Reinoso, E. Jansen, and R. Rolfes, "A two-way loose coupling procedure for investigating the buckling and damage behaviour of stiffened composite panels," *Composite Structures*, vol. 136, pp. 513–525, Feb. 2016, ISSN: 02638223. DOI: 10.1016/j.compstruct.2015.09.056.

[76] A. Bogdanovich and I. Kizhakkethara, "Three-dimensional finite element analysis of double-lap composite adhesive bonded joint using submodeling approach," *Composites Part B: Engineering*, vol. 30, no. 6, pp. 537–551, Sep. 1999, ISSN: 13598368. DOI: 10.1016/S1359-8368(99)00026-8.

[77] M. Akterskaia, E. Jansen, S. R. Hallett, P. Weaver, and R. Rolfes, "Analysis of skin-stringer debonding in composite panels through a two-way global-local method," *Composite Structures*, vol. 202, pp. 1280–1294, Oct. 2018, ISSN: 02638223. DOI: 10.1016/j.compstruct.2018.06.064.

[78] M. Akterskaia, E. Jansen, S. Hühne, and R. Rolfes, "Efficient progressive failure analysis of multi-stringer stiffened composite panels through a two-way loose coupling global-local approach," *Composite Structures*, vol. 183, no. 1, pp. 137–145, Jan. 2018, ISSN: 02638223. DOI: 10.1016/j.compstruct.2017.02.011.

[79] M. Akterskaia, E. Jansen, S. R. Hallett, P. M. Weaver, and R. Rolfes, "Progressive failure analysis using global-local coupling including intralaminar failure and debonding," in *AIAA Journal*, vol. 57, American Institute of Aeronautics and Astronautics Inc., 2019, pp. 3078–3089. DOI: 10.2514/1.J057677.

[80] F. Daghia, E. Baranger, D.-T. Tran, and P. Pichon, "A hierarchy of models for the design of composite pressure vessels," *Composite Structures*, vol. 235, p. 111 809, Mar. 2020, ISSN: 02638223. DOI: 10.1016/j.compstruct.2019.111809.

[81] S. T. Peters, *Composite filament winding*. ASM International, 2011, ISBN: 9781615037223.

[82] L. R. G. Treloar, "Stress-strain data for vulcanised rubber under various types of deformation," *Transactions of the Faraday Society*, vol. 40, p. 59, 1944, ISSN: 0014-7672. DOI: 10.1039/tf9444000059.

[83] D. F. Jones and L. R. G. Treloar, "The properties of rubber in pure homogeneous strain," *Journal of Physics D: Applied Physics*, vol. 8, no. 11, pp. 1285–1304, Aug. 1975, ISSN: 0022-3727. DOI: 10.1088/0022-3727/8/11/007.

[84] R. W. Ogden, G. Saccomandi, and I. Sgura, "Fitting hyperelastic models to experimental data," *Computational Mechanics*, vol. 34, no. 6, pp. 484–502, 2004, ISSN: 01787675. DOI: 10.1007/s00466-004-0593-y.

[85] E. H. Twizell and R. W. Ogden, "Non-linear optimization of the material constants in Ogden's stress-deformation function for incompressinle isotropic elastic materials," *The Journal of the Australian Mathematical Society. Series B. Applied Mathematics*, vol. 24, no. 4, pp. 424–434, Apr. 1983, ISSN: 0334-2700. DOI: 10.1017/s0334270000003787.

[86] C. Lechat, A. R. Bunsell, P. Davies, *et al.*, "Mechanical behaviour of polyethylene terephthalate & polyethylene naphthalate fibres under cyclic loading Mechanical behaviour of polyethylene terephthalate & polyethylene naphthalate fibres under cyclic loading Mechanical behaviour of Polyethylene Terephthalate & Polyethylene Naphthalate fibres under cyclic loading," *Journal of Materials Science MARCH*, vol. 41, no. 6, pp. 1745–1756, 2006, ISSN: 1745-1756. DOI: 10.1007/s10853-006-2372-x{\"{i}}.

[87] R. Marlow, "A general first-invariant hyperelastic constitutive model," in *Constitutive Models for Rubber*, J. Busfield and A. Muhr, Eds., London: CRC Press, Jan. 2003, pp. 157–160, ISBN: 9789058095664.

[88] V. Madhavan and N. K. Naik, "Elastic behavior of twisted impregnated yarns," *Collection of Technical Papers - AIAA/ASME/ASCE/AHS/ASC Structures, Structural Dynamics and Materials Conference*, vol. 2, pp. 936–944, 1999, ISSN: 02734508. DOI: 10.2514/6.1999-1298.

[89] J. S. McQuien, H. K. Adluru, E. Iarve, and A. Harman, "A global-local discrete damage modeling framework for composite laminates," in *AIAA Scitech 2019 Forum*, Reston, Virginia: American Institute of Aeronautics and Astronautics, Jan. 2019, ISBN: 978-1-62410-578-4. DOI: 10.2514/6.2019-1550.

[90] G. A. Fiordilino, A. Pagani, E. Carrera, and M. Montemurro, "Global-local analysis of composite structures," in *21ème Journées Nationales sur les Composites*, Bordeaux: École Nationale Supérieure d'Arts et Métiers, Jul. 2019.

[91] Dassault Systèmes, "Rebar modeling in shell, membrane, and surface elements," in *ABAQUS Theory Manual*, 2021.

[92] T. Lehmann and J. Ihlemann, "Strain analysis of cord-rubber composites using DIC," *Materials Today: Proceedings*, vol. 32, pp. 183–186, 2020, ISSN: 22147853. DOI: 10.1016/j.matpr.2020.04.537.

[93] Dassault Systèmes, "Solid (continuum) elements," in *ABAQUS Analysis User's Manual*, 2021.

[94] Dassault Systèmes, "Hybrid incompressible solid element formulation," in *ABAQUS Theory Manual*, 2021.

[95] Simulia, "Embedded Elements," in *ABAQUS Analysis User's Manual*, 2021.

[96] R. Breidenbach and G. Lake, "Application of Fracture Mechanics to Rubber Articles , Including Tyres," *Philosophical Transactions of the Royal Society of London. Series A, Mathematical and Physical Sciences*, vol. 299, no. 1446, pp. 189–202, 1981. DOI: 10.1098/rsta.1981.0018.

[97] Y. S. Huang and O. Yeoh, "Crack Initiation and Propagation in Model Cord-Rubber Composites," *Rubber Chemistry and Technology*, vol. 62, no. 4, pp. 709–731, 1989. DOI: 10.5254/1.3536270.

[98] Z. Tian, H. Song, Z. Wan, and X. Du, "Fatigue properties of steel cord-rubber composite," *Journal of Elastomers and Plastics*, vol. 33, no. 4, pp. 283–296, 2001, ISSN: 00952443. DOI: 10.1106/17HE-05X2-8WAU-HV92.

[99] B. L. Lee, B. H. Ku, D. S. Liu, and P. K. Hippo, "Fatigue of cord-rubber composites: II. Strain-based failure criteria," *Rubber Chemistry and Technology*, vol. 71, no. 5, pp. 866–888, 1998, ISSN: 00359475. DOI: 10.5254/1.3538515.

[100] J. Song, "Fatigue of Cord-Rubber Composites for Tires," Ph.D. dissertation, The Pennsylvania State University, 2004.

[101] J. Gao, X. Yang, L. H. Huang, and Y. Suo, "Experimental study on mechanical properties of aramid fibres reinforced natural rubber/SBR composite for large deformation–quasi-static mechanical properties," *Plastics, Rubber and Composites*, vol. 47, no. 9, pp. 381–390, 2018, ISSN: 17432898. DOI: 10.1080/14658011.2018.1514480.

[102] S. Rao, I. M. Daniel, and E. E. Gdoutos, "Mechanical properties and failure behavior of cord/rubber composites," *Applied Composite Materials*, vol. 11, no. 6, pp. 353–375, 2004, ISSN: 0929189X. DOI: 10.1023/B:ACMA.0000045312.61921.1f.

[103] L. Michel, A. Vadean, and R. Benoit, "Tire burst phenomenon and rupture of a typical truck tire bead design," *Tire Science and Technology*, vol. 39, no. 4, pp. 270–283, 2011, ISSN: 00908657. DOI: 10.2346/1.3672044.

[104] B. Davids, "Structural Analysis of Multi-Layered Filament Wound Cord-Reinforced Rubber Products," Ph.D. dissertation, TU Delft, 2014.

[105] Dassault Systèmes, "USDFLD," in *ABAQUS User Subroutine Reference Manual*, 2021.

[106] R. Durairaj, "Resorcinol Formaldehyde Latex (RFL) Adhesives and Applications," in *Resorcinol: Chemistry, Technology and Applications*, Berlin/Heidelberg: Springer-Verlag, 2005, pp. 263–339. DOI: 10.1007/3-540-28090-1{_}6.

[107] National Highway Traffic Safety Administration, "Engineering Analysis Report and Initial Decision Regarding EA00-023: Firestone Wilderness AT Tires," Tech. Rep., 2001.

[108] C. Valantin, F. Lacroix, M.-P. Deffarges, J. Morcel, and N. Aït Hocine, "Interfacial damage on fatigue-loaded textile-rubber composites," *Journal of Applied Polymer Science*, vol. 132, no. 4, n/a–n/a, Jan. 2015, ISSN: 00218995. DOI: 10.1002/app.41346.

[109] N. K. Jha and U. Nackenhorst, "Fatigue mechanisms of cord-rubber composites," *Pamm*, vol. 15, no. 1, pp. 133–134, 2015. DOI: 10.1002/pamm.201510057.

[110] Dassault Systèmes, "Node-based submodeling," in *ABAQUS Analysis User's Manual*, 2021.

[111] ASTM International, "ASTM D412-16: Standard Test Methods for Vulcanized Rubber and Thermoplastic Elastomers — Tension," *ASTM Standards*, pp. 1–14, 2016.

[112] J. Day and K. Miller, "Equibiaxial Stretching of Elastomeric Sheets, An Analytical Verification of Experimental Technique," Axel Products, Tech. Rep.

[113] ASTM International, "ASTM D885-10a: Standard Test Methods for Testing Tire Cords , Tire Cord Fabrics , and Industrial Yarns," pp. 1–10, 2010.

[114] ASTM International, "D4776/D4776M − 18: Standard test method for strap peel adhesion of reinforcing cords or fabrics to rubber compounds," pp. 1–5, 2018.

[115] Dassault Systèmes, "UANISOHYPER_STRAIN," in *ABAQUS User Subroutine Reference Manual*, 2021.

[116] Dassault Systèmes, "Anisotropic hyperelastic behavior," in *ABAQUS Analysis User's Manual*, 2021.

[117] H. K. Lee, D. S. Kim, J. S. Won, D. Y. Jin, H. J. Lee, and S. G. Lee, "Effects of Thermal and Humidity Aging on the Interfacial Adhesion of Polyketone Fiber Reinforced Natural Rubber Composites," *Advances in Materials Science and Engineering*, vol. 2016, 2016, ISSN: 16878442. DOI: 10.1155/2016/4159072.

[118] B. Chen, "Lecture 6: Fracture and Damage," in *Lecture Notes: Non-Linear Modelling*, 2020.

[119] X. F. Hu, B. Y. Chen, M. Tirvaudey, V. B. Tan, and T. E. Tay, "Integrated XFEM-CE analysis of delamination migration in multi-directional composite laminates," *Composites Part A: Applied Science and Manufacturing*, vol. 90, pp. 161–173, Nov. 2016, ISSN: 1359835X. DOI: 10.1016/j.compositesa.2016.07.007.

[120] M. Ridha, C. H. Wang, B. Y. Chen, and T. E. Tay, "Modelling complex progressive failure in notched composite laminates with varying sizes and stacking sequences," *Composites Part A: Applied Science and Manufacturing*, vol. 58, pp. 16–23, Mar. 2014, ISSN: 1359835X. DOI: 10.1016/j.compositesa.2013.11.012.

[121] Z. C. Su, T. E. Tay, M. Ridha, and B. Y. Chen, "Progressive damage modeling of open-hole composite laminates under compression," *Composite Structures*, vol. 122, pp. 507–517, Apr. 2015, ISSN: 02638223. DOI: 10.1016/j.compstruct.2014.12.022.

[122] S. van der Linden, "Design Optimisation of a Thick Filament Wound Reinforced Rubber Hose Coupling Section," Ph.D. dissertation, TU Delft, 2016.

[123] L. Zhao, S. C. Mantell, D. Cohen, and R. McPeak, "Finite element modeling of the filament winding process," *Composite Structures*, vol. 52, no. 3-4, pp. 499–510, May 2001, ISSN: 02638223. DOI: 10.1016/S0263-8223(01)00039-3.

[124] R. Rafiee and M. A. Torabi, "Stochastic prediction of burst pressure in composite pressure vessels," *Composite Structures*, vol. 185, pp. 573–583, Feb. 2018, ISSN: 02638223. DOI: 10.1016/j.compstruct.2017.11.068.

[125] D. C. Drucker, "A Definition of Stable Inelastic Material," *Journal of Applied Mechanics*, vol. 26, no. 1, pp. 101–106, Mar. 1959, ISSN: 0021-8936. DOI: 10.1115/1.4011929.

[126] Dassault Systèmes, "Fitting of hyperelastic and hyperfoam constants," in *ABAQUS Theory Manual*, 2021.

This page was intentionally left blank.

A

Rebar Continuum Formulation

In this section, the continuum theory used to develop the rebar elements for the global model is discussed. This method is not a development resulting from this project and is rather just a condensation of ideas presented by Helnwein et. al [51] and the ABAQUS theory manual [91]. For the application of rebar elements to this project, readers may refer to chapter 6.

Rebar creates an orthotropic continuum for a reinforced matrix material that bases its mechanical response on three parameters:

1. Material properties of the reinforcement and the matrix.
2. Cross-sectional area of the reinforcement.
3. Spacing between adjacent reinforcing elements in the matrix.

Rebar is usually used in conjunction with 2D surface elements in ABAQUS. The isoparametric directions ($\mathbf{A}_\alpha$) for these elements may be given by:

$$\mathbf{A}_\alpha = \frac{\partial \mathbf{X}}{\partial \xi^\alpha} = \frac{\partial N^A}{\partial \xi^\alpha}\mathbf{X}_A \tag{A.1}$$

Where $\mathbf{X}$ is the position on the surface element, ξ^α is the α^{th} isoparametric coordinate function, and N^A are the element's shape functions. If $\mathbf{T}$ is the initial user-defined rebar direction, then the initial rebar angle (θ_0) can be calculated by:

$$\theta_0 = \cos^{-1}\left\{\frac{\langle \mathbf{T}, \mathbf{A}_\alpha \rangle}{\|\mathbf{A}_\alpha\|}\right\}, \quad \text{no sum on } \alpha \tag{A.2}$$

Here, the isoparametric direction (α) with respect to which the rebar angle is defined can be selected by the user. It is now assumed that the rebar deformation is based on the deformation of the underlying surface element. Then, the rebar stretch (λ_r) is given by:

$$\lambda_r = \|\mathbf{F} \cdot \mathbf{T}\| = \|\mathbf{t}\| \tag{A.3}$$

Here, $\mathbf{t} = \mathbf{F} \cdot \mathbf{T}$ is the deformed rebar filament. To obtain the stretch in the spacing between the rebar filaments, the deformation perpendicular to the rebar direction is considered. If $\mathbf{P}$ is considered

as the initial unit vector perpendicular to $\mathbf{T}$, then the corresponding perpendicular unit vector post deformation ($\mathbf{p}$) is given as:

$$\mathbf{p} = \frac{\mathbf{F}^{-T} \cdot \mathbf{P}}{\|\mathbf{F}^{-T} \cdot \mathbf{P}\|} \tag{A.4}$$

Then, the rebar spacing stretch (λ_s) is given by the component of the deformation of $\mathbf{P}$ along the direction of ($\mathbf{p}$) as follows:

$$\lambda_p = \langle \mathbf{p}, \mathbf{F} \cdot \mathbf{P} \rangle = \frac{1}{\|\mathbf{F}^{-T} \cdot \mathbf{P}\|} \left\langle \mathbf{F}^{-T} \cdot \mathbf{P}, \mathbf{F} \cdot \mathbf{P} \right\rangle = \frac{\langle \mathbf{P}, \mathbf{P} \rangle}{\|\mathbf{F}^{-T} \cdot \mathbf{P}\|} \tag{A.5}$$

Given $\mathbf{P}$ is a unit vector, equation (A.5) may be expressed as:

$$\lambda_p = \frac{1}{\|\mathbf{F}^{-T} \cdot \mathbf{P}\|} \tag{A.6}$$

Similar to equation (A.2), the deformed rebar angle may be expressed in terms of the deformed rebar direction and the updated isoparametric direction:

$$\theta = \cos^{-1} \left\{ \frac{\langle \mathbf{t}, \mathbf{a}_\alpha \rangle}{\|\mathbf{t}\| \, \|\mathbf{a}_\alpha\|} \right\}, \quad \text{no sum on } \alpha \tag{A.7}$$

Finally, the rebar cross-sectional area (A_r) and the rebar spacing (S_r) may be updated as follows, where A_r^0 and S_r^0 are the original rebar area and spacing respectively.

$$A_r = \frac{A_r^0}{\lambda_r} \quad \text{and} \quad S_r = S_r^0 \lambda_p \tag{A.8}$$

Thus, using this rebar formulation, it is evident that it is capable of undergoing large deformation under finite-strain effects, and is also able to update key parameters such as fibre angles, fibre spacings and fibre cross-sectional areas accordingly.

B

Marlow Hyperelastic Model

In chapter 5, the Marlow model [87] was used to model the fibre uniaxial tension response as an incompressible hyperelastic material. The novelty of this hyperelastic model is that it is able to capture the experimental data exactly without the need for the strain energy density functional. This section explores the workings of this model.

The Marlow model is expressed solely in terms of the first invariant of the Cauchy stretch tensor $\mathbf{C}$. Using equation (B.1), it is evident that I_1 can be considered to be a measure of the deformation magnitude.

$$I_1(C) = \mathrm{Tr}(C) = \mathrm{Tr}(F^T F) = \mathrm{Tr}\,|F|^2 \tag{B.1}$$

Exapanding on this idea, by enforcing material incompressibility, equation (B.1) may be written only in terms of λ_1 and λ_2 as shown:

$$I_1 = \lambda_1^2 + \lambda_2^2 + \frac{1}{\lambda_1^2 \lambda_2^2} \tag{B.2}$$

Using equation (B.2), it can be proven that for any combination of $\lambda_1, \lambda_2 \in (1, \infty)$, I_1 monotonically increases from $3 \to \infty$. Thus, if the strain energy density is defined solely in terms of I_1, then through the course of infinite deformation, it will pass through all the possible values of Ψ.

For the case of uniaxial tension, as is considered for the fibres in this project, the first invariant can be expressed as:

$$I_1 = \lambda_T^2 + \frac{2}{\lambda_T} \tag{B.3}$$

Then, using equation (B.3), given a specified value of I_1, it is possible to find the corresponding stretch (λ_T) as a unique root to the cubic in equation (B.4) such that $\lambda_T \geq 1$.

$$\lambda_T(\hat{I})^3 - \hat{I}\lambda_T(\hat{I}) + 2 = 0 \tag{B.4}$$

Then, if experimental nominal stress-strain data is known, the strain energy density may be obtained using:

$$\Psi(I_1) = \int_0^{\lambda_T - 1} \sigma(\epsilon) d\epsilon \tag{B.5}$$

The strain energy expression in equation (B.5) is thus recovered using just the first invariant and is able to capture the experimental data exactly. For actual use, test data is simply inserted in equation (B.5) in place of σ. Thus, no curve fitting is required either.

C

Fitting Data to Hyperelastic Models and Model Stability

The fit of test data to the 6^{th} order Ogden model as described in chapter 5 is an important step to not only obtain accurate load-displacement relations for the rubber but also to ensure that the material model is stable in the strain-domain of interest. This section describes the techniques used to get the calibration constants for the Ogden model and also the stability check to ensure that the obtained constants lead to a stable material model.

C.1. Nonlinear Least Squares Fit

A variation of the Marquard-Levenberg nonlinear least squares algorithm proposed by Twizell and Ogden [85] is used to fit the material constants for this study.

As a refresher, the strain energy density functional for the Ogden model is defined as:

$$\Psi = \sum_{p=1}^{N} \frac{2\mu_p}{\alpha_p^2} \left(\bar{\lambda}_1^{\alpha_p} + \bar{\lambda}_2^{\alpha_p} + \bar{\lambda}_3^{\alpha_p} - 3 \right) + \sum_{p=1}^{N} \frac{1}{D_p} \left(J_{e\ell} - 1 \right)^{2p} \tag{C.1}$$

In case of purely incompressible behaviour, the deviatoric terms can be dropped, resulting in:

$$\Psi = \sum_{p=1}^{N} \frac{2\mu_p}{\alpha_p^2} \left(\lambda_1^{\alpha_p} + \lambda_2^{\alpha_p} + \lambda_3^{\alpha_p} - 3 \right) \tag{C.2}$$

A vector of calibration constants - a may be defined as:

$$a = \left(\mu_1, \alpha_1, \ldots, \mu_p, \alpha_p \right)^T \tag{C.3}$$

In equation (C.1), Ψ is linear with respect to μ but nonlinear with respect to α. Arbitrary initial values of α may be chosen, after which the corresponding initial values for μ can be found using a simple least squares fit. Then, the optimal calibration constants are calculated based on a recursive update of the vector a as shown in equation (C.4):

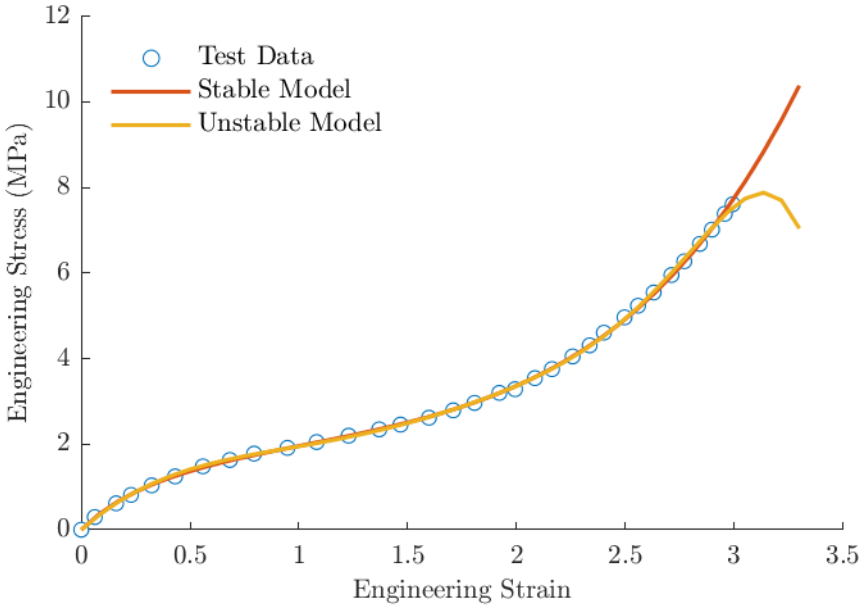

Figure C.1: Comparision of stable and unstable hyperelastic calibrations for rubber test data

$$a_i^{(r+1)} = a_i^{(r)} - \sum_{j=1}^{m}\sum_{k=1}^{n}\left[P_{ik}^{(r)}P_{jk}^{(r)} + \gamma\delta_{ij}\right]^{-1} P_{jk}^{(r)}R_k^{(r)} \tag{C.4}$$

Here, $m = 2N$ is the number of terms contributing to the deviatoric behaviour in the Ogden model. For purely incompressible materials, this may be ignored. r is the iteration count, while n is the number of test data points. R is the vector of relative errors, given by the error between the experimental tractions (t^{test}) and model tractions (t^{th}) as follows:

$$R_k = \frac{t_k^{\text{test}} - t_k^{\text{th}}}{t_k^{\text{test}}} \tag{C.5}$$

Finally, P is the derivative of the error R with respect to the coefficient vector a:

$$P_{ik} = \frac{\partial R_k}{\partial a_i} = -\frac{1}{t_k^{\text{test}}}\frac{\partial t_k^{\text{th}}}{\partial a_i} \tag{C.6}$$

Using equation (C.4), the number of iterations can be adjusted to obtain coefficients converged to the desired degree. Thus, with this method, the experimental data from all the different testing modes are fit to the hyperelastic model simultaneously.

C.2. Drucker Stability Check

The Drucker criteria [125] is a popular check to ascertain if a material behaviour is stable, and is already implemented in ABAQUS to check for the stability of defined materials [126] In this context, stability refers to the material not undergoing arbitrary deformations under infinitesimal loads. it can be postulated that for a material to be stable, the following relation should hold:

$$d\tau : d\varepsilon > 0 \tag{C.7}$$

Via this relation, it is imposed that the internal strain energy of a material should only monotonically increase on the increase in applied load or strain. For an isotropic material, equation (C.7) can be expressed in terms of the principle stresses and strains as:

$$d\tau_1 d\varepsilon_1 + d\tau_2 d\varepsilon_2 + d\tau_3 d\varepsilon_3 > 0 \tag{C.8}$$

For perfectly incompressible materials, the Kirchhoff stress is identical to the Cauchy stress. Additionally, σ_3 can conveniently be chosen as $\sigma_3 = 0$ as a consequence of the hydrostatic stress not affecting the strains due to incompressibility. Then, equation (C.8) can be expressed as:

$$d\sigma_1 d\varepsilon_1 + d\sigma_2 d\varepsilon_2 > 0 \tag{C.9}$$

The Cauchy stress components ($m = 1, 2$) can be found for the Ogden model using equation (5.1) as follows:

$$\sigma_m = \lambda_m \frac{\partial \Psi}{\partial \lambda_m} = \sum_{i=1}^{N} \frac{2\mu_i}{\alpha_i} \left(\lambda_m^{\alpha_i} - \lambda_1^{-\alpha_i} \lambda_2^{-\alpha_i} \right) \tag{C.10}$$

Additionally, the strain components are related to the principle stretches as follows:

$$d\varepsilon_m = \frac{d\lambda_m}{\lambda_m} \tag{C.11}$$

Then, the constitutive relation can be expressed as:

$$\begin{Bmatrix} d\sigma_1 \\ d\sigma_2 \end{Bmatrix} = \begin{bmatrix} K_{11} & K_{12} \\ K_{21} & K_{22} \end{bmatrix} \begin{Bmatrix} d\varepsilon_1 \\ d\varepsilon_2 \end{Bmatrix} \tag{C.12}$$

Here, $\mathbf{K}$ is the tangent stiffness matrix, which for the Ogden model is given by:

$$\mathbf{K} = \sum_{i=1}^{N} 2\mu_i \lambda_1^{-\alpha_i} \lambda_2^{-\alpha_i} \begin{bmatrix} \lambda_1^2 \alpha_{i\lambda} \lambda_2^{\alpha_i} + 1 & 1 \\ 1 & \lambda_1^{\alpha_i} \lambda_2^{2\alpha_i + 1} \end{bmatrix} \tag{C.13}$$

To satisfy the Drucker stability criteria for the Oden model, this expression of $\mathbf{K}$ given by equation (C.13) should be positive definite.